Optimization of single crystalline all diamond scanning probes for quantum sensing applications

Inauguraldissertation

zur
Erlangung der Würde eines Doktors der Philosophie
vorgelegt der
Philosophisch-Naturwissenschaftlichen Fakultät
der Universität Basel

von

MARIETTA BATZER

aus Arlesheim (Basel-Landschaft), Schweiz

Basel, 2019

Genehmigt von der Philosophisch-Naturwissenschaftlichen Fakultät
auf Antrag von
Prof. Dr. Patrick Maletinsky
Prof. Dr. Uwe Pieles

Basel, den 17. Dezember 2019

Prof. Dr. Martin Spiess
Dekan

Invention, my dear friends,
is 93% perspiration,
6% electricity,
4% evaporation,
and 2% butterscotch ripple.

- *Willy Wonky & the Chocolate Factory*

Abstract

Moore's Law demands for innovation not only to solve the question of how to store even more information on even smaller areas but also in how to access this information. Both problems make point defects in solid-state systems very interesting. Color centers in diamond are one of these atom-like systems. Their electronic spins can be used as a versatile sensor or quantum storage. These sensors live up to their full potential when combined with a scanning technique as atomic force microscopy (AFM). The precise control of the position combined with an atom-sized light source or sensor opens up various possibilities. The main struggles encountered by the field so far are the difficulty of retaining the crystal quality of bulk diamond and simultaneously have a sharp tip to get the best topological feedback possible. In our work, we present three different avenues to tackle this. We conduct a study of the cause of decoherence in plasma etched nanostructures and test different treatments to reduce the effect. We test a novel method to stabilize an alternative color center believed to be less sensitive to electric field noise. Furthermore, we explore a new approach combining top-down fabrication and bottom-up overgrowth to get sharp tips with good crystal quality. The combination of the individual avenues has the potential to bring the sensing and imaging capabilities of color center-based sensing to the next level.

Contents

List of symbols and abbreviations

General symbols:

t	time
λ	optical wavelength
τ	spin evolution time
$\tau_{\pi/2}$, τ_{π}	pulse lengths for $\pi/2$- and π-pulses
S	total electron spin
m_s	electron spin quantum number
r	radius

Chemical abbreviations:

Al	Aluminum
Al_2O_3	Alluminium oxide
Ar	Argon
B	Bohr
C	Carbon
^{12}C	Carbon isotope
^{13}C	Carbon isotope
Cl	Chlorine
DI water	deionized water
F	Fluorine
H	Hydrogen
HF	hydrofluoric acid
HSQ	hydrogen silsesquioxane
IPA	iso-2-propanol
Mg	Magnesia
N	Nitrogen
^{14}N	Nitrogen isotope
^{15}N	Nitrogen isotope
O	Oxygen
S	Sulfur
Si	Silicon
TEMED	Tetramethylethylenediamine
TMAH	Tetramethylammonium Hydroxide

Color centers and point defects:

N	single nitrogen defect
N^0	neutrally charged nitrogen center
N^+	positively charged nitrogen center
NV	nitrogen vacancy center
NV^0	neutral NV center
NV^{-1}	negatively charged NV center
NV^+	positively charged NV center
SiV	Silicon-Vacancy center
SiV^0	neutral silicon vacancy center
SiV^{-1}	negatively charged silicon vacancy center
SiV^{-2}	double negatively charged silicon vacancy center
SiV^+	positively charged silicon vacancy center

Abbreviations:

2D	two-dimensional
AC	alternating current
AFM	atomic force microscope
ALD	atomic layer deposition
BFP	back focal plane
CPD	contact potential difference
CVD	chemical vapor deposition
CW	continuous wave
DC	direct current
DP	dipole
ESR	electron spin resonance
FDTD	finite-difference time-domain
FWHM	full width half maximum
HG	hole gas
ICP	inductively coupled plasma etching
KPFM	Kelvin probe force microscopy
LT	low temperature
MW	microwave
NA	numerical aperture
ODMR	optically detected magnetic resonance
PSB	phonon sideband
PSD	position sensitive detector
Φ	Work function
RF	radio-frequency
RT	room temperature
SCD	single crystalline diamond

SEM	scanning electron microscope
T2	coherence time
ZPL	zero-phonon line
XPS	x-ray photo spectroscopy

Units:

A	Ampere
eV	electron Volt
g	gram
h	hour
Hz	Hertz
K	Kelvin
m	meter
nm	nanometer
s	seconds
T	Tesla
W	Watt
V	Volt
μm	micrometer

1. Introduction

Is Moore's law dead? As with Schrödinger's cat as long as we don't try, we won't know. In 1965 the co-founder of Intel Gordon Moore made a prediction. He postulated that the number of transistors one can fit in a given unit of space would double every two years [1]. At the time, it was only an observation of a trend, but as time continued, it became a self-fulfilling prophecy, transistors became smaller and more numerous. Now over 50 years later, we approach the end of an era. An era dominated by silicon-based computer chips, an era with impressive developments. To give an example, a smartphone today, something nearly every person carries around, has more computation power than the computer on the spacecraft delivering the first human to the moon in 1969. Today the average transistor on the market has a size of 14 nm. The newest generation of commercially available chips fabricated and released by Intel this summer has even a 10 nm architecture, and the release of a 7 nm general-purpose GPU is expected for 2021 [2]. But what comes next? How small can we go? We approach fundamental limits like the speed of light and the atomic nature of matter. For perspective, the diameter of an atom ranges from 0.1 to 0.5 nm, meaning 10 nm is only between 20 and 100 atoms in a row. Furthermore, the speed of light provides a natural limitation on how fast a computation can be processed via a single transistor, as the information cannot be transferred faster than at the speed of light. Additional to the fundamental physical limits comes the increasing cost of fabricating smaller and smaller transistors. We come to the point where it is not lucrative anymore to go smaller. However, does the end of Silicon-based electronics simultaneously herald the end of Moore's law?

What is certain is that new technology with new concepts beyond classical silicon-based electronics is needed. Fortunately, there are various ideas and different approaches. Among those, the idea of a quantum computer is one of the most advertised ones. Here concepts of quantum mechanics, such as entanglement and superposition, are used to overcome the problems of a classical computer. Other approaches rely on spintronics [3], electronics based on spins instead of charge, optical computing [4] or biological computing [5].

For several of these fields, point defects in solid-state materials are very attractive candidates. As they combine atom-like systems with excellent coherence properties with the advantage of scalability of a solid-state system. Among the many materials studied, diamond has several attributes rendering it an excellent host, to name a few, exceptional hardness, optical transparency, chemical inertness, and a spin-free lattice. Color centers in diamond can be used either as qubits (quantum bits) or as versatile sensors. Their spin states and optical transitions can be harnessed for applications ranging from quantum communication [6] to quantum networks [7] and quantum sensing [8, 9].

The best-studied defect in diamond is the nitrogen vacancy center. It has proven to be an excellent sensor and has attracted particular interest, triggered by recent

success in, e.g. nanoscale imaging of superconductors [10] and ultra-thin magnets [11, 12], as well as high-frequency probing of spin waves [13].

It all started with a publication in 2005 by Chernobrod and Berman [14] suggesting the creation of a scanning magnetic microscope based on the combination of a photoluminescent nanoprobe exhibiting optically detected magnetic resonance with a scanning microscopy technique, like atomic force microscopy. They predicted nanoscale lateral resolution and single spin sensitivity. The scanning geometry enables a controlled positioning of the sensor in close proximity of the sample. Further, the topography and magnetic field measurements can be recorded simultaneously, simplifying the interpretation of the measured fields. First attempts to implement such a spin microscope with nitrogen vacancies were made by gluing nanodiamonds onto AFM tips [8, 11, 15, 16]. Nanodiamonds have the disadvantage of being a not very defined system with limited control over the point defects orientation and environment, resulting in less than ideal optical and coherence properties.

A more recent approach relies on "top-down" fabrication of monolithic AFM tips from high-purity, single-crystalline diamond (SCD) [17, 18]. Next to the known crystallographic orientation and crystal purity, these tips have the additional advantage of a waveguiding effect of the fluorescence. Hence, minimal power is needed to excite the color center, the fluorescence count rate is increased, and as a result of both, a higher signal to noise ratio is attainable.

To maximize the resolution and sensitivity, one wants to put the sensor as close to the sample as possible. For this, color centers are incorporated very shallowly only a few nm under the diamond surface. Unfortunately, such shallowly, spins are plagued by spin noise present on the sample surface resulting in degradation of coherence and optical properties [19]. A deeper understanding of the interactions between diamond surface and color centers is thus the first step towards creating better sensors and reaching the next level of sensitivity. In this thesis, we explore different routes towards optimizing such sensor tips. The first approach focuses on understanding and optimizing the surface chemistry for nitrogen vacancy-based sensors. The second proposal revolves around the stabilization of a promising alternative color center through targeted surface chemistry modification. And the third avenue relies on the optimization of the scanning probe geometry.

1.1. Scope of this thesis

This thesis is focused on studying and optimizing diamond scanning probes for sensing of nanoscale magnetic fields with a lateral resolution on the order of tens of nanometers. Specifically, we address the surface of such single-crystalline all diamond scanning probes with the motivation to employ them as sensors for magnetic sensing with nanometer resolution.

In Chapter 2, we give an overview of the material properties of diamond in general and as a host for quantum systems in particular. We introduce the concept of color centers with a detailed description of the most popular two point defects, namely the nitrogen vacancy and silicon vacancy. We continue by explaining how a color center-based measurement looks like, using the negatively charged nitrogen vacancy as an example. Next, we present a few sensing applications and describe their

implementations. To conclude this chapter, we discuss why it is mandatory to minimize the sensor to sample distance and the influence of the diamond surface on the color center's spin and optical properties.

In Chapter 3, we focus on the oxygen terminated diamond surface using the negatively charged nitrogen vacancy as reference. Oxygen termination is the most widespread surface termination used but is still not very well controlled. In the first part, we discuss different studies of oxidation protocols under the aspects of charge state stability and influence on coherence time. In the second part, we discuss the different aspects of the problem of reduced optical and coherence properties of the nitrogen vacancy center and present our findings. In the first measurement presented, we focus directly on the impact of diamond nanofabrication on the coherence of nitrogen vacancies and how to counteract it. In the second set of measurements, we evaluate x-ray photo spectroscopy as a tool to characterize diamond surface quality and chemical composition of the diamond surface-termination. We conclude the chapter by summarizing our insights and by discussing them concerning previously reported work and suggesting further experiments.

In Chapter 4, we discuss the impact of hydrogen termination on the diamond surface and the electronic configuration of different color centers. First, we introduce the transfer doping model explaining the band bending and surface conductivity observed for hydrogen-terminated diamond. Then we present our protocol of hydrogen termination based on thermal annealing in a hydrogen atmosphere, including x-ray photo spectroscopy measurements to confirm the successful modification. We continue by studying the impact of the termination on the charge states of the nitrogen and silicon vacancies at room and low temperature. Next, we discuss the role of surface adsorbed water and introduce aluminum oxide as a possible capping layer to protect the diamond surface chemistry. Besides discussing hydrogen as termination, we present the idea of a new surface termination technique enabling the direct writing of a termination onto the diamond.

In Chapter 5, we focus on the optimization of the diamond probe itself by studying a novel fabrication approach combining top-down pillar fabrication with bottom-up overgrowth. We find the resulting pyramids to have a very smooth surface and tip radii on the order of 10 nm. The phononic properties of the pyramids are studied by incorporating color centers into the pyramids. We find excellent collection efficiencies from color centers close to the pyramid apex. To conclude the chapter, we discuss the potential of these nanopyramids as future sensing tips.

In the last chapter, we conclude the thesis by summarizing our findings and the insights gained. We discuss how the different optimizations could be combined and what additional experiments will be needed to improve our understanding of the diamond surface further.

2. Color centers in diamond

As hinted at in the last chapter, this thesis is focused on color centers in diamond with the motivation to create better sensors for applications in sensing magnetic and electric fields. In this chapter, we give the reader background information about diamond itself and its potential as a host material. It is not a coincidence that many interesting and promising color centers are point defects in diamond (there are over 500 known centers [20]). Next, we introduce the color centers relevant to this thesis and present a few sensing applications. Then we introduce the reader to the main focus of this thesis: the diamond surface and its influence on color center-based sensing.

2.1. Diamond as host

"Diamonds are forever" is not just a well-known song by Shirley Bassey but also an appropriate description of the chemical inertness and mechanical robustness of this material [21]. To understand where these properties come from, one needs to have a closer look at the diamonds lattice structure, which is depicted in Fig. 2.1. Diamond is a carbon-based material. Each atom has four valence electrons with the configuration 2s2p. To be able to bond with four neighbors, the one 2s- and three 2p-orbitals are hybridized into four sp^3 orbitals. The angle between the sp^3 orbitals defines the diamond lattice geometry, which forms a face centered cubic (fcc) lattice with an interatomic distance of $1.54\,\mathring{A}$ and a lattice constant of $3.57\,\mathring{A}$.

The fcc geometry, together with the strong C-C covalent bonds, are the reason for the chemical inertness and mechanical hardness of diamond [22, 23]. The rigidity of the C-C bonds and the connectedness of the atoms results in an excellent temperature conductivity ($22\,\mathrm{Wcm^{-1}K^{-1}}$), with a Debye temperature of 1860 K, the highest of all known solids [23, 24].

The electronic properties of diamond are dominated by the large indirect bandgap of 5.5 eV. As a result, undoped diamond forms an insulator with a very high breakdown field of 10 MV/cm at room temperature [24, 25]. Another consequence of the wide band gap is the optical transparency window of diamond, which ranges from deep UV to the far IR. This large band gap is one of the main reasons for the numerous color centers observable in diamond, as a broad range of energy levels and energy spacings can "fit" within the band gap. A further reason why diamond is an ideal host, especially for sensing applications, is that the most abundant isotope of carbon ^{12}C (98.9 %) is nuclear spin free and therefore does not deteriorate the coherence properties of the sensor spin [26]. Furthermore, it is possible to grow diamond in a controlled way such that even isotropically pure diamond ($^{12}\mathrm{C} > 99.7\,\%$) is feasible [27].

In summary, diamond provides an environment protecting the sensor inside from all types of mechanical and chemical influences while being an excellent heat con-

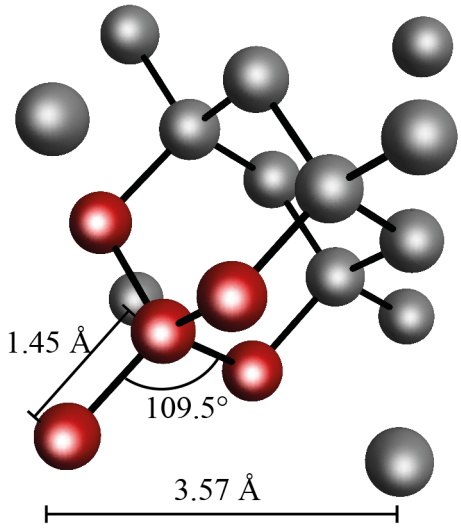

Figure 2.1.: Illustration of a diamond lattice unit cell. One carbon atom and its four neighbors are colored in red to emphasize the tetrahedral structure of the diamond lattice.

ductor and insulator without adding any background noise in terms of electric or magnetic fields. As Nobel Laureate Wolfgang Pauli once said, "God made the bulk; the surface was invented by the devil" [28].

2.2. Color centers for sensing

Color centers in diamond are optically active point defects. They not only determine the color and, therefore, the price of the diamond, but also form atom-like systems with a vast number of possible uses in the fields of quantum science and technology. Their spin properties and optical transitions can be harnessed for applications ranging from quantum communication [6] to quantum networks [7] and quantum sensing [8, 9]. Of the various color centers occurring in diamond, we will present two that have proven relevant and have already found applications in several fields of quantum science and technology.

2.2.1. The nitrogen vacancy center

One of the best-studied color centers is the negatively charged nitrogen vacancy (NV) in diamond. It is a two-atom defect, in which a nitrogen atom replaces one carbon atom of the diamond lattice and a neighboring carbon atom is missing (Fig. 2.2(a)). The defect has trigonal C_{3V} symmetry with the major symmetry axis passing through both the nitrogen atom and the vacancy and positioned along a $\langle 111 \rangle$ axis of the diamond crystal [30]. Consequently there are four different NV orientations, corresponding to the crystallographic directions [111], $[\overline{1}\overline{1}1]$, $[1\overline{1}\overline{1}]$ and $[\overline{1}1\overline{1}]$.

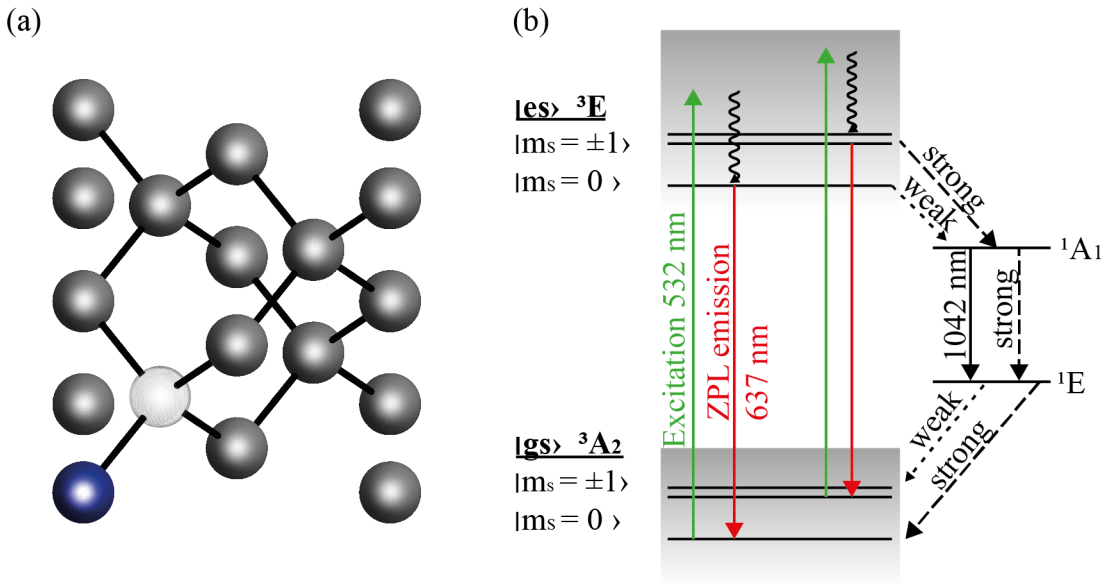

Figure 2.2.: (a) Model of the nitrogen vacancy defect in the diamond lattice. Carbon atoms are represented as gray spheres and the nitrogen as a blue sphere. The vacancy is represented as a white sphere for better visibility of the defect geometry. (b) Schematic of the NV^- electric structure, including the ground ($^3A_2$) and exited (^3E) state triplets as well as the singlets ($^1A_1$, ^1E) forming the metastable state. Solid arrows indicate the optical and infrared radiative transitions. The non-radiative intersystem crossings are drawn with dashed lines. Corrugated arrows represent phonon induced decays. The schematic is adapted from [29]

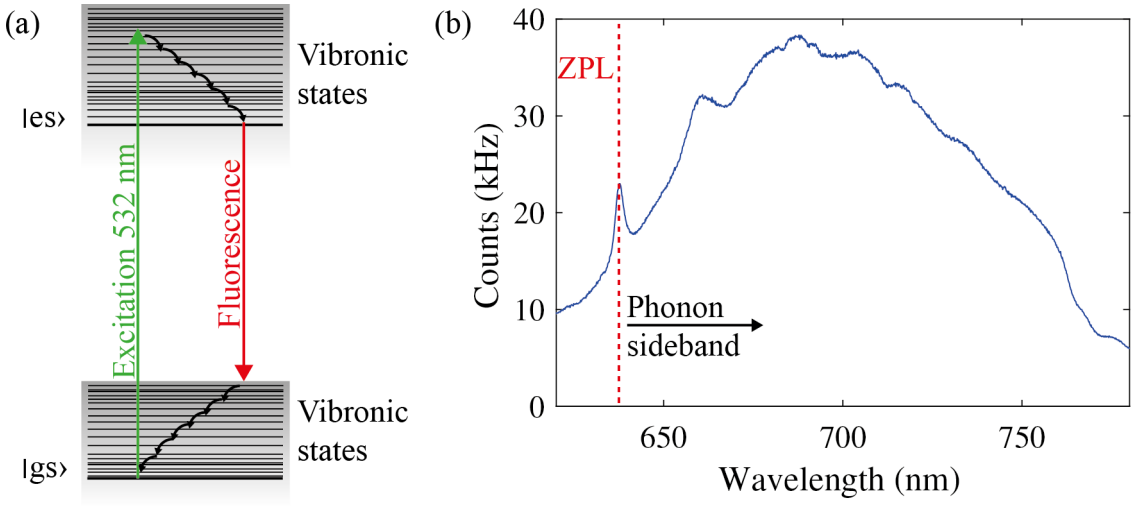

Figure 2.3.: (a) Schematic of off-resonant NV excitation with green laser light. The electron is excited into vibronic states and decays non-radiatively into the pure, electronic excited state by emitting phonons. From there, the system can either decay directly to the ground state and emit a photon into the zero phonon line (ZPL) or decay to the excited vibronic states of the ground state by emitting a photon into the phonon sideband. (b) Representative NV spectrum measured at room temperature with the ZPL at 637 nm, and phonon sideband of the ZPL extending to $\sim$ 750 nm. This figure is adapted from [32].

2.2.1.1. Electronic and optical properties

The neutral NV has five unpaired electrons, two from the nitrogen atom and one from each of the dangling bonds of the carbon atoms that neighbor the vacancy. The remaining three valence electrons of the nitrogen atom are used to form covalent bonds with its neighboring carbon atoms. Depending on the position of the Fermi level in diamond, other charge states can be observed [31]. Due to its magneto-optic response, the negative charge state is the most relevant NV charge state for sensing applications. For simplicity's sake, whenever the abbreviation NV is used in this work, the negative charge state is meant unless a different charge state is explicitly stated. The sixth electron of the NV is typically donated by a nearby N atom, also known as P1 center. Two out of the six electrons of the center are unpaired, resulting in a total electron spin of S=1.

The electronic energy levels of the NV can be described with three major states, consisting of a ground state, an excited state, and a metastable state (Fig. 2.2(b)). The metastable state is formed by two spin-singlet states, the ground and excited states by spin-triplet states. For a detailed description of the underlying physics we refer the reader to [29, 30]. The $m_s = \pm 1$ states have a higher likelihood to decay non-radiatively via the metastable state, resulting in approximately 30 % lower fluorescence when the NV is excited from the $m_s = \pm 1$ ground states. This enables the determination of the spin state based on the fluorescence count rate detected. Another consequence of this spin selective decay is that roughly 80 % of the spin population ends up in the $m_s = 0$ after a few excitation cycles with green laser light ($\sim 1\,\mu s$).

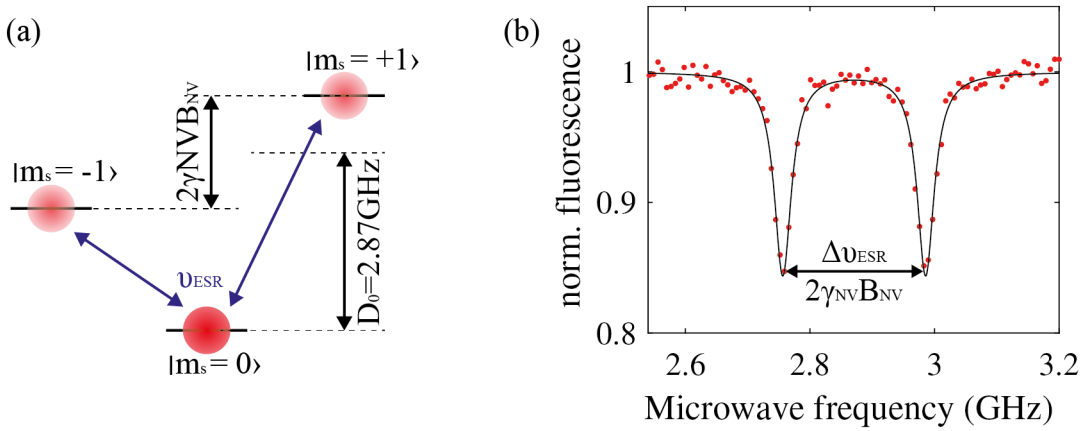

Figure 2.4.: (a) NV ground state spin triplet in the presence of a magnetic filed along the NV symmetry axis. The $ms = \pm 1$ states are separated from the $m_s = 0$ state by the zero field splitting (D_0). The degeneracy ot the $ms = \pm 1$ states is lifted in the presence of a magnetic field by the Zeeman splitting ($2\gamma_{NV}B_{NV}$). The transition between $m_s = 0$ and $m_s = +1$ or $m_s = -1$ can be driven by applying microwave magnetic fields of the frequency ν_{esr}, indicated by solid blue arrows. The relative fluorescence intensity of the different states is indicated by the brightness of the red spheres. (b) Typical electron spin resonance trace (red dots) fitted with the sum of two Lorentzian dips. This figure was reproduced from reference [34].

When the NV is excited off-resonantly with green laser light, it is pumped into a vibronic state from which it decays into the electronic excited state by emitting phonons into the diamond lattice. When the NV decays from the ground state, only ∼4 % of the fluorescence light is emitted in the Zero Phonon Line (ZPL), with the rest of the fluorescence ending up in the phonon sideband (Fig. 2.3(a)). A representative spectrum can be seen in Fig. 2.3(b) with the ZPL at 637 nm and the phonon sideband extending to ∼750 nm. Although the weak emission into the ZPL is one of the main obstacles to overcome for applications relying on coherently interconnecting several NV centers for large scale quantum networks [33], it is not a major issue for sensing.

2.2.1.2. Optically detected magnetic resonance

In typical magnetic resonance spectroscopy, the absorption spectrum of an oscillating magnetic field with a frequency in the microwave regime is measured. In the case of the NV, optical initialization combined with spin-dependent fluorescence allow for direct optical detection of the microwave absorption. The zero-field splitting of the NV lies in the GHz range, and the transition can be driven with a microwave magnetic field. A green laser is used to initialize the NV spin state, and at the same time, a microwave field is applied, and the fluorescence is recorded. The frequency of the magnetic field is swept over the range of interest; when the frequency matches the transition frequency, some of the $m_s = 0$ population will be transferred to the $m_s = \pm 1$ state, which results in a dip in the measured fluorescence. When a magnetic field aligned to the NV axis is applied the degeneracy of the $m_s = \pm 1$ states is lifted due to the Zeeman effect Fig. 2.4(a). Therefore two dips appear in

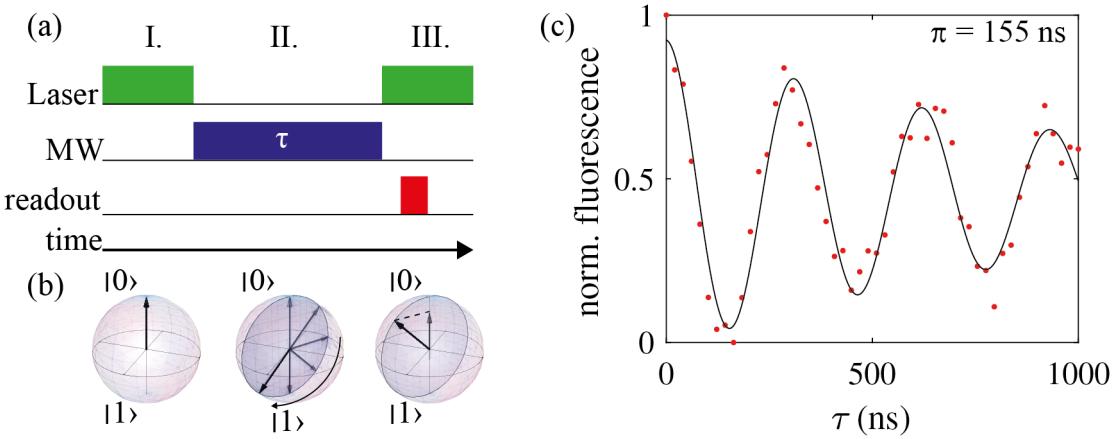

Figure 2.5.: (a) Representation of the pulse sequence used to measure Rabi oscillations. Between the spin initializations (I.) and read out (III.) a MW pulse of length τ is applied (step (II.)). (b) Bloch sphere representation of the NV spin states during the different phases of the measurement. (c) Example Rabi curve (red dots) fitted with an exponentially decaying sinusoid function. The extracted π-pulse length is 155 ns.

the spectrum. The magnetic field projected onto the NV axis can be calculated from the splitting between the $m_s = \pm 1$ states through:

$$\Delta\nu_{\mathrm{esr}} = 2\gamma_{\mathrm{NV}} B_{\mathrm{NV}} \tag{2.1}$$

Where $\Delta\nu_{\mathrm{esr}}$ is the frequency-difference between the two transitions, γ_{NV}=28 MHz/mT is the gyromagnetic of the NV and B_{NV} is the magnetic field projected onto the NV axis [15].

This measurement technique is suitable to measure 'd.c.' magnetic fields with a sensitivity proportional to the linewidth of the ESR transition. The linewidth is influenced by the MW and optical pumping power but ultimately limited by the dephasing rate ($1/T_2^*$) of the NV spin [35]. The 'a.c.' field sensitivity, in contrast, is proportional to the decoherence rate ($1/T_2$). A detailed discussion on the topic of 'a.c.' and 'd.c.' field sensitivity can be found in [8, 36]. Both T_2^* and T_2 can be measured directly employing measurement schemes relying on coherent spin manipulation. The T_2 time is typically used to compare different systems.

2.2.1.3. Spin manipulation and coherence time

To determine the coupling strength between the driving MW field and the NV center, we conduct Rabi oscillation measurements. Rabi oscillations are based on the coherent interaction of a two-level system with an oscillatory driving field [37]. A typical pulse sequence for a Rabi experiment is shown in Fig. 2.5(a). To conduct a Rabi measurement the NV spin is first initialized in m_s=0 with a green laser pulse (Fig. 2.5(a)I). Then a microwave (MW) pulse of length τ is applied (Fig. 2.5(a)II). Finally, the NV state is measured with a second laser pulse (Fig. 2.5(a)III). When a static magnetic field is applied, the $m_s = +1$ and $m_s = -1$ states are no longer degenerate and their transitions can be driven separately. The transition is selected by tuning the frequency of the applied microwave field to match the transi-

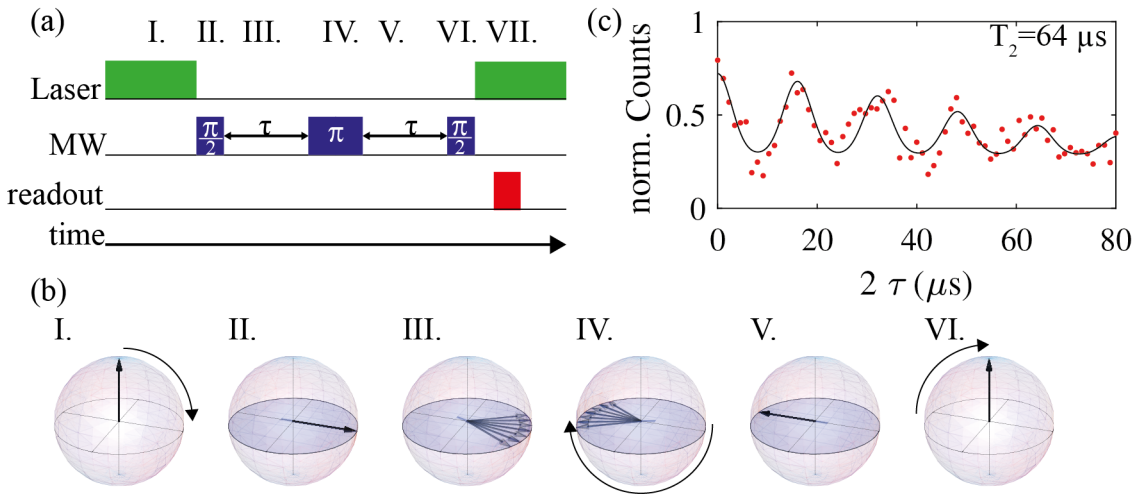

Figure 2.6.: (a) Pulse sequence of a Hahn echo measurement with (b) Bloch sphere representation of the NV spin during the steps (I.-VI.). After the spin initializations (I.), an MW $\pi/2$ pulse (II.) creates a superposition state, a second MW $\pi/2$ pulse VI. maps the superposition state back onto the initial state. In between the MW $\pi/2$ pulses, the system is left in a superposition state for a time τ (III. and V.) to pick up a phase induced by external fields. The π pulse (IV.) in the middle leads to the refocusing of the spin (see main text). (c) Representative spin coherence time measurement on a shallow, 20±5 nm deep NV using a Hahn echo sequence (red dots) with fitted with Eq. (2.2) (black line). The T_2 time found is 64 μs.

tion frequency. In Fig. 2.5(b) the spin states are visualized using the Bloch sphere notation [38], where the north and south pole represent the pure states (typically $|m_s = 0\rangle$ and $|m_s = \pm 1\rangle$) and the surface of the sphere superpositions of the two pure states. Initializing the spin in $m_s = 0$ and corresponds to north on the Bloch sphere (Fig. 2.5(b)I). Applying the MW field coherently transfers the population from one state to the other. Doing so for a prolonged time results in an oscillation between the state populations. Assuming a resonant driving field, the Blochvector representing the spin state oscillates from the north to the south pole in the gray-colored plane. The oscillation axis depends on the phase of the MW field. For a detailed discussion of the phase we refer to reference [32]. The different arrows in Fig. 2.5(b)(II.) represent positions after the application of MW pulses with different durations. In the Bloch sphere notation reading the spin out corresponds to a projection onto the z-axis (Fig. 2.5(b)(III.)).

A typical measurement trace of Rabi oscillations can be found in Fig. 2.5(c). The resulting oscillation can be fitted with an exponentially decaying sinusoid, and the π-pulse length can be extracted. The π-pulse is defined as the time needed by the applied MW field to transfer the spin population from one pure state to the other. It is therefore a measure for the driving strength. In this specific dataset, a decrease in contrast is visible, caused by a loss in spin coherence.

To investigate the decoherence of the NV spin, we employ a Hahn echo-based measurement method [39]. The extracted time is the spin relaxation time T_2, also called spin coherence time. The measurement can also be used to detect whether the NV is coupled to nearby spins, as the echo part of the pulsing sequence causes a

selective sensitivity to specific frequencies and suppresses part of the electromagnetic background noise [19]. A corresponding pulsing diagram can be found in Fig. 2.6(a). As in the Rabi measurement, the pulsing sequence starts by initializing the NV spin in $m_s = 0$ with a laser pulse (Fig. 2.5(a)I). A $\pi/2$ microwave (MW) pulse is then applied to create a superposition of the $m_s = 0$ and $m_s = 1$ states. The system is left in this state for a precession time τ to accumulate phase from the surrounding spin bath. A π pule is then used to invert the accumulated phase such that the second free precession period leads to a refocusing of the spin. The last $\pi/2$-pulse is then used to project the spin again onto the $m_s = 0$ state before the final spin readout. A typical dataset of such a spin echo can be found in Fig. 2.6(c). The periodic peaks, called revivals, stem from the interaction with ^{13}C nuclear spins, a natural isotope occurring within the diamond lattice. The precession of these nuclear spins causes an oscillating magnetic field acting on the NV spin.

To extract the coherence time, the data is fitted with the following equation [40].

$$C(t) = A * \exp\left[-\left(\frac{t}{T_2}\right)^n\right] \sum_{i=0}^{N_R} \exp\left[-\left(\frac{t - i\tau_r}{2\tau_C}\right)^2\right] + C \tag{2.2}$$

The first exponential term defines the envelope function and the main decay with T_2 and n. The value of n depends on the spin bath characteristics and is assumed to be between one and three [40]. The sum of exponents represents the interaction with the ^{13}C spins. A and C are fitting constants, N_R is the number of revivals, τ_R the revival periodicity and τ_C a measure for the width of the peaks.

We have described two types of experiments that we can use to manipulate and study the NV. The measurement of Rabi oscillations allows us to manipulate the quantum state of the NV precisely. On the other hand, the Hahn echo measurement tells us about the local spin bath and allows us to protect the NV against environmental noise. Later in this thesis, we will use both techniques to characterize our NV centers.

2.2.2. The silicon vacancy center

A more recent star in the field of color centers is the negatively charged silicon vacancy center (SiV^-), in which two carbon atoms are missing from the diamond lattice, and a silicon atom is situated on an interstitial position between a split vacancy [42]. The neutral charge state of the SiV center has ten electrons: each of the six surrounding carbon atoms provides one electron, with the remaining four electrons stemming from the silicon valence electrons. As with the NV, a nearby donor provides the additional electron to charge the defect. Like the NV center, the SiV is oriented along the $\langle 111 \rangle$ axis of the diamond, but in contrast to the NV, the SiV is highly symmetric [43]. It belongs to the symmetry group D_{3d}, which includes an inversion center located at the position of the Si atom. As the additional electron is localized at the Si atom, the SiV has no static electric dipole moment [42] and is, as a consequence, not susceptible to Stark-shifts caused by electric fields in the diamond lattice. The electronic structure of the SiV center is depicted in Fig. 2.7(b). For further details regarding the SiV center, we refer the reader to Ref. [42, 43].

Another benefit of the symmetric architecture and the main advantage for quantum application compared to the NV is that 70 % of the SiV fluorescence is emitted

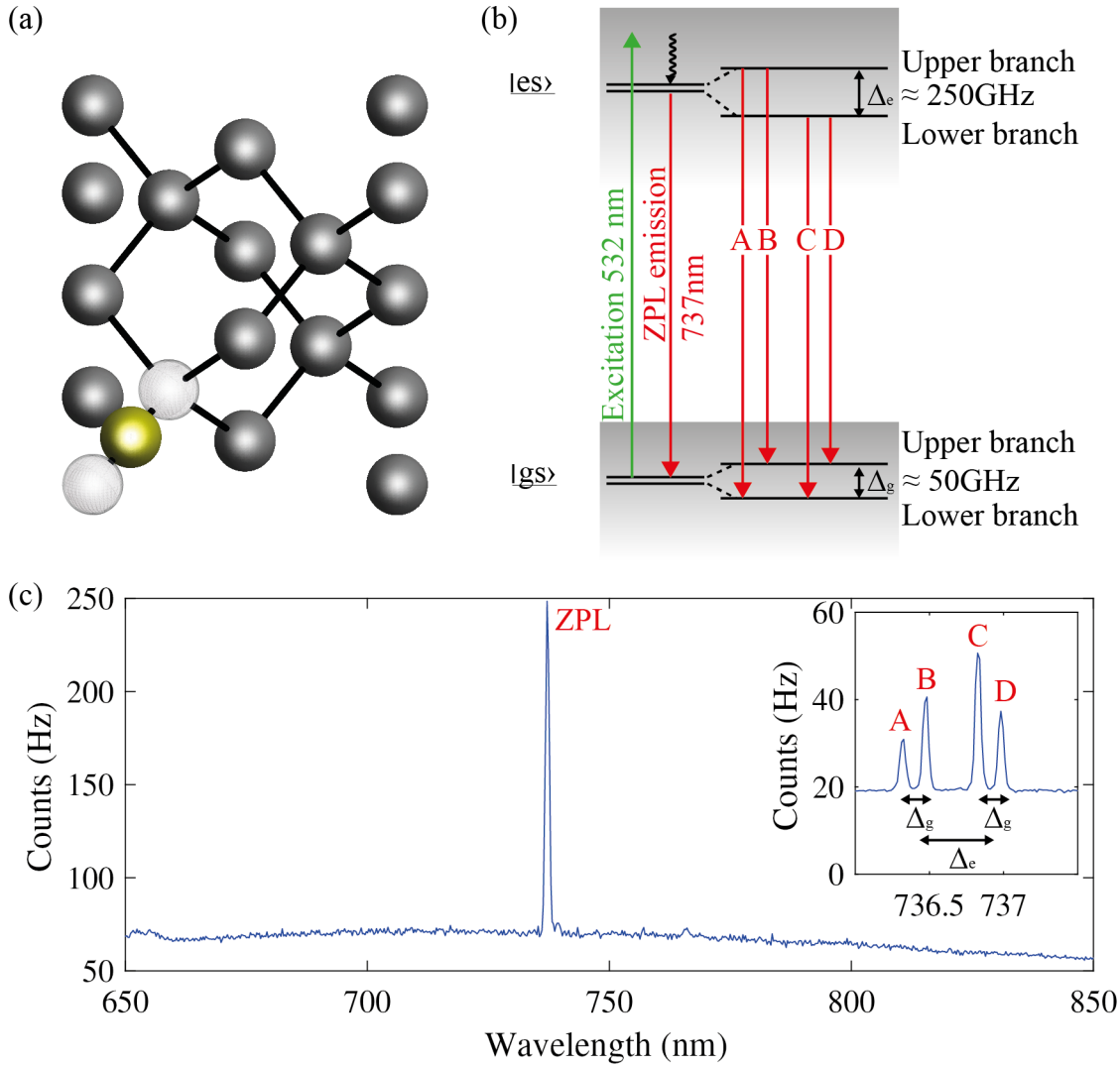

Figure 2.7.: (a) Diamond lattice with a Silicon vacancy center. The Silicon atom (yellow) sits in between two vacant carbon sites. The vacancies (carbon atoms) are represented by white (black) spheres for better visibility. (b) Electronic structure of the negatively charged SiV center, including ground and excited state. The optical radiative transitions are symbolized by solid arrows and phonon induced relaxation by corrugated arrows. The schematic is reconstructed after Ref. [41]. (c) Typical SiV^- spectrum measured at 6 K. Inset: zoom in on ZPL with labeled splitting and transitions.

into the ZPL at 738 nm. Very narrow linewidths have been reported in the case of low-strain bulk diamond at 4 K even lifetime limited linewidths [43, 44]. A typical spectrum can be seen in Fig. 2.7(c). In the inset, the ZPL is resolved to reveal the four transitions between the two gound and excited state sub levels depicted in Fig. 2.7(b). Each of the in total four sub-levels is doubly spin degenerate and split when an external magnetic field is applied. Due to different g-factors in the ground and excited states, each transition spits up into four. The positions of the transitions could then, in principle, also be used to measure magnetic fields [41].

As for the NV, the SiV spin can be coherently manipulated [45]. One of the main drawbacks of the negatively charged SiV is that, due to electron-phonon coupling, the coherence time at room temperature is only ~ 30 ns, much lower than for the NV center (T_2 up to 1 ms) [27]. Cooling the system to 2 K the authors of [46] measured a prolonged coherence time of 3 μs, and were able to initialize and readout the state of a nuclear spin. Never the less the necessity to work at cryogenic temperatures and the short coherence time limit the utility of the SiV^- center for the sensing of small magnetic fields severely. Another approach is to use nanodiamonds to impose boundary conditions to reduce the number of phonons of a critical frequency and thereby extend the coherence time [47]. A very recent idea is to get rid of the electron and use the neutral SiV, which has a total spin of S=1 and is expected to have a similar electronic structure as the NV^- and therefore a long coherence time all while retaining the optical properties of the SiV^-. As it has proven to be challenging to stabilize the neutral charge state, the SiV^0 is not yet well studied. A recent publication reports the successful stabilization of the neutral charge state in a Boron-doped diamond and shows promising first coherence measurements [48].

2.2.3. Sensing applications

Nanoscale quantum sensors using single color center-based electron spins in diamond have attracted particular interest, triggered by recent success in, e.g. nanoscale imaging of superconductors [10] and ultrathin magnets [11, 12], as well as high-frequency probing of spin waves [13]. Such nanoscale quantum sensors live up to their full potential when employed in a scanning probe configuration using atomic force microscopy (AFM) tips that incorporate single spins [8]. This approach allows for precise, sub-nanometre positioning of the quantum sensor and thereby yields optimized resolution and sensitivity. While early implementations of this concept focused on grafting color center-containing nanodiamonds onto AFM tips [8, 11, 16], recent work increasingly focuses on "top-down" fabrication of monolithic AFM tips from high-purity, single crystalline diamond (SCD) [17, 18]. A representative SEM image of an all diamond cantilever with a tapered pillar can be seen in Fig. 2.8. This approach combines several advantages: It yields highly robust tips, amenable to operation in harsh environments, such as cryogenic conditions [10]. It mitigates optical blinking and excess spin dephasing, both of which are ubiquitous in nanocrystals [49]. And lastly, it allows for tailoring the photonic properties of the tips to yield high fluorescence collection efficiencies and thereby high sensitivity [50]. Unfortunately, this is not the end of the story. To optimize the spatial resolution and sensitivity per source strength, it is desirable to minimize the sensor-to-sample distance. As a result, NVs are embedded into the diamond lattice a few nanometers from the

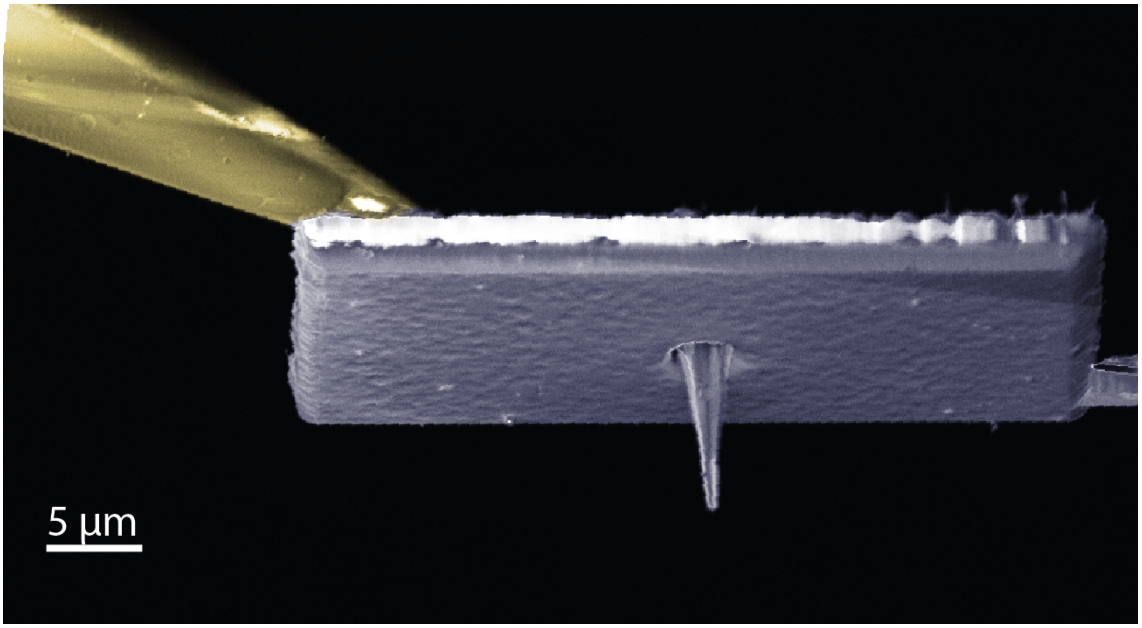

Figure 2.8.: False-colored scanning electron microscopy (SEM) image of an all diamond cantilever (blue) glued to a quartz capillary (gold). The cantilever consists of a platelet with a tapered pillar, with a circular end facet of 200 nm in diameter. The color center is incorporated approximately 20 nm below the surface of the pillar end facet.

diamond surface. However, such shallow NVs are plagued by spin noise present on the surface resulting in degradation of coherence and optical properties [19]. The current state of the art being scanning probes with 9 nm deep NV in 200 nm pillars with average coherence times of 44 μs at room temperature [18].

2.3. Summary and Outlook

In this chapter, we presented a short overview of the material properties of diamond, namely its exceptional hardness, optical transparency, and spin-free lattice. We introduced the concept of color centers with the detailed presentation of two of the most popular point defects, and we gave an idea of how a color center-based measurement looks like and how it can be implemented in an actual sensor. We concluded the chapter by presenting the problem this thesis tries to address, namely how to improve the quality of the spin and optical properties of color centers close to the surface of nanofabricated structures. In the next chapters, we focus on the surface chemistry of diamond and present how the community currently treats the diamond surface and what we have learned about the origin of the surface noise so far. In chapters 4 and 5, we will introduce two different, new avenues to address the issue. The first is focused on the surface chemistry of the diamond and introduces the neutral SiV as a possible new candidate for nanoscale sensing. The second relies on a combination of top-down fabrication with bottom-up overgrowth to restore the surface properties of diamond nanostructures to those of as-grown diamond.

3. Commonly used surface treatments

In the last chapter, we discussed the potential and needs of color center-based sensing and explained why color center-based sensors work best at a minimal distance from the sample. As a direct consequence, the color centers need to be incorporated very shallowly and, therefore, close to the diamond surface. This proximity leads to several challenges. For simplicity, we will focus on the nitrogen vacancy in this chapter. When the NV center gets closer to the sample surface, it often appears to be unstable, with a broad ZPL and poor spin coherence times. These issues are attributed to fluctuating fields on the diamond surface and sub-surface lattice damage. There have been several theoretical and experimental studies as to which surface terminations and treatment protocols should perform best, concerning charge state stability and coherence times [51–54]. We will first give a brief overview of the existing insights on oxygen terminated diamond surfaces interacting with color centers and will investigate deeper the effects of oxygen plasma on the quality of the diamond surface and test promising post-treatments to restore it. Damage introduced during the NV creation will not be addressed in this work (see references [55, 56] for more details on this subject).

3.1. Motivation

Even though the NV center is one of the most studied color centers in diamond, its interaction with the diamond surface remains to be fully understood. The creation of photo-stable, shallow NV centers with satisfactory coherence properties is an outstanding challenge. Even more so for NV centers incorporated into diamond nanostructures. One can divide the challenge to create such NV centers into different aspects. To list the most demanding, the reduction in coherence time when NVs get closer to the sample surface, the difficulty to create NVs with a stable charge state close to the surface, and the reduction in coherence time when the diamond is structured by plasma etching for further applications. One common feature of all aspects is the fact that a deeper understanding of the diamond surface and its influence on NV centers is the first step to create NV centers with much better spin and optical properties. In this chapter, we will mainly focus on the last aspect, as it is essential for final devices relevant to nanoscale quantum sensing.

3.2. Surface treatments employed thus far

In this section, we will give a brief overview of the experimental and theoretical NV-surface interaction reported for different surface treatment protocols. We will focus

on oxygen-based termination techniques as they result in a diamond surface with a positive electron affinity, which is beneficial for the NV^- charge state stability [51].

3.2.1. Tri-acid treatment

The tri-acid treatment is due to its versatile applications, probably the most frequently used chemical treatment in the diamond nanofabrication. It is used to remove graphitized diamond, to prepare a reproducible starting point for nanofabrication, to clean off HF residues, to generally clean diamond and to ensure a predominantly oxygen terminated diamond surface [57]. With the term acid clean, we refer to a wet chemical etching based on a mixture of strong acids. More concretely, we boil the diamond in a 1:1:1 mixture of nitric, sulfuric, and perchloric acid. The boiling temperature depends on the sample geometry. For more fragile samples, the mixture is set to a temperature where the solution just starts boiling, whereas, for robust samples, the mixture is strongly boiling. The solution undergoes two color changes from transparent to yellow to transparent again. Depending on the temperature, this can take from 3 to 5 hours. After the second color change, the acid clean is considered finished. The sample is then rinsed with DI water and blow-dried with nitrogen. A detailed discussion of the method, including requirements necessary for safe handling of the chemicals can be found in Ref. [57].

The resulting surface chemistry consists of a rather undefined mix of different oxygen groups (hydroxyl -OH, ether-like C-O-C, carboxyl COOH, and carbonyl C=O) [58, 59]. It has been shown by various studies that oxygen termination stabilizes the negative charge state of the NV reliably due to a positive surface electron affinity of +1.7 eV [58, 60, 61]. There are, however, other studies that contradict this and report a strong upward band bending for chemical oxidized diamond surfaces. They attribute it either to incomplete oxidation of the surface (with the remaining binding sites being occupied by hydrogen) or to surface states near the valence band maximum (VBM) pinning the Fermi level [62]. The connection of band bending and charge state stability is discussed in Chap. 4. Theoretical studies offer a different explanation for the observed instability, namely deeply localized surface states in the band gap predicted for carboxyl groups and closely packed ether-like bonds [51]. A decrease in charge state stability results in either complete loss of the additional electron and with it the NVs sensing capabilities or in a less extreme case in a reduction of detectable ODMR contrast and as consequence sensitivity (see Chap. 2).

Besides charge stability, the coherence time is of major interest for sensing. Several studies employing NV-based measurement protocols using spectral decomposition in pulsed spin manipulation protocols found electronic spin impurities on the diamond surface, forming a 2D electronic spin bath [19, 63, 64]. The origin of this spin noise remains unclear. Most often incomplete oxidation of the surface resulting in unsaturated dangling bonds or adsorbents on the diamond surface of unknown origin and nature are suspected. Furthermore, several studies even suggest that this phenomenon is not constrained to diamond but also appears on other surfaces or interfaces [19, 65]. Mechanical properties, such as surface roughness, have been shown recently to have minimal influence on NV coherence [52]. The consent in the NV community is that the oxidation of the diamond surface by immersing the

diamond in strong acids results in less than optimal surface termination, which is detrimental to NV's coherence and optical properties.

3.2.2. Air anneal

Several studies have reported enhanced properties of the optical and coherence properties of NV centers after an air anneal compared to the acid clean [53, 54, 62].

The literature agrees on the positive development of the charge state stability. One explanation is a favorable composition of oxygen species. Simulation studies suggest the combination of -H, -OH, and C-O-C species at the diamond surface, as present at early stages of thermal oxidation, to be best suited for sensing applications with a (100) surface [51]. Another explanation is the increase in oxygen coverage of the surface by eliminating -H bonds [52, 62] or the removal of defects in the diamond lattice due to gentle etching [66].

Concerning the treatment's influence on the coherence times of NV centers, one finds contradicting information in literature. For instance, Ref. [52] reports no influence on the coherence time whereas Ref. [53] reports an improvement of up to a factor ten. One striking difference between the annealing protocols used is the process gas, combined with the work Sangtawesin et al. [67] this could be a plausible explanation for the contradicting observations. In their study, they correlate NV based T_2 measurements with surface spectroscopic techniques and find strong evidence for a modification of the surface chemistry from the unorganized mix present after the acid treatment towards a more ordered surface chemistry, dominated by ether bridges [67]. Another explanation could be that the increase in coherence observed by some authors stems from a layer of damaged diamond that is etched away by the anneal [66]. In this scenario, variations of the sample history or surface quality would lead to different results concerning the efficiency of the anneal.

For the experiments shown in this chapter, we adapt the protocol used in Ref. [53]. Before the anneal, the sample is cleaned in a Piranha bath (2:1 mixture of concentrated sulfuric acid and 30 % hydrogen peroxide). Then the sample is placed in a tube furnace and heated in air under atmospheric pressure to a temperature of 465° C. The sample is annealed for 4 hours. The ramping time to heat from RT to 465° C is 45 minutes and 1 h to cool down again. After the cool down, the sample is placed a second time in Piranha solution, rinsed in DI water, and blow-dried with nitrogen gas. The exact temperature is essential for efficient oxidation of the diamond surface and selective removal of amorphous carbon from the diamond surface [68].

3.2.3. Reactive ion etching: High bias plasma

Several different etch plasmas are employed to shape diamond. For the sake of simplicity, we will only discuss the two plasmas used during pillar fabrication in our group. The first one is a mixture of Argon and Chlorine, and the second one is a pure Oxygen plasma. More information about the nanopillar fabrication can be found in Chap. 5.

Reactive ion etching uses a strong radiofrequency electromagnetic field to ionize the molecule of an etching gas. Due to their lower mass, the electrons are accelerated much stronger than the ions, hitting the sample wafer and the sidewalls of

the camber. As the side walls are grounded, absorbed electrons are removed from the chamber. Electrons hitting the sample wafer result in a built-up of a negative voltage. The plasma is now slightly positively charged due to the higher concentration of positive ions. In an RIE system, the resulting DC bias is directly coupled to the applied RF power. For an inductively coupled plasma (ICP) RIE system, the DC bias field can be set separately, enabling a broader range of processes. In both cases, the ions in the plasma are accelerated toward the sample due to the bias field. Upon hitting the sample, the ions can either react chemically with the material of the surface or sputter the surface by transferring kinetic energy to surface atoms. Which process dominates depends on the type of ion and the applied bias. As diamond is one of the hardest materials, sputtering is a slow process. This can be used to etch contaminations on the diamond surface with high selectivity.

Argon is an inert gas and, as a result, the Argon-based plasma etches mostly by sputtering the sample surface. Chlorine, on the other hand, is highly reactive and adds a chemical component to the etch. This enables Chlorine-based plasmas to clean off Chromium, titanium, and silicon-based residues efficiently. Additionally, Argon-Chlorine plasma has been shown to etch diamond without roughening the diamond surface [69]. Oxygen, on the other hand, etches the diamond very well chemically and, depending on the applied bias, forms a combination of both aspects. The bias is needed to define the anisotropy of the etch.

A typical etch combines both plasma first an Argon-Chlorine plasma to remove residues that could not be removed with wet chemistry, then oxygen plasma to etch the diamond efficiently. If necessary additional Argon-Chlorine plasma steps can be added to clean off repositioned material in between oxygen etch steps. The combination of Argon-Chlorine and oxygen plasma results in a smother final etch surface compared to etch protocols purely based on oxygen plasma. Alternating steps of Argon-Chlorine and Oxygen-based plasma have been reported to reduce the surface roughness of diamond samples [18].

Various reports have shown that high bias plasma treatments damage the diamond crystalline structure and, as a consequence create charge traps and defects, which in turn cause a loss in coherence [66, 70]. It remains unclear if the deterioration of spin properties can purely be attributed to induced damage, if the surface termination is altered additionally or if another unknown effect is present. An example of such an effect would be the adsorption of radicals on the diamond surface or the implantation of ions [71].

3.2.4. Reactive ion etching: Zero bias plasma

Zero bias plasma, also referred to as soft plasma, is dominated by chemical etching and as a result, can be used to terminate the diamond surface or to remove layers of diamond slowly and gently. In our experiments, we worked until present only with an oxygen-based soft plasma, which has been reported to etch amorphous carbon selectively [66]. The process parameters used for this soft plasma are pressure 1 Pa, flux 60 sccm, ICP power 300 W, and RF power 0 W. In contrast to the high bias plasma, the etching is isotropic and of pure chemical nature. Various successful surface termination protocols relying on soft plasma have been reported, such as Nitrogen [72], Fluorine [73], Oxygen [61] and Hydrogen [61]. The slow etch rate and

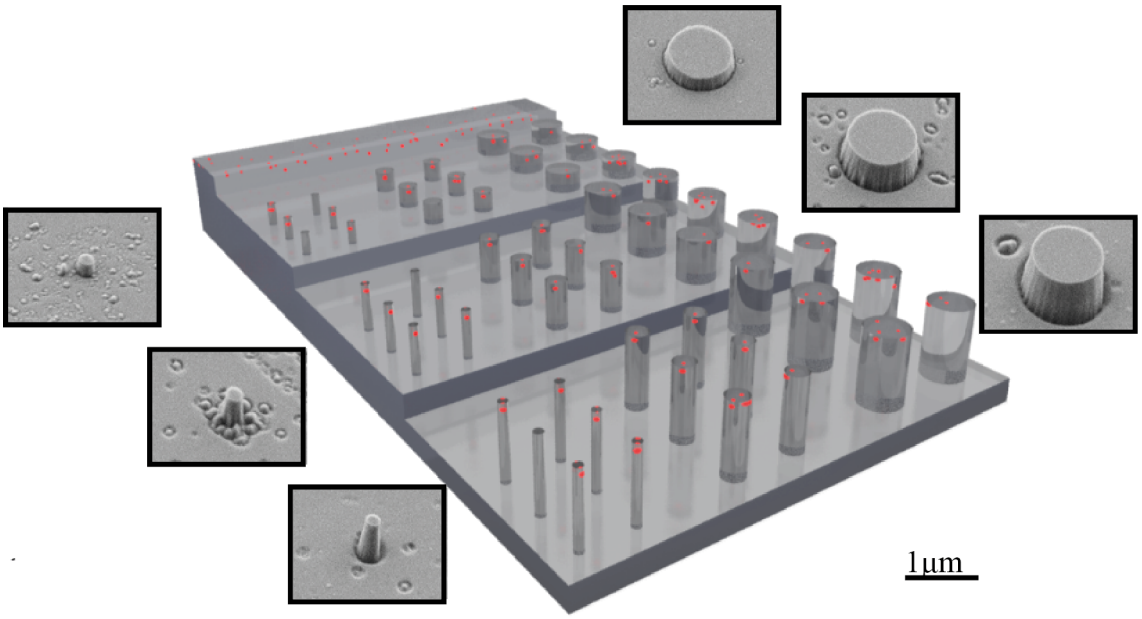

Figure 3.1.: schematic of the fabricated structures with different pillar diameters (200 nm, 500 nm and 1 μm) and etch depth (500 nm, 1 μm and 1.5 μm). The NVs inside the diamond lattice are symbolized by red points. Insets: SEM images of representative diamond pillars taken under a 45° angle.

strong selectivity to etch weak chemical bonds can be employed to etch damaged diamond material in a controlled way resulting in enhanced NV spin properties [66].

3.3. Nanofabrication plagued by loss in coherence time

To minimize the sensor-to-sample distance and enable a scanning measurement configuration using diamond spins, nanofabrication is mandatory. The current state of the art for this consists of all-diamond cantilevers formed by a thin diamond slab holding conically shaped nanopillars as local probes [74]. One of the drawbacks of this approach is the necessity of shaping diamond using different techniques. Commonly used are lapping, polishing, and plasma-based techniques. In this section, we present and discuss our observations regarding plasma-induced reduction in coherence time measured on shallow NV centers in fabricated nanostructures compared to coherence times measured on NV centers in bulk diamond.

3.3.1. Coherence properties of NVs hosted in diamond nano-pillars

Oxygen plasma is one of the most commonly used plasmas in diamond nanofabrication due to its etch selectivity. However, oxygen plasma related processes have been

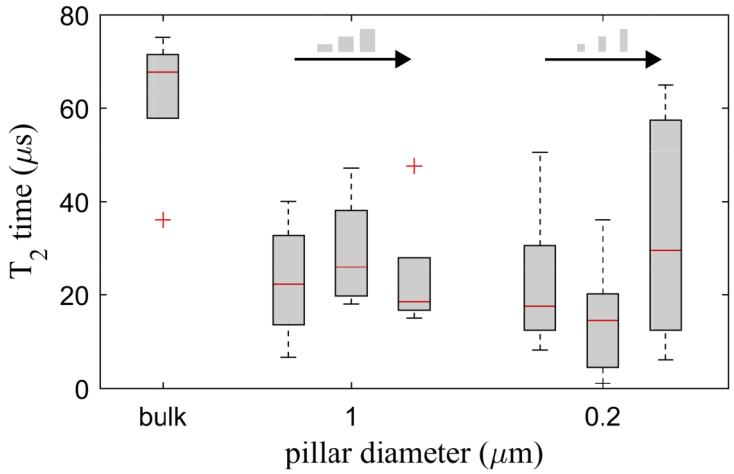

Figure 3.2.: Coherence times of NVs in nanopillars with different pillar diameters and lengths were measured and fitted, as described in Chap. 2. A representation of the fabricated structure can be found in Fig. 3.1. Statistics are built on the measurements of 5 NV centers per group considered (pillar diameter and etch time). The red line indicates the median and the bottom (top) edges of the box the 25^{th} (75^{th}) percentiles. The whiskers extend to the most extreme data points. Outliers, which are not considered, are marked with the symbol "+".

reported to be harmful to the coherence properties of shallow nitrogen vacancies. To systematically investigate this problem, we patterned a diamond test sample with three write fields of disks with different sizes (200 nm, 500 nm and 1 μm) and exposed them to oxygen plasma for varying time intervals (5, 10 and 15 minutes). The base material used is a single crystalline diamond with implanted NVs (^{14}N, 6 keV, $3*10^{11}$ ion/cm^2) at a depth of 9±4 nm [18]. More information about the fabrication process of nanopillars can be found in Sect. 5.2.1. A representation of the final device geometry can be seen in Fig. 3.1 with insets of SEM images of the widest and most narrow pillars fabricated, for all three pillar length.

To evaluate the effect of the plasma on the spin properties of NV centers near the diamond surface, we measured the T_2 times of 5 NVs per pillar diameter and etch-interval. As a reference, we measured 5 NV ensembles in an unpatterned area, subsequently referred to as "bulk". The results are visualized in Fig. 3.2. A clear reduction in coherence time is observed for all the NVs in pillar independent on pillar diameter or exposure time, compared to the NVs in bulk. On top of this, no significant difference can be detected between the different measurements on pillars. This uniformity indicates that the observed reduction of coherence times cannot be attributed to either spins or other surface effects at the sidewalls of the etched structures. If the reduction in coherence were caused by spins sitting on the sidewalls of the pillar, the area directly exposed to the plasma, we would expect the wider pillar to perform better as the NV has, on average, a higher distance from the side walls. An etch time-dependent reduction of spin coherence could be explained by the plasma creeping in between the etch mask and the top surface of the pillar. No such dependence was observed. However, we can not role out this

possibility entirely as the reduction could already have happened during the shortest time interval. Another explanation could be that the plasma damages the diamond though the etch mask. This hypothesis could be tested by measuring the coherence time of a sample entirely covered with an etch mask and exposed to 5 minutes of oxygen plasma. If no reduction in coherence time can be detected, we would suggest repeating the experiment with shorter etch intervals.

Summarizing from these first measurement we can deduce three main points: 1st the reduction in coherence time happens during the first 5 minutes of oxygen plasma and does not seem to get worse with more prolonged exposure; 2nd the top surface of the pillar appears to be the most likely source of decohering defects and 3rd a distance of 300 nm from the mask border to the NV spin is not enough to evade the effect.

3.3.2. Surface treatments: TEMED and air anneal

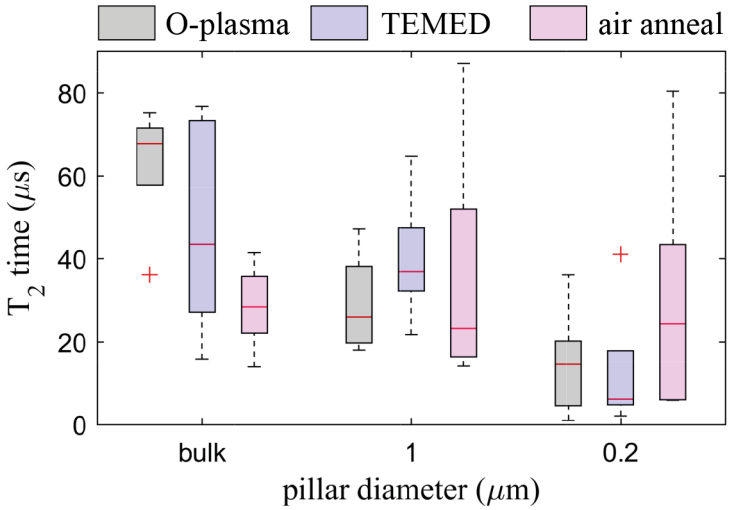

Figure 3.3.: The Coherence times of the same five NVs in the 600 nm long pillars were examined after different types of treatment (gray directly after fabrication, blue after immersion in TEMED and red after annealing in air). Five NVs in the bulk area were measured as a reference. As the density is too high to distinguish individual NVs, the data stem from different ensembles for all measurements. The red line indicates the median, and the bottom (top) edges of the box the 25^{th} (75^{th}) percentiles. The whiskers extend to the most extreme data points. Outliers not considered are marked as "+".

To deepen our understanding of the source of decoherence and to explore possible countermeasures, the same diamond was subsequently exposed to tetramethylethylenediamine and annealed in air. After each treatment, coherence time measurements were performed on the same NV centers, as in the previous section. The first treatment tested was immersion in tetramethylethylenediamine (TEMED) for one hour. TEMED is commonly used to stabilize free radicals. The idea of the treatment was to quench the plasma-activated surface and absorb Oxygen radicals.

The same 5 NVs in the 600 nm, long 200 nm wide pillars and the 600 nm long, 1 μm wide pillars were measured before and after immersion. For the bulk value we measured five new NV ensembles in the same area already investigated in the previous section. The result of the T_2 measurements can be seen in Fig. 3.3. The grey squares represent the T_2 times measured directly after fabrication, and the blue squares the T_2 times after TEMED treatment. In short, no clear tendency can be identified in the average T_2 time after the treatment. The mean got slightly better in the case of the 1 μm pillars and slightly worse for the NVs in the 200 nm pillars. One point to highlight is the significant increase in the variance of the bulk value. This increase could be a sign of a more heterogeneous diamond surface in this area. However, the measurements performed on the pillars did not continue the trend.

Next, we annealed the sample in air at a temperature of 465° C for 4 hours. The protocol and more information about the treatment can be found in Sect. 3.2.2. For evaluation, we measured the coherence time of the same NVs as for the TEMED treatment. The result is represented with the pink squares in Fig. 3.3. For the bulk, we again measured the coherence of 5 ensembles in the same area as before. We observe an apparent reduction in coherence time for the bulk value but also a reduced variance. We explain the loss in coherence with a potential miscalibration of the temperature during annealing, and as a result, a considerably higher etch rate [68]. Such a miscalibration would lead to the removal of more than just the defective diamond layers and as a result, very shallow NVs. It is to be noted that the variance is significantly reduced, indicating a rather homogeneous surface termination of the unstructured diamond. The results associated with nanopillars present a different behavior. Compared to the values before the anneal, some NVs show a definite increase in coherence time, others a slight reduction. The overall variance in the data points increased for both pillar fields. We assign this increased variance to two competing effects: the reduction in NV depth, leading to lower coherence times, and the removal of spin contamination or damaged diamond material, increasing the spin coherence. Comparing the maximum values for both pillar sizes, we see an apparent increase, for the 200 nm pillar the maximal coherence time measured directly after the fabrication improved due to the anneal by a factor of two.

We conclude that the anneal in air is a promising treatment to reduce plasma-induced surface noise. For the measurements taken on pillars, the average T_2 times found were comparable to the ones measured directly after the fabrication, despite reducing the NV depth considerably. To confirm this result, we propose to test the treatment using lower annealing temperatures or shorter annealing times to avoid the loss in spin coherence by removing an unnecessary amount of diamond. Further, the reproducibility needs to be verified and the etch rate calibrated carefully. Lastly these results are in good agreement with previous studies [53, 75]. Both predict an improvement in coherence time after annealing a diamond sample in oxygen-rich atmosphere but where Oliveira et al. [75] attribute it to the removal of defective diamond Lovchinsky et al. [53] associate it with a change in the surface chemistry.

3.3.3. Surface analysis by X-ray photo spectroscopy

The prolongation of coherence time is one of our main goals, therefore, it seems natural to use T_2 measurements as an evaluation criterion. The downside of these

measurements, however, is the long measurement time and limited surface area characterized per measurement. To complement our understanding of the surface chemistry and material properties of the diamond surface, we conduct a series of X-ray photo Spectroscopy (XPS) measurements. The technique probes the binding energy of the core level electrons of surface atoms by irradiating the sample surface with X-rays of a known frequency and measuring the number of escaping electrons and their kinetic energy. The anode emits X-rays when exposed to a high energy electron beam, with the electron source being the cathode. The most common cathodes are thermionic sources like W filaments, and the typical anodes are Magnesia K$\alpha, h\nu = 1253.6\,\mathrm{eV}$, or Alumina K$\alpha, h\nu = 1486.6\,\mathrm{eV}$ based. For further details we refer to [76]. For both energies, the detected electrons stem from the top 5 nm of the sample material. It is possible to increase the surface contribution of the measurement signal by tilting the sample and measure at a shallower angle [76]. The following equation connects the kinetic energy of the measured electrons E_{kin} and the energy of the X-ray photons $h\nu$.

$$E_{\mathrm{kin}} = h\nu - E_{\mathrm{bond}} - \phi \tag{3.1}$$

With E_{bon} accounting for the binding energy between electrons and nucleus relative to the Fermi level and ϕ the material-specific work function. As binding energies are atom specific, the material composition of the sample can be determined. If the individual peaks are measured with a high-enough resolution, even shifts in energy induced by chemical bonds can be resolved. When the ionization cross-section for different species is factored in the number of electrons measured from a specific atom-shell, are proportional to the number of atoms at the sample surface [76].

3.3.3.1. Chemical surface composition

We start our XPS measurement series by comparing three polycrystalline optical grade diamonds. The first diamond was measured in an untreated state, as received from E6, the second diamond was measured after treatment with our standard acid clean (see Sect. 3.2.1) and the third diamond after an air anneal (see Sect. 3.2.2). First, we measured full spectra, or "survey spectra", on all samples to identify the elements present. For the measurement, we used a Mg Kα source with an acceleration voltage of 10 kV, a current of 10 mA, and an energy step size of 0.5 eV. For a better signal to noise ratio, we averaged over three sweeps. All survey spectra in Fig. 3.4(a) were normalized to the intensity of the C1s peak, to enable a direct comparison of the remaining peaks. The O1s peak is larger on the acid cleaned diamond, and the air annealed diamond compared to the diamond measured as received. Further we detected a nitrogen-containing contamination on the as received diamond (Fig. 3.4(b)). This contamination was not detected on the acid cleaned or air annealed diamond. On the acid cleaned diamond, we found traces of Sulfur, which might indicate residuals of sulfuric acid remaining from the acid clean (see Sect. 3.2.1) even after rinsing the sample in DI water.

After identifying the material composition, we measured more highly resolved spectra for the elements of interest. Detailed spectra were recorded for the O1s and the C1s peak with a step size of 0.05 eV, and averaged over ten sweeps (see Fig. 3.5). As diamond is an insulator, the continuous removal of electrons during

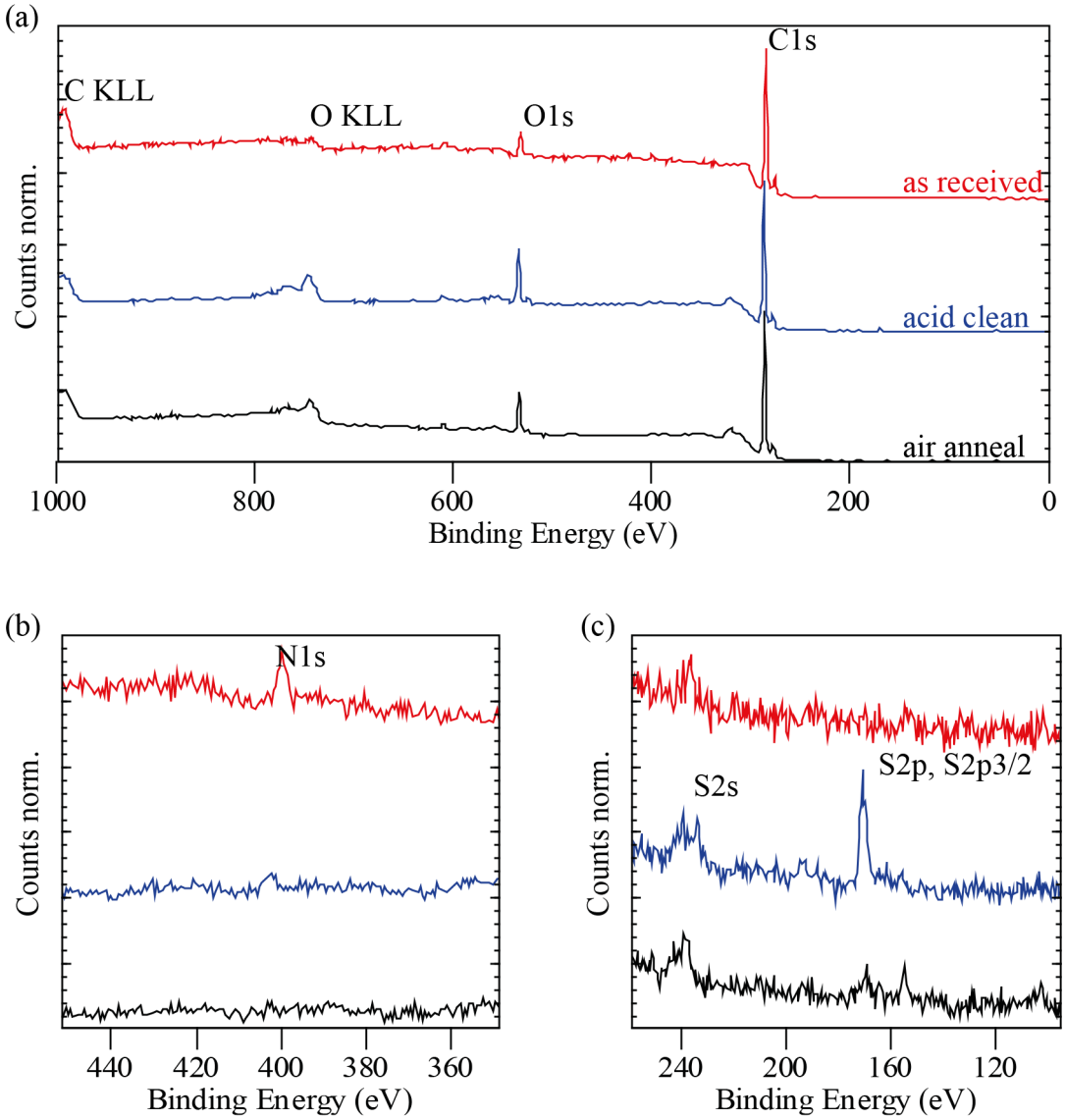

Figure 3.4.: (a) Survey spectra measured on optical grade diamond after different treatments. All survey spectra were measured with the parameters: source Mg Kα, acceleration voltage 10 kV, current 10 mA, energy steps size 0.5 eV, and averaged over three sweeps. All surveys were normalized to the C1s peak intensity. The labels O KLL, and C KLL mark the position of the oxygen and carbon Auger peak. (b, c) Zoomed-in parts of the survey spectra depicted in (a) to make small peaks caused by minimal contaminations visible. The color legend for all panels is the same and indicates the preparation of the sample measured red: diamond as received from E6, blue: diamond cleaned in an acid clean and black: diamond annealed in air.

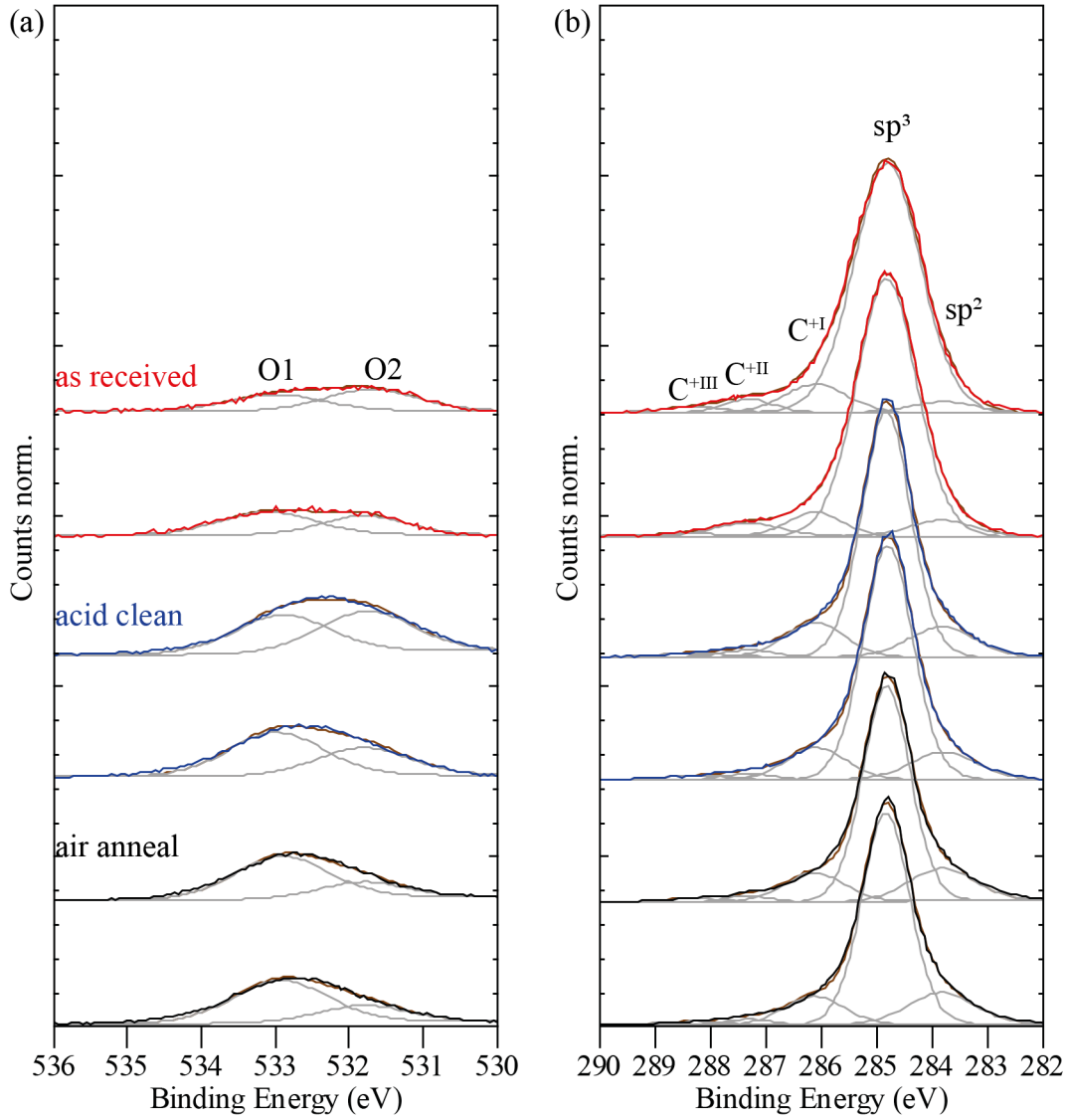

Figure 3.5.: Detail spectra of the O1s and C1s peaks measured on optical grade diamond after different treatments. All spectra were measured with the parameter: source Mg Kα, acceleration voltage 10 kV, current 10 mA, energy steps size 0.05 eV, and averaged over ten sweeps. The charging-induced energy shift was corrected by assigning the maximum of the C1s peak the energy 284.8 eV, and correcting the O1s spectra accordingly. Both peaks were fitted with a Gaussian Lorentzian peak shape (70 % Gaussian, 30 % Lorentzian). A legend explaining the sub-peaks used for fitting can be found in Tab. 3.1. The color code specifies the treatment of the sample, red: diamond as received from E6, blue: diamond cleaned in an acid clean and black: diamond annealed in air. On each sample two different areas were measured.

the measurement leads to a charged surface and a change in ϕ (Eq. (3.1)). This causes an offset in the measured XPS spectra. We corrected this energy shift by assigning the C-C peak the energy of 284.8 eV. For the analysis of the C1s peak components, we followed the example of Klauser et al. [77]. In their work, they compare different diamond surface oxidation methods by XPS spectroscopy. The C1s peak was fitted with five peaks assuming a Gaussian Lorentzian mixed shape and a Shirley background. The later is an algorithm to construct a background sensitive to changes in the data [78]. The same shape and linewidth were used to fit all the C1s sub-peaks, to ensure a reproducible fitting routine and comparability across the different spectra (Fig. 3.5(b)). In each spectrum, the highest sub-peak was assumed to stem from the sp^3 C-C bond, as this is the dominating species in a diamond sample. All other sub-peak positions were defined relative to the C-C sub-peak [79]. Towards lower energies, there was only one sub-peak accounting for the sp^2 bonds on the diamond surface with an energy shift of -1±0.1 eV from the C-C sub-peak. There were three sub-peaks shifted towards higher energies associated with oxidized carbon (Fig. 3.5(b)). The first one (C^{+I}) appears at an energy shift of 1.5±0.1 eV, and originates from single oxidized carbon C-OH or C-O-C. The second sub-peak (C^{+II}) has a shift of 2.5±0.1 eV, and is caused by double oxidation. Possible chemical groups are -O-C-O- or C=O. The third and final sub-peak (C^{+III}) is caused by carboxyl groups (a C with three bonds to oxygen) and has an energy shift of 3.5-4.5 eV. In Tab. 3.1 all components used to fit the detail spectra with the respective tolerances are summarized. These chemical shifts are normally used for organic polymers, but it is widely accepted that the energy shifts assigned also hold for carbon-oxygen groups on the diamond surface [80]. The authors of [80] give an overview of different XPS studies conducted on oxygen and hydrogen-terminated (111) and (100) diamond. For the C1s peak, the components used to fit are largely the same with differences in the detailed fitting routines. The situation for the O1s peak is less clear than for the C1s peak. As the shifts introduced by the various oxygen groups are very close together, and the sub-peaks are in general rather broad, many research groups concentrate on the C1s peak only. We fitted the O1s peak with two components based on standard values used in organic chemistry. We again used a Shirley background and the same mix of Gaussian Lorentzian line shape (70 % Gaussian, 30 % Lorenzian) as for the C1s peak. The positions of the sub-peaks were set to 531.5-532 eV for C-O single-bonded species and to 533 eV for C=O double-bonded components (see Fig. 3.5(a)).

For every sample, two detail spectra were measured on different positions of the diamond sample. The respective data sets are shown in the same color code (red: as received, blue: acid clean and black: air anneal) in Fig. 3.5. First, we note that all samples appear rather uniform because of their very similar chemical composition. Second, the spectra measured on samples treated with acids and air anneal have a much higher signal O1s peak. This increase indicates higher surface coverage and, therefore, a more complete surface termination. Another point to note is the presence of the sp^2 peak: this component is more pronounced for the acid cleaned and the air annealed sample, compared to the as received sample. Comparing the C1s sub-peak composition of the chemical oxidized and thermally oxidized sample, no apparent differences can be seen. In the O1s peak, the O2 component appears smaller for the sample annealed in air compared to the O2 component of the acid

	C1s				
Component	sp^2	sp^3	C^{+I}	C^{+II}	C^{+III}
Energy shift (eV)	-1 ±0.1	0	+1.3 ±0.1	+2.5 ±0.1	+3.5-4.5
Species	C=C	C-C	C-OH, C-O-C	-O-C-O-, C=O	-COO-
	O1s				
Component	O1	O2			
Position (eV)	533	531.5-532			
Species	C-O	C=O			

Table 3.1.: Components used to fit the C1s and O1s detail spectra. For each peak the relative position with respect to the sp^3 C-C peak or the energy value assumed and the corresponding chemical groups are listed.

clean sample. For more quantitative statements, we integrated over the areas of the sub-peaks and displayed the normalized areas in a bar plot (see Fig. 3.6).

The atom percentage of the individual components was calculated by integrating the area of the fitted peaks. The ratio between the C1s and O1s peak carries information about the surface coverage of the termination. The calculated ratios are 0.048 for the as received, 0.11 for the acid cleaned, and 0.094 for the oxygen annealed sample. Here the increase of the amount of oxygen on the annealed and acid cleaned sample compared to the as received one is even more evident. The lack of difference in the C^{+I}, C^{+II} and C^{+III} components, representing the different oxidation degrees of carbon, suggests that the surface terminations are too similar to differentiate by XPS. This is consistent with the results presented by Ref. [77] but contradicts Ref. [67]. One possibility to study the surface chemistry in more detail would be to measure angular XPS to increase the surface sensitivity or to switch to FTIR or another surface-sensitive technique. The O1s peak, on the other hand, shows a reduction of the O2 component for the air annealed sample. However, due to the many different species contributing to the O1s peak, no reliable source could be found to explain the different components for diamond surface reconstruction. All O1s peaks measured are rather broad, indicating the presence of multiple different functional groups. We can presume a decrease in C=O bonds, but as the C1s components did not mirror this behavior, we refrain from any conclusion.

The results of this work show significant discrepancies with Ref. [67]. There, differences between the wet chemical and thermally oxidized diamond surfaces were examined. The most obvious difference is the missing O1 sub-peak and the general peak position and size of the O1s peak in [67]. Additionally, we find a higher oxygen coverage on our samples. Both observations are surprising as we use very similar preparation techniques. One explanation could be a different surface reconstruction due to the pure oxygen atmosphere the authors of [67] used during their anneal. We exclude the possibility of surface contaminations as they would have appeared in the survey spectra.

3.3.3.2. Material properties

After the difficulties of differentiating between the oxygen species and the inconsistent information found for the O1s peak, we decided to use a hydrogen plasma to

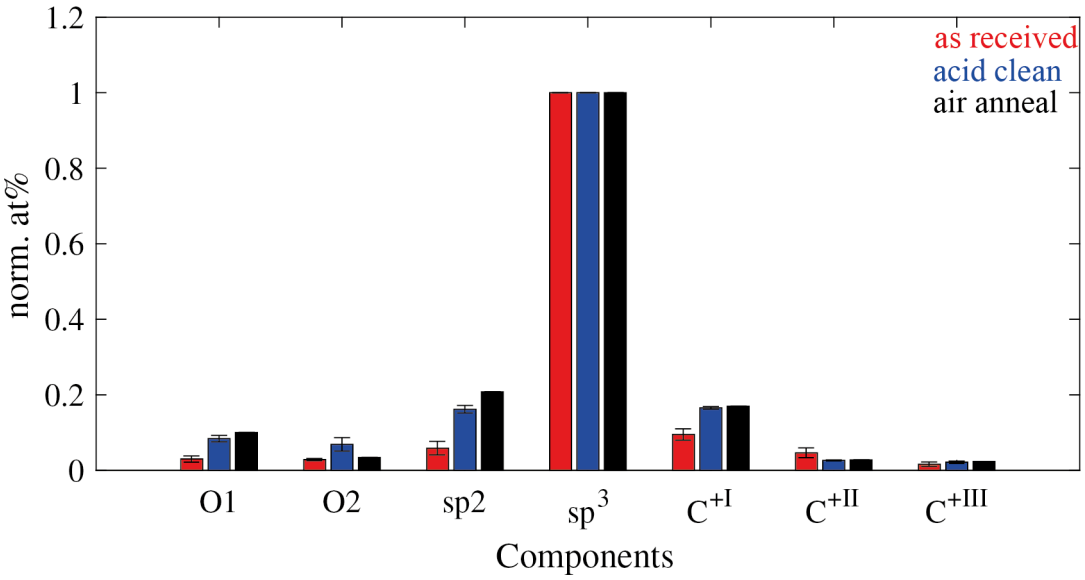

Figure 3.6.: Bar plot of the atomic percentage of the different components measured. The spectra considered can be found in Fig. 3.5. All the components were normalized with respect to the amount of C-C measured to facilitate the comparison. The color code indicates the sample treatment. The error bar gives the variation between two sample areas measured. A legend of the components can be found in Tab. 3.1

prepare an oxygen-free reproducible starting point for our next measurement series and to focus on the C1s peak alone. For this, we used a set of four polycrystalline diamond samples and exposed all to a hydrogen plasma with the parameters RF power 100 W, gas flow 30 sccm H_2, V_{Bias} 298 V and a pressure of 1.8 Pa. We then removed one sample and treated the remaining three with an oxygen plasma for 10 seconds, we removed another sample and turned the plasma on for another 50 seconds. The plasma parameter used are RF power 10 W, gas flow 30 sccm O_2, V_{Bias} 80 V and a pressure of 0.97 Pa. After which, the 3rd diamond was removed, and the last sample was exposed for 4 more minutes. A schema illustrating the sample preparation can be found in Fig. 3.7(a). All four samples were measured in the same run using the experimental parameters Al Kα source with an acceleration voltage of 10 kV, a current of 10 mA, and an energy steps size of 0.05 eV. We changed from the Mg source to Al as this is combined with a monochromator and gives a better resolution of the peak shape. The C1s spectra were averaged over 12 sweeps. The resulting XPS detail spectra can be seen in Fig. 3.7(b).

A detailed analysis of the development of the C1s peak with increasing exposure to oxygen plasma leads us to three main conclusions. First, the C1s peak of the sample exposed to hydrogen plasma only still shows the C^{+I} component associated with C-O bonds. We conclude that the hydrogen plasma did not eliminate the oxygen termination from the diamond surface. A reason could be that the sample was not heated up as reported by other references using a hydrogen plasma for surface termination [31]. The second observation is about the peak shape of the C1s peak. With increasing exposure to oxygen plasma, it appears to become more narrow. The

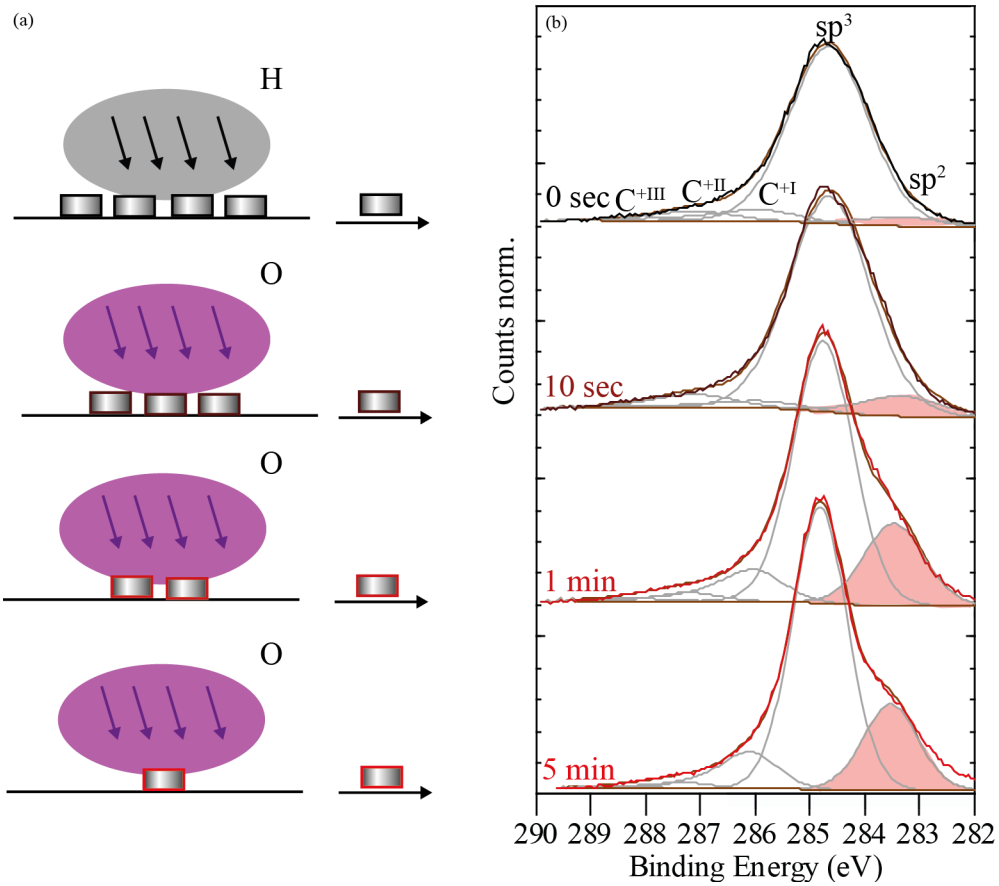

Figure 3.7.: (a) Schematic of the sample preparation used. In total, four samples were exposed to a Hydrogen plasma. After 2 min the first sample was removed. The remaining three samples were exposed to an oxygen plasma, after 10 seconds one more sample was removed. The two remaining samples were exposed for 50 seconds, one was taken out and the last one was exposed for another 4 minutes. (b) C1s detail spectra measured on optical grade diamond after increasing exposure to oxygen plasma. All spectra were measured with the following parameters: source Mg Kα, acceleration voltage 10 kV, current 10 mA, energy steps size 0.05 eV and averaged over ten sweeps. The charging induced energy shift was corrected by assigning the maximum of the C1s peak the value 284.8 eV. The component associated with sp^2 bonds is colored in red.

width of the C1s peak has been reported to correlate with disorder [81], possibly due to the presence of C-H bonds [77]. A third observation is an appearing shoulder associated with the sp^2 hybridization of carbon or amorphous carbon. We assume it to be caused by damage induced by the oxygen plasma. This, in turn could explain the decrease in coherence time found in our T_2 measurement as seen in Fig. 3.1. The shoulder does not seem to increase after the first minute of plasma exposure. This observation is consistent with our findings in the T_2-based measurement.

Inspired by the results of Ref. [66], we implemented the soft oxygen plasma in an attempt to reduce the sp^2 related sub-peak. In their work, they showed a correlation between this sub-peak and damage in the diamond surface layer. They etch the damaged layer with oxygen-based zero bias plasma and measure a positive influence on NV coherence.

The sample used for this measurement was a 8x8mm polycrystalline diamond treated with 5 min Argon-Chlorine and 5 min Oxygen plasma with the parameters used to etch nanopillars (see Sect. 5.2.1 or [18]). Half of the diamond was then covered with a quartz platelet, and the uncovered area was etched for another 30 minutes using a soft oxygen plasma (Sect.3.2.4). The soft oxygen plasma should be purely chemical and as such similar to a thermal anneal, but in a better-controlled environment. In addition to that, such a routine holds the promise of a more straightforward implementation in our fabrication routine.

After the sample preparation XPS spectra were measured on both the uncovered(Fig. 3.8(b) green) and covered area (Fig. 3.8(b) red). In Fig. 3.8(a), a survey spectrum measured on the uncovered area can be seen. The C1s and O1s peaks are expected as we measure an oxygen terminated carbon species. The F1s peak, on the other hand, was unexpected but can be explained by HF residues from the cleaning process or from the ICP chamber used to etch the sample as there are also CF_4 processes run in the chamber. All spectra were normalized to the peak maximum of the C1s peak. As diamond is insulating, we corrected the charging induced shifts by taking the C1s peak as reference peak, assigning it the value 284.8 eV. Comparing the C1s and O1s peaks before and after the soft oxygen plasma, there are two main points to highlight (Fig. 3.8(c)). First, the O1s peak is drastically reduced in size, and second, the shoulder on the C1s peak, the pink area in Fig. 3.8(c), shrinks. As the shrinking peak is associated with amorphous carbon, this is a clear sign of the successful removal of parts of the damaged diamond surface. The decrease in oxygen is explainable by a reduction of the surface roughness and, therefore, effective surface area. More tests are necessary to determine if the remaining amorphous carbon layer can be reduced even further, by optimizing the plasma parameters, and to verify the correlate between the observed decrease in coherence time and the peak intensity of this shoulder. For both experiments, a careful study of the plasma reproducibility and the etch rates is mandatory to be able to control the final depth of the NVs in a reliable and reproducible way. As our machine is not designed for this application, the first attempts to do so proved somewhat challenging.

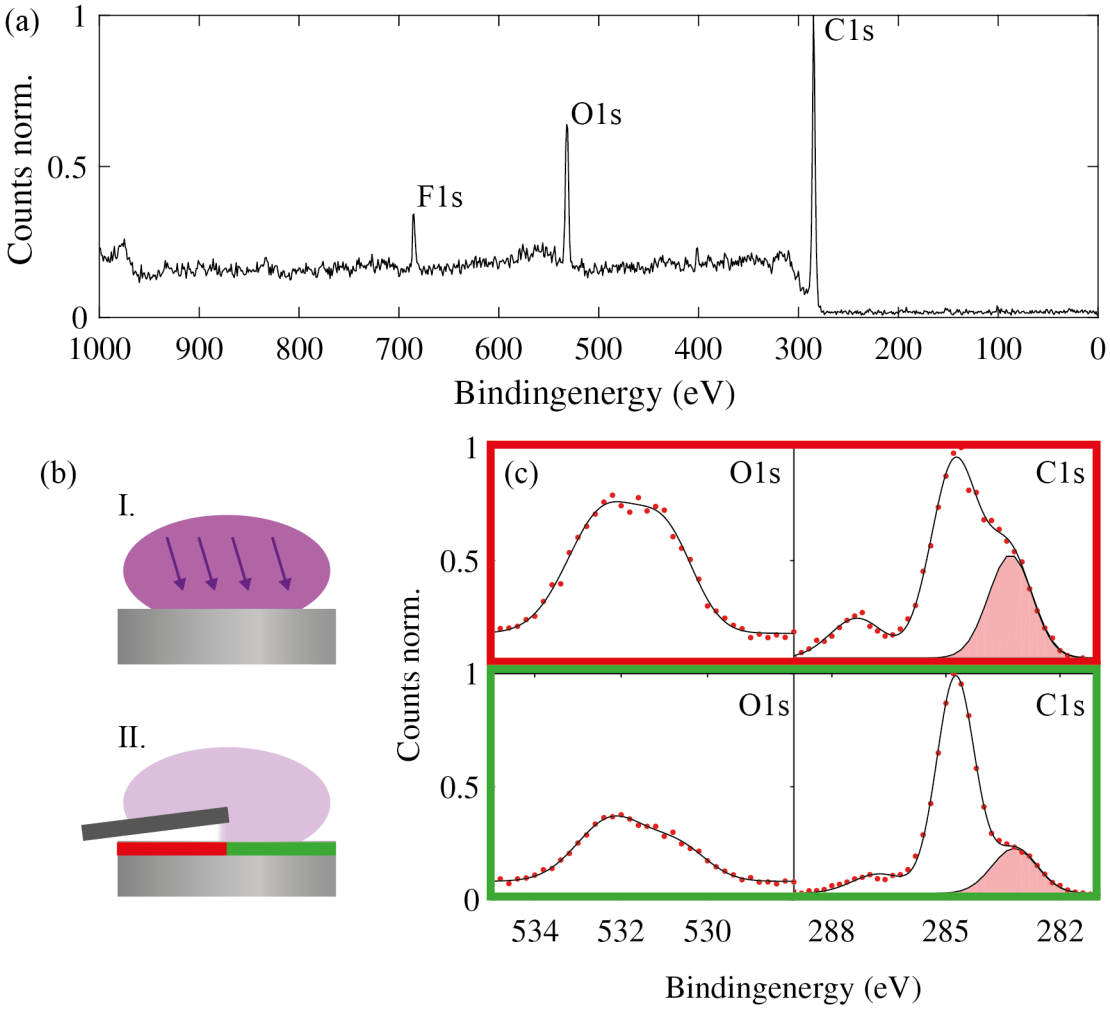

Figure 3.8.: (a) Full range X-ray spectrum of a diamond surface exposed to a harsh etching plasma. (b) Schematic of the sample fabrication. I. exposure of the whole surface with a high bias plasma. II. protection of one area (red) by a quartz platelet and exposure of the other area (green) to a 0 bias "soft" oxygen plasma. (c) Finely resolved spectra of the O1s and C1s peak measured on the two parts of the diamond i.e. the half exposed to a harsh etching plasma only (red area, top panels) and to the second half to which an additional soft plasma (green area, bottom panels) was applied. All spectra were measured with the parameters: source Al Kα, acceleration voltage 10kV, and current 12 mA. The survey spectra were averaged over six sweeps and measured using a step size of 1 eV. The detail spectra were averaged over ten sweeps and an energy step size of 0.2 eV was used

3.4. Summary and outlook

In this chapter, we present a brief overview of the theoretical predictions and experimental findings reported by other groups concerning the effect of different oxygen-based surface treatments on NV centers. In the second part, we employ two methods, namely spin coherence time measurements of incorporated NV centers and X-ray photo spectroscopy, to investigate the effect of oxygen plasma and different treatments on the diamond surface.

In the first experiment, the sensing capabilities of the NV center are employed, using the change in coherence time observed when the diamond surface is exposed to oxygen-based etching plasma, to investigate the source of decoherence reported [66, 70]. We find evidence that the affected diamond surface is the top surface covered by etch mask, that the damage is induced during the first 5 minutes of plasma exposure and does not appear to get worse with longer exposures. We identify two possible scenarios: First, the plasma is creeping in between the etch mask and the sample surface, and second the diamond is damaged through the etch mask. The identification of the cause is essential to find efficient solutions as any change in the process bears the risk of introducing new sources of decoherence and new difficulties. If the plasma is creeping in between the mask and the diamond surface, an additional adhesion layer could help. A possible avenue to explore there is the recently published use of a silicon-based adhesion layer [82]. If the diamond is damaged through the mask, a possible solution could be to transfer the mask into a metal layer through a wet chemical process and then use this reinforced mask for plasma etching. To differentiate between the two suggested mechanisms we suggest two experiments: First expose a diamond surface entirely covered with an etch mask to 5 minutes of oxygen plasma and compare coherence times before and after second repeat the measurement as performed for this thesis with shorter time intervals we suggest 20, 40 and 60 seconds.

In the second part of the experiment, we investigated treatments to recover the NV spin properties. We found the immersion in TEMED to have no or a negative effect and the anneal in air to be a promising technique. The average coherence time measured on pillars was after the treatment comparable to the coherence time measured in bulk. We could not see an apparent increase in coherence time compared to the values measured directly after fabrication, presumably due to a poorly calibrated temperature, resulting in the removal of more diamond than necessary. To asses the potential of this technique, it is necessary to first optimize the annealing temperature to prevent diamond etching and then repeat the experiment.

The second set of experiments used X-ray photo spectroscopy (XPS) to investigate the diamond surface. We found XPS very useful in detecting contaminating species or graphitized carbon layers on the diamond surface but challenging to utilize to determine the surface chemical composition reliably. It remains unclear if the difference between wet chemical oxidized surface and surfaces treated by annealing in air are chemically too similar or if the technique is not sensitive enough. To investigate this further, we suggest measuring XPS at an angle to increase the surface sensitivity or to supplement the measurements with other surface-sensitive spectroscopic methods like Fourier transformed infrared spectroscopy (FTIR). This observation contradicts the theory of wet chemical oxidation having a smaller oxygen coverage

than the air anneal surface [62, 67].

In the second set of measurements, we investigated the influence of oxygen plasma on the diamond surface and found clear evidence of the formation of an amorphous carbon layer. This observation of plasma-induced damage is consistent with previous reports [75]. Further, we established a soft oxygen plasma protocol and observed a reduction of the signal caused by amorphous carbon. It proved very challenging to find parameters creating a plasma with a reproducible and stable bias. We attribute this to the fact that our ICP is not designed to be run without bias applied. If these challenges cannot be overcome, the annealing in air or oxygen atmosphere could be considered as an alternative to reduce damage in the subsurface crystal lattice by removing the top layers.

In the next step, we want to correlate both measurements to verify that the existence of the sp^2 related sub-peak is connected with the observed loss in coherence time. Additional to the coherence time measurements, we propose to measure charge state dynamics to gain a more complete picture. We suggest to conduct this comparison on an SCD diamond with fabricated pillars containing single NV centers and to measure T_2 times and XPS spectra directly after the fabrication and after the treatment with soft oxygen plasma or alternatively air or oxygen anneal.

We further believe that a similar experiment comparing the surface chemistry and coherence time of implanted NV after an anneal in air and after an anneal in pure oxygen atmosphere to be of interest to the community as this difference in atmosphere could explain the controversial reports on the effect of the treatment. We would set up the experiment in the following way: sample fabrication, acid clean, air anneal, tri-acid clean, oxygen anneal with XPS, charge state, and coherence time measurements after each tri-acid clean and annealing step.

A further promising experiment would be the investigation of the adaptability of the findings of Ryan et al. on nanodiamonds to single-crystalline diamond pillars [83]. They reported an increase in spin-lattice relaxation time measured on nanodiamonds treated with borane compared to nanodiamond treated with a thermal anneal. Also, other surface terminations like Fluorine or Nitrogen termination could be interesting. A more homogeneous base termination is better suited as a starting point to implement new termination protocols. A homogeneous termination would also simplify the analysis of the surface chemistry and deepen our understanding of the spectroscopy methods. Many of the reported termination protocols are based on a hydrogen termination as a starting point. This led us to the decision to investigate the hydrogen-terminated diamond surface next.

4. Hydrogen termination and its influence on color centers

Hydrogen termination is a widely used surface termination in diamond electronics as it causes surface conductivity based on a two-dimensional hole gas in the top 1-3 nm of the diamond surface [84, 85]. This conductive layer is a result of band bending, which can be used to stabilize different charge states in diamond, which could not be observed with oxygen-based terminations. In the first part of this chapter, we explain the mechanism causing this band bending and how the bending influences the charge states of color centers in diamond. Followed by a presentation of our termination protocol, including XPS measurements and fluorescence measurements of shallow NV and SiV centers to confirm the effectiveness of H-terminations. In the last part of the chapter, the influence of temperature and the presence of surface adsorbed water are investigated, utilizing color center-based fluorescence and Kelvin Probe Force Microscopy measurements.

4.1. Motivation

In the last chapter, we gave an overview of the work done on oxygen terminated diamond, comparing the most frequently used preparation methods. In the second part, we presented coherence time and XPS measurements of different oxygen surfaces. The treatment by annealing the sample in air and the soft oxygen plasma appeared promising for coherence time prolongation, but it proved challenging to detect the chemical changes by XPS consistently. As various termination protocols use the hydrogen-terminated diamond surface as a starting point, we decided to investigate this termination next [86, 87]. An additional advantage for the hydrogen termination as a starting point is that C-H groups do not introduce a resolvable chemical shift in the XPS carbon detail spectra. Therefore the hydrogen termination is an ideal reference to detect chemical changes.

An additional benefit of the termination is the already mentioned impact on the energy bands and the possibility to observe color center charge states that are not stable upon creation in the commercially available undoped diamond. This opens up two exciting opportunities, first the possibility to stabilize the neutral Silicon vacancy center, a highly promising defect for quantum communication applications [48], and second, to gain more insights about the role of the diamond surface when it comes to charge state stability.

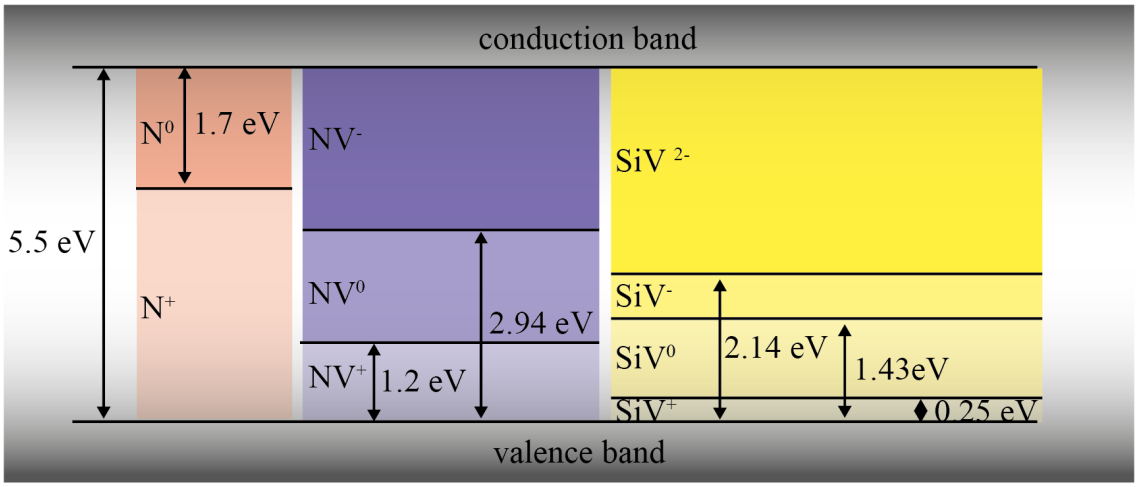

Figure 4.1.: Band diagram of diamond with the charge transition levels of the different nitrogen and silicon vacancy charge states. The energy levels observed by Schreyvogel et al. [88] are used for the Nitrogen vacancy and the predictions by Gali et al. [89] for the SiV. The range in which the charge states of the different color centers are stable are colored with different intensities. Red is used to encode the charge states of the P1 (N center), blue for the NV and yellow for the SiV.

4.2. Band-bending and charge states

To understand band bending, one needs to consider the electron energy states in a material. In solid-state physics, band diagrams are often used to visualize changes in Fermi energy and band edges as a function of position. A common insulator can be described by a valence band, a conduction band, and the energy gap between them. The mentioned band edges are then the valence band minimum and the conduction band maximum. The Fermi energy gives the energy level up to which the electronic states are filled at a theoretical temperature of zero Kelvin. If the Fermi energy is higher than the conduction band maximum, the conduction band is filled with electrons, and analogously if the Fermi energy is lower then the valence band minimum, the valence band has empty states, holes. Both cases cause the material to be conducting. If the Fermi level is located within the band gap, as is the default state for diamond, the valence band is filled, the conduction band is empty, there are no free charge carriers, and therefore the material is insulating.

An illustration of the band structure of diamond, including the energy levels of the charge states of the NV and SiV center can be seen in Fig. 4.1. In addition to the color centers, also the energy level of a single Nitrogen donor in the diamond lattice is represented. The energy level of the nitrogen is largely accepted. For the NV we chose the values measured experimentally by Ref. [88]. They are in good agreement with theoretical prediction, which put the $NV^{-/0}$ and $NV^{0/+}$ charge transition levels at E_V+2.67 eV and E_C - 4.46 eV respectively [90]. For the $SiV^{-/0}$ charge transition level, the situation is less clear. Different energy transitions are reported, for example, E_V + 1.5 eV in [89] and at E_C -1.9 eV in [91]. For the scope of this thesis, we assume the values, as depicted in Fig. 4.1, to be correct. Hence assuming we have a sample with both NV and SiV defects, the negatively charged

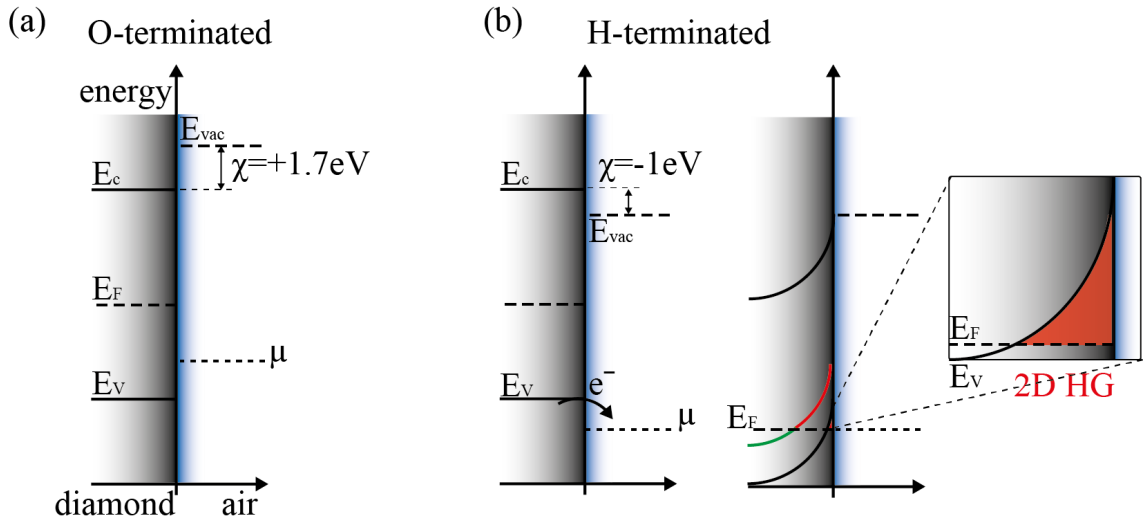

Figure 4.2.: (a) Energy band schematic of oxygen terminated diamond, with a positive electron affinity $\chi = 1.7\,\text{eV}$. The Fermi level is defined predominantly by the dopant present in the diamond lattice. (b) Mechanism leading to surface conductivity present for hydrogen-terminated diamond. The negative electron affinity of hydrogen-terminated diamond $\chi = -1\,\text{eV}$ shifts the bands upwards, such that the energy level of the chemical potential μ of the adsorbed water layer lies now below the valence band minimum. The equilibration of the chemical potential of the electrons in diamond and water leads ultimately to band bending (more detail in the text). The modified energy of a not specified color center charge state is visualized with the colored line. If the state lies above the Fermi energy, it is unoccupied (red) and occupied otherwise (green). The inset zooms in on the two-dimensional hole gas (2D HG) present on the diamond surface. This figure is recreated after the reference [61].

SiV could only be observed if a majority of the NV is already in a neutral charge state.

In undoped diamond the Fermi level is located at E_V +2.7 eV in the middle of the band gap [62]. As a consequence, a NV center in this environment would be in its neutral charge state since the transition energy $\text{NV}^{-/0}$ lies above the Fermi level. This donor and acceptor free diamond lattice containing a single NV is a pure "Gedankenexperiment". In actual samples, nitrogen is a nearly omnipresent impurity, either due to the creation process of the NV or incorporated during diamond growth (electronic grade provided by Element 6 $[\text{N}]^S < 5\,\text{ppb}$). This additional nitrogen present in the diamond acts as a dopant and influences the Fermi level. If nitrogen is the major impurity, the Fermi level is expected around E_C- 1.7 eV [92]. Collins et al. [92] find in their calculation that the Fermi level is predominantly defined by the concentration of the major impurity present. Further, the authors of [92] explain the existence of different NV charge states in one diamond sample by different distances to the next donor or acceptor. When working with color centers close to the diamond surface, in addition to the donor present in the diamond lattice, one has to take the surface termination into account as it can lead to band bending.

A good example of the influence of surface termination on the properties of the

sub-surface diamond lattice is the hydrogen termination. Fig. 4.2 illustrates the difference between oxygen terminated diamond with a positive electron affinity and hydrogen-terminated diamond with a negative electron affinity. The electron affinity χ of a material is defined in solid-state physics as the amount of energy gained when an electron is moved from the vacuum outside the material to the conduction band minimum inside the material. Therefore, if the electron affinity is negative, energy is gained when a conduction electron is moved out of the material. The negative electron affinity of hydrogen-terminated diamond causes a shift in energy levels putting the chemical potential μ of the aqueous wetting layer covering the diamond surface below the valence band maximum. As a result, electrons are depleted from the diamond until the chemical potential of the electrons in the diamond and the water layer equalize. This depletion leads to an accumulation of positive charge in the diamond and negative charge in the adsorbed water layer, which leads to the bending of the energy bands. The valence band rises above the Fermi level, introducing a two-dimensional hall gas (2D HG). The Fermi level can be defined as the total chemical potential of the electrons. The described charge transfer is possible because of the presence of an acceptor state outside of diamond laying lower in energy as the conduction band maximum [93]. This acceptor state is believed to be formed by a reduction of atmospheric oxygen or other atmospheric contaminants in the adsorbed water layer [94]. This mechanism is named "transfer doping model" and is a widely accepted explanation of the surface conductivity.

How far the band bending reached into the diamond depends mainly on the donor concentration present. Newell et al. [95] confirm a strong correlation with nitrogen concentration in their simulation and find a complete charge state conversion to the neutral charge state for the top 50 nm of diamond material, assuming a concentration of $10^{19}/\mathrm{cm}^3$ NV^-. Similar behavior has been reported experimentally by Hauf et al. [61] studying the NV charge state of different implantation depth and doses. With our standard implantation parameter (1e11 cm^{-2}N 12 keV, 7° implantation angle), resulting in NVs located ∼20 nm below the surface, we expect to find predominantly NV^0 or even NV^+.

4.3. Hydrogen termination of the diamond surface

Hydrogen termination is a commonly used technique in the field of diamond electronics. As discussed in the previous paragraph, it leads to a two-dimensional hole gas at the diamond surface and hence, a locally confined conductive channel. This opens the possibility to directly pattern conductive circuits on diamond, just by locally changing the surface chemistry. For this to be possible, the termination process needs to be compatible with e-beam lithography or another scalable nanofabrication process. As a consequence, the most commonly used technique to achieve H-termination is plasma-based. However as already seen in the Chap. 3, plasma can cause damage to the diamond structure. Also, the typical recipe involves heating during the plasma, which is technically not possible in our plasma chamber. Because of this, we decided to focus on a technique often used for nanodiamonds employing thermal annealing of the substrate in hydrogen atmosphere [96].

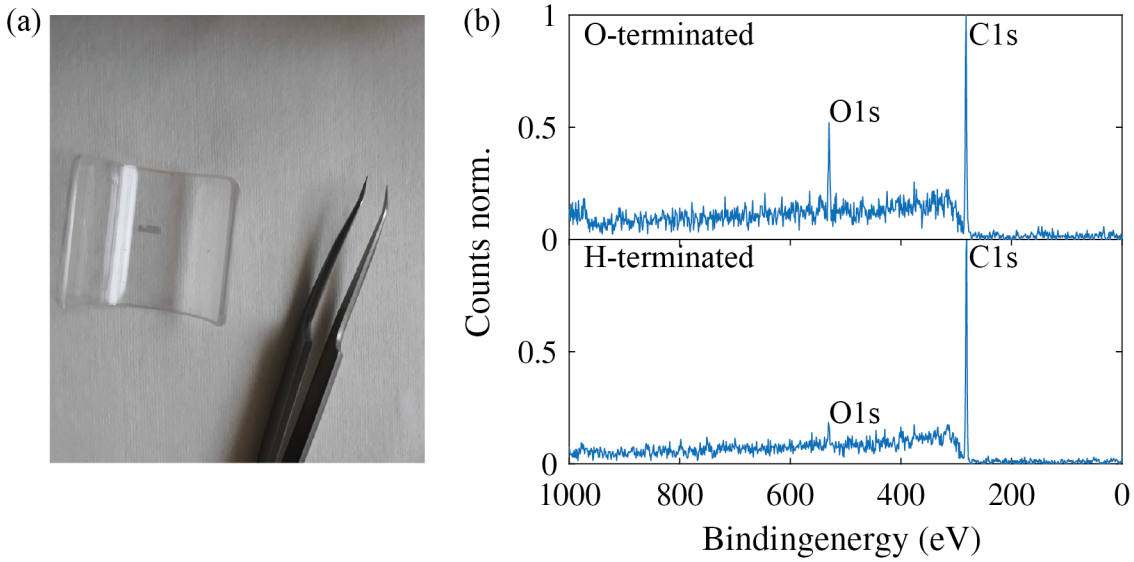

Figure 4.3.: (a) Picture of a thin diamond sample on the quartz boat before the anneal in hydrogen atmosphere. (b) XPS survey spectra of oxygen (top) and hydrogen (bottom) terminated diamond surface, with labeled C1s and O1s peaks. To enable better comparability of the C to O peak ratio, the measurement counts were normalized to the C1s peak amplitude.

The diamond was first cleaned with a tri-acid clean followed by a solvent clean to ensure a reproducible starting point, free of possible residues. Next, the sample was placed on a quartz boat (Fig. 4.3(a)) and inserted into the oven. To ensure an oxygen-free atmosphere, the whole system was purged for ten minutes with Argon gas. In the next step, the sample was heated under hydrogen atmosphere to 750° for 6 hours and then cooled down in a mixture of hydrogen and argon gas. A detailed recipe can be found in Appendix A.1.

As the temperature of 750°C is not high enough to dissociate hydrogen [97], it is commonly assumed that the termination protocol is based on thermal dissociation of functional groups on the diamond surface [98]. This creates active surface sites, in the form of dangling bonds and unsaturated carbon-carbon bonds, which have the power to dissociate molecular hydrogen and form -CH groups [96]. A similar mechanism has been reported for the thermal hydrogenation of diamond nano particles [99].

To assess the success of the surface termination, we measured XPS spectra before and after the termination Fig. 4.3(b). The O1s peak is strongly reduced after the termination. The remaining oxygen measured could stem from organic surface contaminations, adsorbed water, or an imperfect surface termination. As the hydrogen atom has no core electrons, it cannot be detected by XPS [100].

4.3.1. NV centers under Hydrogen terminated surfaces

To test the previously reported charge state conversion from NV^- to NV^0 (and possibly NV^+) as well as the reversibility of the process, an implanted diamond was characterized optically by confocal microscopy after different surface treatments. The

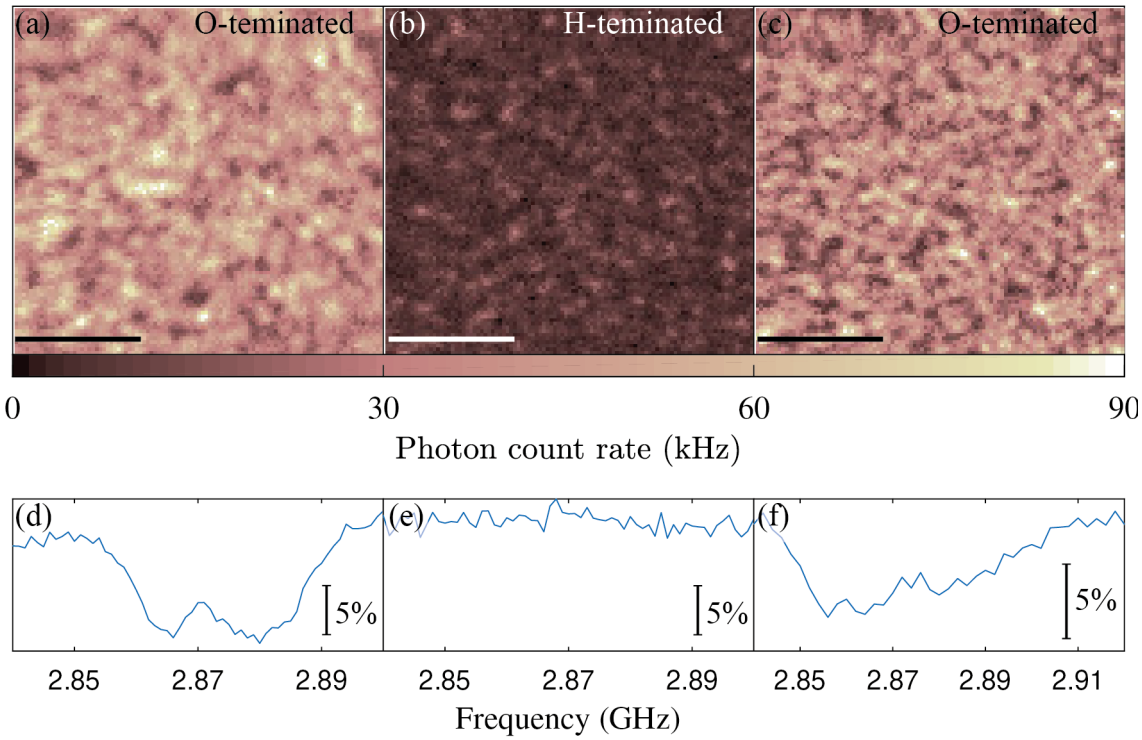

Figure 4.4.: Sequence of confocal images and ESR curves measured of the same diamond sample with different surface terminations. The first is measured on an oxygen terminated diamond surface after an acid clean (a, d), then the diamond is measured after the hydrogen termination with our standard protocol (b, e) and the last time after recovering the oxygen termination by acid cleaning the sample again (c, f). An optical excitation power of 300 μW at a wavelength of 532 nm was used for (a) and (b) and 200 μW (c). The scale bar in all panels equals 5 μm. The ESR curves are normalized with the percentage indicating the change in counts.

sample used was an electronic grade single crystalline diamond obtained from E6, implanted with nitrogen at our standard density used for scanning probe fabrication. The implantation parameters used were 1e11 cm^{-2}N, 12 keV and a 7° implantation angle. After implantation the sample was annealed, resulting in a NV density of $\sim$30 μm^2 at a depth of 17$\pm$6 nm from the diamond surface (Sect. 5.2.3). More information on the implantation and annealing protocol can be found in Chap. 5. The first confocal map was measured after an acid clean (see Chap. 3), then the sample was hydrogen-terminated and measured again. For the last confocal map, the oxygen termination of the diamond was reestablished by performing an acid clean (see Fig. 4.4).

The confocal setup used was a homebuilt optical setup using continuous 532 nm excitation. We refer the reader to Ref. [101] for a description of the setup. To separate the excitation from the collection path, we employ a dichroic mirror with a cut off wavelength of 635 nm (Semrock FF635 Di01) and, therefore, only collect light emitted above 635 nm. As a result of the blue shift of the NV^0 (ZPL centered at 575 nm) spectrum compared to the NV^- (ZPL centered at 637 nm) we collect less photons if the NV is in its neutral charge state and even none for the NV^+, as it does not show fluorescence upon optical excitation [88]. This allows us to readily differentiate between the charge states of the NV center under the surface. Comparing Fig. 4.4(a) and (b), the expected reduction in count rate is clearly visible. In addition to that, we were able to measure an ESR signal on the oxygen terminated sample but not on the hydrogen-terminated one (Fig. 4.4(d) and (e)). From this, we deduce that the hydrogen termination indeed results in a dominant charge state of NV^0 (and possibly NV^+). After the boiling in acid, the fluorescence counts were recovered, and we could again detect an ESR signal from the sample (Fig. 4.4(f)). We attribute the decrease in average fluorescence signal between Fig (a) and (c) to the difference in excitation power and a possible reduction in background fluorescence. A recent publication claims the Hydrogen termination not to be fully reversible by boiling the sample in acids [102]. However, since the authors of [102] implant Nitrogen into a hydrogen-terminated sample, the origin of this observation cannot be fully assessed. Moreover, the authors use a plasma-based termination, which could present a possible source of plasma-induced damage and which may destroy NV centers.

To gain more information about the charge dynamics of the NV centers in the sample, a charge state readout protocol similar to Shields et al. [103] could be implemented to compare the charge stability of the Oxygen terminations before and after the Hydrogen termination. Ideally, this would be implemented on a sample with pillars or marker structures to be able to identify the same NV before and after hydrogen termination. Additionally, we suggest to include saturation curve measurements for NV fluorescence to keep track of the development of the background fluorescence.

4.3.2. Switching of SiV^- emission by H-termination

The neutral SiV center is an auspicious system for quantum applications. It combines the SiV^-'s high fraction of emission into the ZPL ($> 80\%$) with the excellent spin coherence times ($\sim$ 1 ms) typical of NV^- [27, 104]. As SiV^0 is difficult to sta-

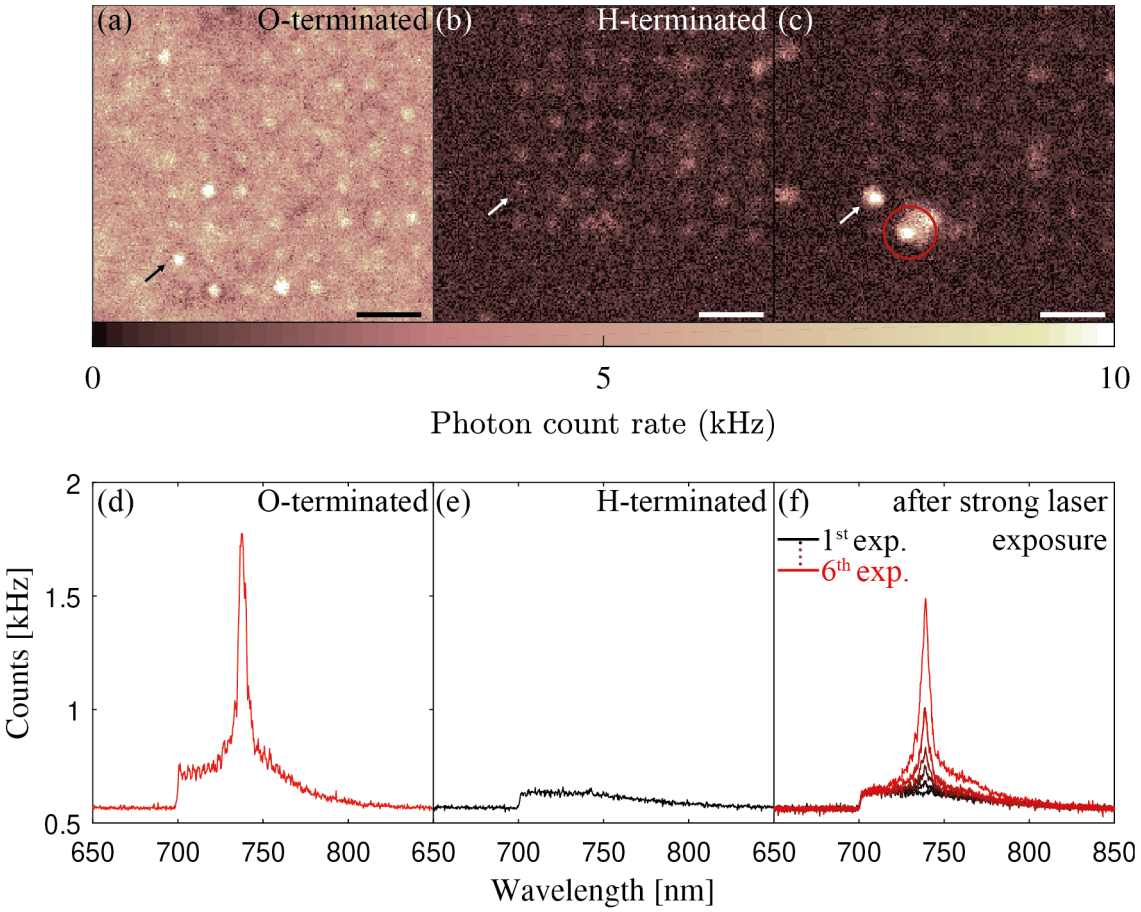

Figure 4.5.: (a),(b), and (c) confocal maps of the same diamond nanopillars containing SiV centers. The diamond surface in the three cases was terminated with oxygen or hydrogen, respectively. An additional bandpass filter was used to limit the background fluorescence. For the excitation 5.5 mW of continuous 532 nm laser light was used. The scale bar in all maps equals 5 μm. The sample was measured before (a) and after (b) hydrogen-termination. An exemplary spectrum of the pillar indicated with an arrow in the corresponding confocal map can be found in (d) and (e). Here only a long-pass filter at 700 nm employed. The red circle in (c) marks a spot on the surface where the laser was parked for $\sim$ 20 minutes. (f) Several spectra were recorded on the same pillar measured before (white arrow), showing the reappearing SiV^- ZPL. Approximately one spectrum per minute was recorded. The first spectrum (black) was taken directly upon laser illumination and the last spectra (red) after $\sim$ 5 min of continuous laser illumination.

bilize, it is not yet well studied. So far, one of the few successful reports in doing so employs Fermi level engineering of the diamond substrate, to stabilize this charge state [48]. This process was a difficult and meticulous task, given the difficulty of the necessary addition of Boron to the diamond during the growth. As the Hydrogen termination also influences the Fermi level, we had the idea to use this termination as a novel and easier method to stabilize the neutral SiV charge state. In the following part, we describe the effect of Hydrogen termination on the SiV charge state in different samples and configurations.

For a first test, we used an electronic grade diamond sample with shallow SiV centers in pillars. To create SiV the sample was implanted with 1e11 cm^{-2} Si at an energy of 25 keV under an implantation angle of 7∘ and annealed for 4h at 400°C followed by a step for 8h at 800°C (see Ref. [105]). According to SRIM simulations we expect SiV centers in a depth of 19±6 nm (Appendix A.2). To increase the collection efficiency of the fluorescence and to mark the SiV positions, we fabricated nanopillars on the diamond. The last step of the fabrication is an acid clean; therefore, the sample was oxygen terminated. For details on the fabrication process and the acid clean, we refer to Chap. 5 and Chap. 3. To characterize the sample, a combination of confocal microscopy and optical spectroscopy was used. An excitation power of 5.5 mW at a wavelength of 532 nm is used to obtain confocal maps. To limit the background fluorescence a bandpass filter was added to the collection path.

A confocal map of the sample after fabrication is shown in Fig. 4.5(a). To confirm the presence of SiV^- color centers, we measure the spectra of the pillars which appear bright in the confocal scan. An example can be found in Fig. 4.5(d), with the corresponding pillar indicated with an arrow in Fig. 4.5(a). After optical characterization, the diamond was hydrogen-terminated and characterized again. The confocal map appears considerably darker (Fig. 4.5(b)). Due to scattering effects, we could identify the position of the pillars. Measuring the same pillar as before, we could no longer detect any SiV^- related fluorescence around 740 nm (Fig. 4.5(e)).

We observed that under strong laser illumination, the SiV fluorescence can be recovered (Fig. 4.5(c) red circle). To investigate the observation more methodically, we exposed a second pillar and simultaneously recorded spectra (Fig. 4.5(f)). We measured a continuously increasing SiV signal. The reappearance of SiV fluorescence was only seen on pillars and did not change after long periods of dark time or disappear when reducing the laser power. Therefore we assume a change in surface termination caused by laser-induced heating. This is supported by the report of photochemical functionalization of hydrogen-terminated diamond using a 254 nm, 4.9 eV laser [106]. An additional argument in favor is that we observe no change when we subject an unstructured area to the same laser irradiation. Due to the high heat conductivity of the diamond, the surface is not heated as strongly in the bulk area compared to the pillar. We assume that the process for this laser-induced surface modification similar to the one we exploit for hydrogen termination. Namely, surface groups dissociate, and the now active sites dissociate gases present in the atmosphere or bind to adsorbents present on the diamond surface. As a result, we expect the resulting surface termination to be a mixture of hydrogen, oxygen, and possibly nitrogen species. Nitrogen is the gas that is primarily present in air and oxygen because it is the second most abundant gas and is also present on the diamond surface inform of an adsorbed water layer. A similar composition

has been observed recently for a diamond exposed to a pulsed laser in air (1064 nm, 3 μJ/pulse, 50 ns) [107].

To summarize, we successfully changed the SiV charge state from negative to presumably neutral and found a technique to switch individual pillars back to SiV^- permanently. To investigate the nature of the altered diamond surface and use its potential, we propose additional steps. First, one should try to find the critical laser power needed to alter the surface termination on bulk diamond. Due to the high thermal conductivity of diamond, it might be necessary to use pulsed laser excitation instead of continuous excitation. The critical laser power could be probed by exposing hydrogen-terminated diamond to an increasing amount of laser power while monitoring the fluorescence signal of incorporated color centers until a change in charge state is detected. The selective removal of the Hydrogen-termination could be used to pattern electric circuits on the diamond surface or tailor the charge state distribution to one's needs. To identify the chemical species, we propose XPS measurements on bulk diamond or, if the termination on bulk diamond proved difficult, one could also measure a field of densely packed nanopillars with XPS. If our proposed mechanism is correct, this technique could be used to pattern the diamond surface locally with different chemical species by changing the gas present during the exposure.

4.3.3. Hydrogen terminated diamond at cryogenic temperatures

After verifying the disappearance of the spectral signature of the SiV center's negative charge state, the logical next step is to measure the SiV^0 spectral signature around 946 nm. For that, we sent the hydrogen-terminated sample characterized and prepared here in Basel (data are shown in Fig. 4.5) to Professor Alex Högele's laboratory in Munich. Their optic setups are optimized to measure fluorescence in the infrared, where the neutral SiV emits. Unfortunately, the group could not detect any SiV^0 related fluorescence-more on the topic later in this section (Fig. 4.8). However, their studies revealed an interesting observation presented in Fig. 4.6. During their measurements, they took on every position a full spectra at room temperature and 4K. In Fig. 4.6(a) and (b) a map of the integration of the spectral range 735-740 nm can be seen for both temperatures. Their map shows the same area already characterized in Basel (Fig. 4.5). The two bright spots in (b) correspond to the laser-illuminated pillars shown in Fig. 4.5(c). The spectra for the pillar in the red circle can be seen in (c) for 4 K, and (d) for 295 K. At both temperatures, a clear SiV^- signature is visible as expected. For the 4 K map, additional bright spots are appearing in close agreement to the positions where we measured pillars containing SiV^- centers under oxygen termination. After heating the sample to room temperature, the spots disappear again. The spectra measured on the pillars identifies the appearing fluorescence as SiV^-. However, compared to the laser annealed pillar, the appearing peak low indicating a relaxation but not complete elimination of the hydrogen-induced band-bending. This observation could be explained by the holes freezing out under cryogenic conditions. Nebel et al. [108] found in their work sample dependent critical temperatures, below which the hole sheet density was reduced. They attribute these sample-specific critical temperatures to differences in the diamond surface, such as imperfections in the hydrogen termination, surface

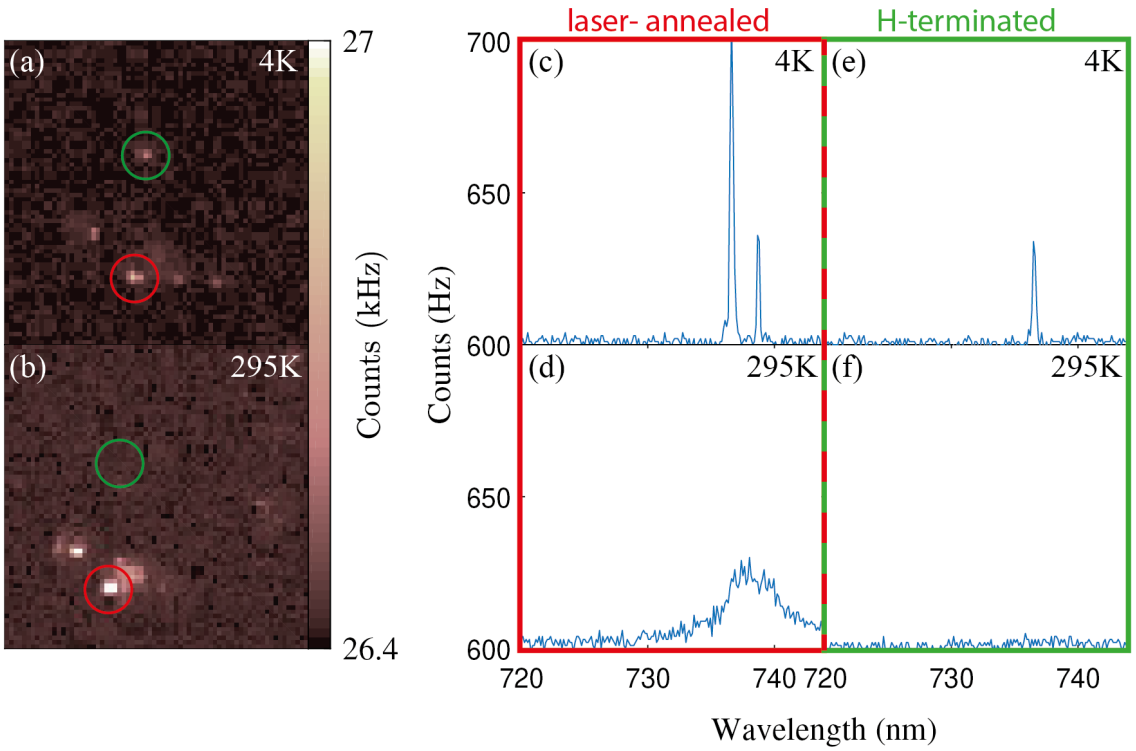

Figure 4.6.: Hyperspectral mapping of SiV fluorescence from H-terminated diamond: on each point of the map, a full optical emission spectrum was recorded, under 532 nm excitation. (a) and (b) show the integrated counts in the spectral range from 735 nm to 740 nm as a function of position. The spectra were recorded at 4 K (a),(c)and (e) with an excitation power of 100 μW or at room temperature (b),(d) and (f) with an excitation of 2 mW. In (c) and (d) the spectrum of the laser laser funktionalized pillar (c. f. Fig. 4.5(c)) circled in red is shown at 4 K (c) and 295 K (d). In (e) and (f) the spectrum of an untreated, hydrogen terminated pillar is shown at 4 K (e) and 295 K (f).

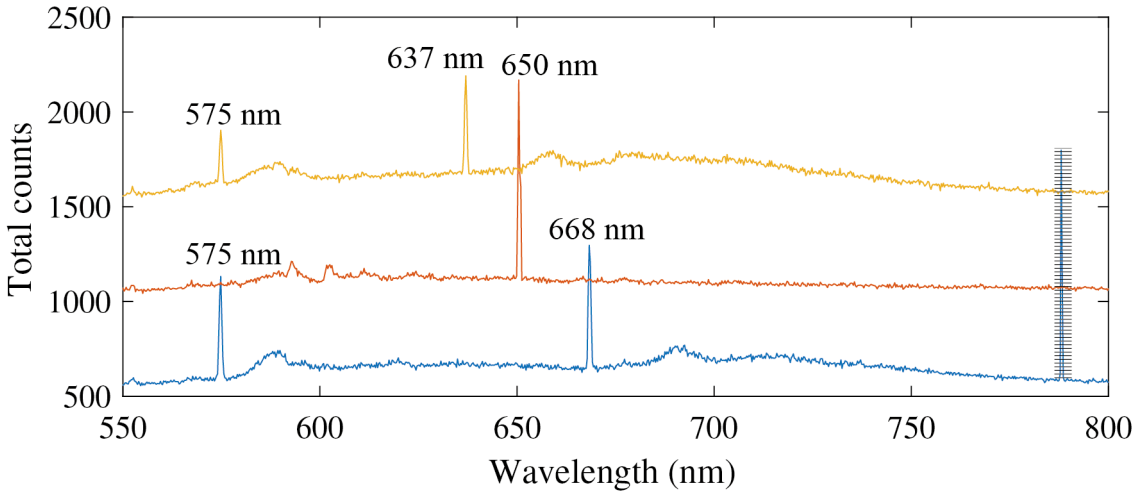

Figure 4.7.: Specta of 3 different NV in hydrogen terminated diamond measured with a 300 μW, 515 nm excitation. The temperature during the measurement was 6 K. The lined area indicated a cosmic ray.

roughness, and negatively ionized adsorbents generating Coulombic disorder at the diamond surface. These irregularities introduce differences in the up bending of the valence and conduction bands, and as a result, generate electronic traps and destroy the long-range order. These differences in local band bending together with local differences in doping could also explain the spread in charge states observed.

To investigate this apparent reduction in band-bending further, we examined a single crystalline diamond sample implanted with NV centers. The implantation parameters were ^{15}N, 12 keV, 1e^{11} ions/cm^2 and 7° resulting in an NV depth of 17±6 nm. After the implantation the diamond was annealed with or standard annealing protocol [18] and hydrogen-terminated (Sect. 4.3). The measurement was performed at a temperature of 5 K using an excitation wavelength of 515 nm. Measuring the spectra we found the expected NV^0 ZPL at a wavelength of 575 nm, and one other peak at varying wavelengths. We observed these unexpected peaks at wavelengths from the ZFL of the NV$^-$ up to 700 nm. Approximately every third NV center measured had this shifted peak. It is unclear if these peaks are associated with the NV$^-$. Our first idea was an electric field induced ZFL shift. However, this seems rather unlikely considering the electric field strength of 410±5 kV/cm reported by Broadway et al. [109], for the Hydrogen terminated diamond surface. To investigate this further, the first step is to verify if the appearing peak is indeed N$^-$ related. We propose either to try to stabilize the charge state by green laser illumination and measure ESRor to conduct correlation measurements between the ZPL of the neutral and negative NV center. Interestingly spectra measured on hydrogen-terminated diamond at 7 K with shallow SiV centers also had an unknown peak shifted from to higher frequencies of ZPL of SiV^0. Additional to the measurements in Munich, we sent a different sample to Princeton to Professor de Leons group, as they are most experienced in detecting SiV^0 fluorescence. The sample had nanopillars fabricated here in Basel containing single SiV at a depth of 19±6 nm ([Si], 25 keV, 3e10^{11} ions/cm^2, 7°).They did not find any fluorescence near 946nm, the ZPL of SiV^0, but found a signature at 991 nm in several pillars (Fig. 4.8). The

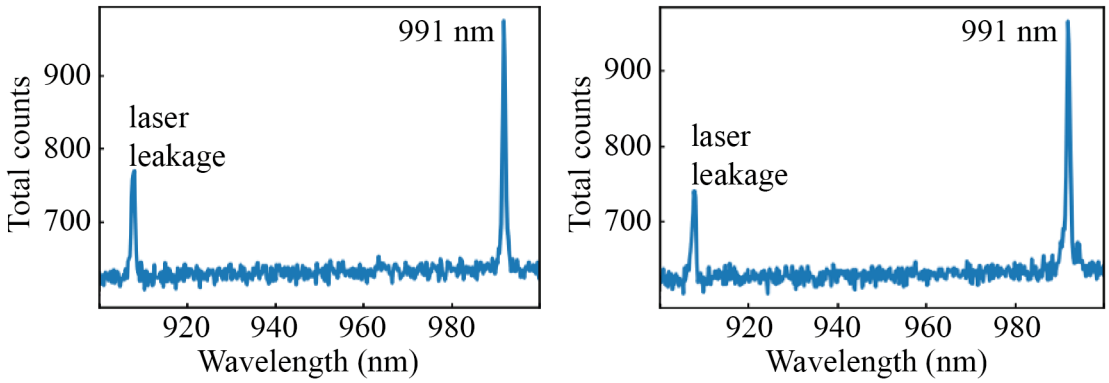

Figure 4.8.: Both panels show spectra measured with a 905 nm excitation, at a temperature of 7 K. The sample measured was a hydrogen-terminated diamond with implanted SiV centers and structured with nanopillars. The measurements were performed in Prof. de Leon's research group in Princeton.

observed peak is not a Raman line as it did not shift when changing the laser excitation. The origin of the peak is unclear further experiments are being conducted to see if the peak correlates with the SiV^- charge state. This opens up the question if the observed peaks could be the SiV^0 and NV^- peaks, as they have a similar electronic structure, a similar reaction to external influences seem reasonable.

To summarize, the Hydrogen induced band-bending appears to be less pronounced in cryogenic temperatures and might induce a shift in the ZPL of the N^- and SiV^0. The reduction in efficiency observed is consistent with the reduced hole sheet density reported by Nebel et al. [108]. The observed shifted peaks need to be further investigated, first to confirm if they are NV respectively SiV related at all and second to find a suitable explanation for the shift.

4.3.4. Clarification of energy levels

As there are some uncertainties in the community concerning the localization of the charge state transition energy level of the SiV center, we prepare a diamond with both color centers, the NV, and the SiV, present. To ensure approximately the same depth localization we implant a nitrogen-enriched diamond with 1e11 cm^{-2} Si at an energy of 80 keV and anneal the sample for 4 h at 400° C, followed by an annealing step for 8 h at 800° C (see Ref. [105]). SRIM simulation predicts SiVs to be located at a depth of ∼55 nm. We assume that the NVs are created by recombination of the implantation induced vacancies with the nitrogen already present in the diamond lattice. As a result, the NVs are expected to be located more shallow than the SiV centers. The spread of the implanted ions and induced vacancies is shown in A.2.

Examining the sample after color center creation, we found clear evidence of NV^- and SiV^- center under oxygen termination (Fig. 4.9(b)). This is unexpected considering the predicted position of the charge conversion level of the SiV^- to the SiV^{2-} center. From it, we would expect SiV^- to appear only when the NV is in its neutral charge state Fig. 4.9(a). As an orientation help a band diagram indicating the Fermi level ranges, where each charge state is stable and the expected Fermi level for both hydrogen and oxygen-terminated diamond, at the position of the

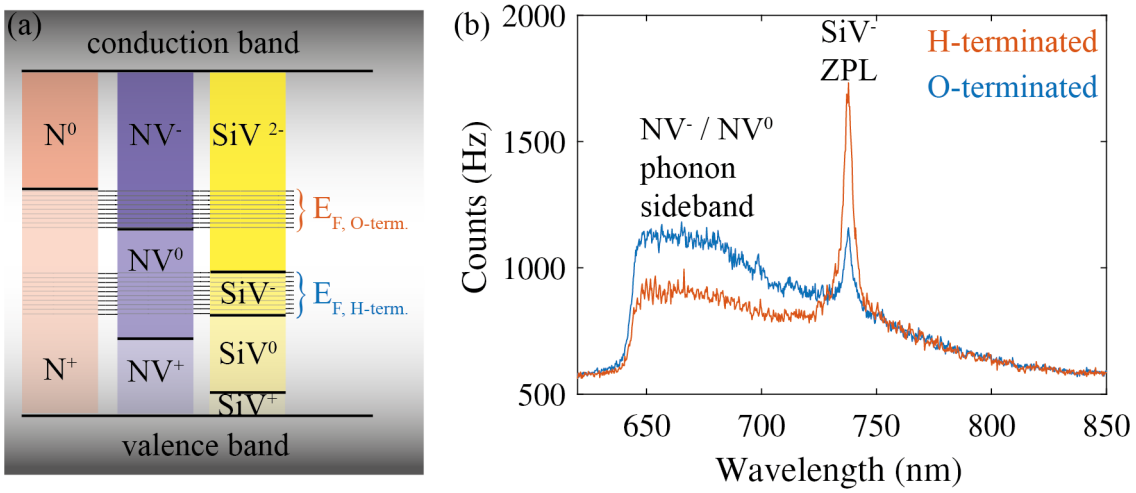

Figure 4.9.: (a) Simplified version of Fig. 4.1 with the assumed location of the Fermi level at the position of the color centers for the O-terminated ($E_{F,\,O\text{-term}}$ and the H-terminated ($E_{F,\,H\text{-term}}$) diamond.(b) Spectra measured with 1 mW, 532 nm excitation on a sample containing NVs and SiV under different surface termination. The blue trace is measured directly after an acid clean and the orange after hydrogen termination. The sharp edge around 630 nm is due to a dichroic in the beam path.

color centers, can be found in Fig. 4.9(a). After hydrogen termination, we found an increased SiV^- peak and a reduced NV^- phonon sideband (Fig. 4.9). We interpret the increase in SiV^- fluorescence as a sign that several centers converted from SiV^{2-} to SiV^- [110] and the reduction of the phonon sideband as a consequence of the conversion of NV^- to NV^0. This puts the $SiV^{-/0}$ charge state conversion level lover than the $NV^{-/0}$. With this explanation and the previously introduced theory of the charge state being influenced by the distance to the next donor, our observations are in agreement with reported ab initio calculations [92, 110]. We attribute the differences in the spectrum found, compared to the previous spectra shown (Fig. 4.4 and Fig. 4.5) to the increased depth of the implantation and the unknown nitrogen concentration of the sample. The band bending effect of the hydrogen termination does not reach as far into the diamond for higher nitrogen concentrations [111].

4.4. Water layer on diamond surface

In this section, we investigate the importance of the water layer adsorbed on the diamond surface for the band bending observed on H-terminated diamond. Our motivation to understand the role of adsorbed water in the band bending mechanism is two-fold. For one, there are reports about the surface conductivity disappearing when heating a diamond sample in vacuum [112]. The disappearing surface conductivity implies a reduction of band bending in the absence of the water layer on the diamond surface. This could mean that the negative charge state of the NV is stable if one can protect the diamond surface from water. This could enable us to study the NV spin and optical properties under H-termination.

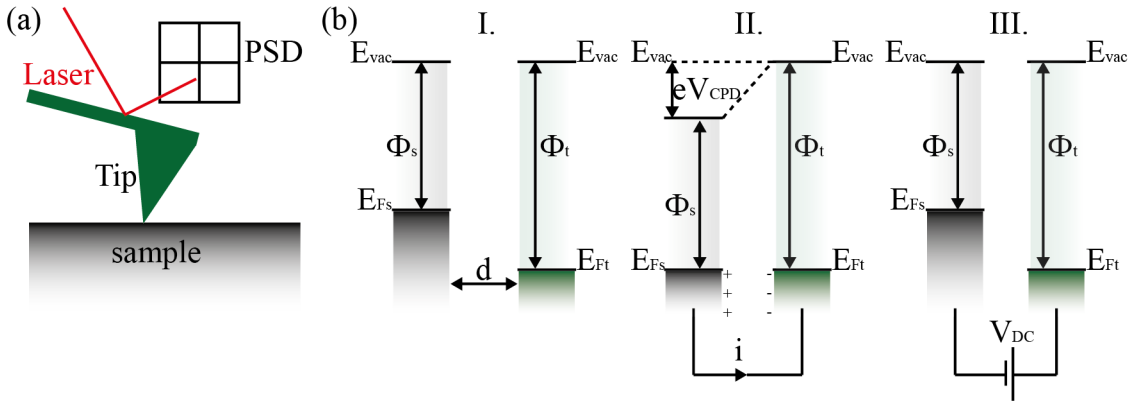

Figure 4.10.: (a) Drawing of a position-sensitive detector measuring cantilever deflection by detecting the relative position change of a laser reflected from the cantilever backside. (b) Illustration of the working principle of Kelvin Probe Force Microscopy. Vacuum level (E_{vac}) , work functions (Φ) and Fermi levels ($\mathrm{E_F}$) of the sample and tip for different cases: I. tip and sample are at a distance d with no electric contact II. tip and sample are in electric contact though the leads and III. an external bias V_{DC} is applied to compensate the contact potential difference. Reproduced from [113].

4.4.1. KPFM study in water-free environment

To better understand the diamond surface and the overall role of the surface adsorbed water layer, we performed Kelvin Probe Force Microscopy in a glove box filled with inert gas. These measurements were taken in collaboration with Ernst Mayer and his research group at the University of Basel.

4.4.1.1. Introduction to Kelvin Probe Force Microscopy

Kelvin Probe Force Microscopy (KPFM) is an Atomic force microscopy (AFM) based method for detecting the Contact Potential Difference (CPD), the difference in work functions of the sample (Φ_s) and an AFM tip (Φ_t). During the measurement, both sample topography and CPD are recorded simultaneously. The cantilever is excited mechanically using a frequency close to its first resonance mode. When the AFM tip is approached to the sample surface, tip-surface forces act on the tip, and the cantilever resonance frequency shifts slightly. This leads to a change in vibration amplitude and cantilever deflection, respectively. A position-sensitive detector (PSD) is used to detect the cantilever deflection through a laser reflected from the cantilever backside (Fig. 4.10(a)). The change in amplitude is used as a feedback signal to keep the tip-to-sample distance constant and record the sample topography. To understand the principle of CPD measurements, one needs to consider the material properties of the sample and tip (Fig. 4.10(b)). Every material has its work function, the minimum energy needed to move an electron at the Fermi level inside the material surface to the Vacuum level (E_{V}), which is defined as the energy of a free stationary electron in perfect vacuum outside of the material. When two materials are separated by a big enough distance such that no electrons can tunnel between the two, the vacuum level is aligned, but the work function and, therefore,

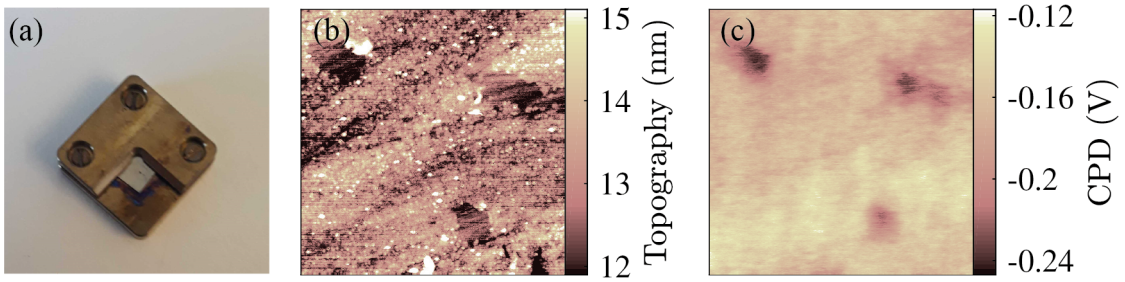

Figure 4.11.: (a) Picture of the holder designed to optimize the electric contact between the KPFM holder and our sample. Topography (b) and the corresponding CPD (c) of a 2x2μm diamond surface with a layer of unknown surface adsorbents.

the Fermi level can differ. If tip and sample are brought into electrical contact, a current flows, and at the equilibrium state, the Fermi level is equalized. The transfer of electron leads to a build-up of surface charges and as a consequence an attractive force between the surfaces. These forces can be nullified by applying a potential between sample and tip to counteract the CPD. In amplitude-modulated KPFM a combination of V_{AC} and V_{DC} potential is applied with the AC frequency being tuned to the second resonance of the cantilever. This enables the simultaneous recording of CPD and topography. Further details on the KPFM method can be found in references [113] and [114].

4.4.1.2. KPFM on diamond

To study the influence and nature of the wetting layer and the surface adsorbents, we performed KPFM measurements on hydrogen and oxygen terminated diamonds. Measurements were performed in a glove box filled with dry nitrogen to ensure an inert and humidity-free atmosphere (O_2 and H_2O level below 0.1 ppm). The samples are measured in situ, directly after transferring them into the glove box and after annealing for 2 hours at a temperature of 400°C. A FlexAFM with a C3000 controller (Nanosurf) was used to measure topography and a UHFLI lock-in amplifier (Zrich instruments) to control the KPFM feedback. All measurements were performed with Pt/Ir5-coated PPP-EFM cantilever (Nanosensors, f_1=75±40 kHz, f_2∼500 kHz). Further detail of the measurement setup can be found in reference [115].

As pure diamond is an insulator, it was not evident in the beginning if the conductivity of our slightly doped material is high enough for reliable KPFM measurements. We optimize electrical contact with the sample by using a specially made holder clamping the sample from all sides (Fig. 4.11 (a)). As a first test, we chose a dirty area on one sample. As can be seen, comparing Fig. 4.11(b), and (c), we can see a clear difference in CPD in three places, and these align perfectly with what appears to be holes in the layer of adsorbents. As we see a difference in CPD between the areas, we assumed the remaining conductivity to be high enough.

4.4.1.3. H-term vs. O-term diamond

To investigate the water layer on H-terminated diamond more closely, we conducted a series of measurements. First, we measured the sample directly after loading it into

the glove box. To remove water from the sample surface, we then heated the sample to 400°C for 2 hours, let the sample cool down, and measured it again. With this heating, we hoped to desorb the water layer on the diamond surface, including the adsorbents involved in the charge transfer doping process. To ensure reproducibility, we took the sample out of the glove box, left it in atmosphere for 30 minutes, then reintroduced it to the glove box and measured it again. After that, we repeated the annealing step and measured the sample a last time. We conducted this experiment for two samples, one hydrogen, and one oxygen terminated diamond for reference. For two reasons, we used single-crystalline diamonds, for all the experiments shown. First, the surface roughness of single-crystal diamond is a lot smaller than for polycrystalline diamond, and second, the grain boundaries in polycrystalline diamond could interfere with the KPFM measurement by locally changing the Fermi level due to defects or dopants. The hydrogen termination was prepared by the previously introduced protocol (Sect. 4.3) and the oxygen termination by acid cleaning the diamond (Sect. 3.2.1).

For each measurement, we collected the topography and CPD of a 2x2 μm area. To visualize the CPD values of all the measurements, we plotted the histogram of the CPD maps (Fig. 4.12). An example of a set of measurements (topography and CPD) can be seen in Fig. 4.11(b) and(c). As we performed no measurement using the tips on a known material, we can not calibrate its work function, and therefore we can only compare relative values. The difference between the CPD before and after annealing the hydrogen-terminated surface is 0.093 V for the first and 0.087 V for the second measurement set Fig. 4.12(a). The unexpected shift between the first and third measurement could be due to a change of the tip, either geometry or an adsorbed contamination. The oxygen and hydrogen-terminated samples cannot be compared directly, as a different tip was used, which could result in a further offset. For the oxygen terminated sample, the annealing induced shift is with 0.20 V and 0.22 V twice as large as for the hydrogen-terminated sample. The shift towards lower CPD with annealing the sample is consistent with what was previously measured for nanodiamonds for both terminations [115]. In these measurements, the authors found a more significant shift for both terminations with 0.5 V for the hydrogen-terminated and 0.35 V for the oxygen terminated nanodiamonds. The authors of [115] explain the shifts by a desorbing surface-bound water layer; since it is expected that a porous powder (such as a nanodiamond sample) contains more hydrogen than a crystalline surface, we do not see their results as contradicting our measurements. Following the argumentation in [115], we assume a thinner water layer on the hydrogen-terminated diamond surface compared to the oxygen terminated surface, which is in agreement with [116]. As we do not see a substantial change in CPD for the hydrogen-terminated diamond, we assume the two-dimensional hole gas still to be present even after annealing. A possible explanation for this could be that the temperature is not high enough or that we would need to heat for a more extended period to allow for full removal of the water layer from the system.

For future measurements, we suggest to pattern gold markers on every surface to be able to calibrate the work function of the measurement tip. In such a measurement, one could also determine the Fermi level on oxygen terminated diamond prepared with different protocols. With these additions, KPFM would be a powerful

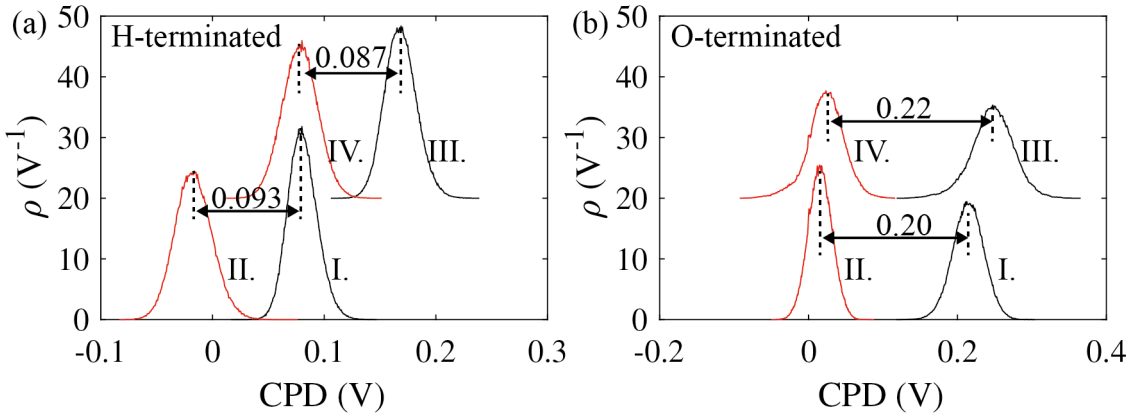

Figure 4.12.: Histogram of KPFM values of a 2x2μm scan of a hydrogen (a) and oxygen (b) terminated diamond surface. The sample was measured after introduction to the glove box (I.), then after annealing inside the glove box for 2 hours to a temperature of 400°C (II.), then the sample was taken out of the glove box for 30 min reintroduced remeasured (III.) and annealed once again (IV.)

tool to investigate the diamond surface and the cause of charge state instabilities. However, the technique can only live to its full potential when a possibility to characterize the work function of the tip is present.

4.4.2. Alumina oxide as protection layer

The deposition of aluminum oxide (Al_2O_3) is an often-used technique in the field of diamond electronics to stabilize the surface conductivity. Al_2O_3 protected devices based on hydrogen-terminated diamond surface conductivity have been reported to perform over a wide range of temperatures (10K-700K) and up to high voltages (~1 kV) [117]. This could be of interest for the protection of the neutral charge state of the SiV. For oxygen terminated diamond capped with aluminum oxide, the absence of surface conductivity has been reported [118]. This led us to the idea to test Al_2O_3 as a protection layer for NV^- based measurements. The deposition technique used is Atomic layer deposition (ALD). Two precursors are used in an alternating fashion to grow the oxide layer by layer. In the case of Al_2O_3, the precursors used are trimethylaluminum (TMA) and water. ALD has the advantage to coverer three-dimensional structures evenly in a conformal way and would, therefore, ultimately be compatible with cantilever fabrication.

To test the interaction of Al_2O_3 with incorporated color centers and measure its optical properties, we deposit 1 nm of Al_2O_3 on the surface of an implanted single crystalline diamond. Our standard NV implantation is used (1e11 cm^{-2} N, 12 keV, 7° implantation angle) followed by an anneal (see Chap. 5) to mobilize the vacancies and create NVs. The diamond is treated with an acid clean and examined by confocal microscopy, previous to the ALD deposition. After the deposition, we investigate the surface by confocal microscopy again and see a clear increase in fluorescence (see Fig. 4.13). We assume the fluorescence to be caused by the additional Al_2O_3 layer, upon green laser exposure, it appeared to bleach. The darker square in Fig. 4.13(b) was exposed to green laser light (140 μW) for 5 minutes.

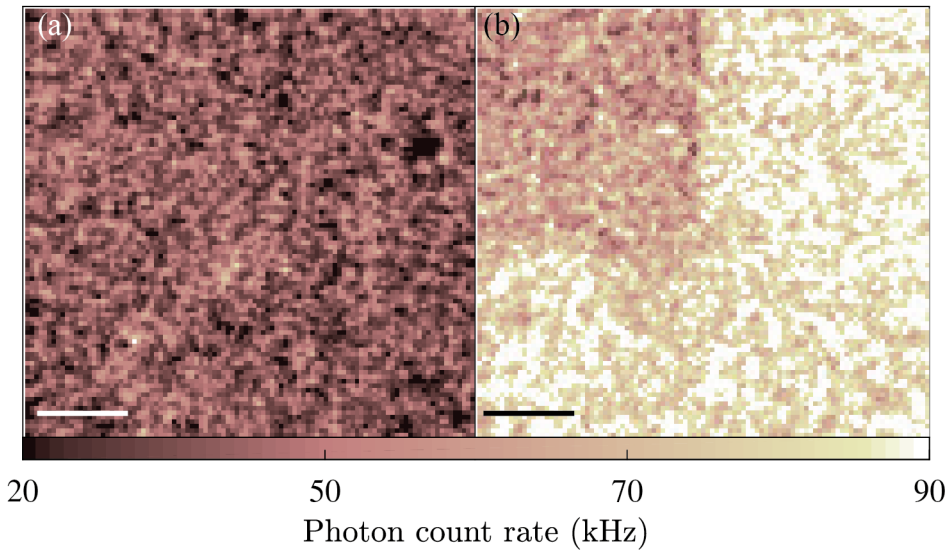

Figure 4.13.: Confocal image of a diamond sample implanted with NVs, using continuous 532 nm excitation at a power of 140 μW. The sample is measured before (a) and after (b) deposition of a 1 nm thick aluminum oxide layer. The darker square in (b) has been exposed to 5 min of continuous scanning laser illumination. The scale bar is 5 μm in both panels.

To summarize, we were able to deposit an even film of Al_2O_3 on the diamond surface, but already 1 nm of Al_2O_3 leads to significant background fluorescence, for the exciton wavelength and power typically used to measure NVs. Further experiments with longer bleaching times are necessary to determine if the fluorescence can be reduced enough to enable ODMR and other spin manipulation experiments. We did not examine the Al_2O_3 fluorescence spectrum in the wavelength range relevant for SiV^0.

4.5. Summary and Outlook

We started this chapter with an introduction to the model of energy bands and band-bending and used them to explain the charge transfer doping responsible for the surface conductivity observed on hydrogen-terminated diamond. Further, we listed the reported charge transition states for the NV and SiV center and put them into context with the Fermi level expected for different surface terminations and diamond substrates.

We successfully established a hydrogen termination protocol based on thermal annealing under hydrogen atmosphere at ambient pressure. We verified the success and reversibility of the process by XPS measurements and the comparison of the emission of shallow implanted nitrogen vacancies. From the reduction in fluorescence observed after H-termination, we conclude that the most favorable NV charge states are NV^0 and NV^+ rather than the NV^-. This indicates a Fermi level below $E_V + 1.7\,eV$.

In the next step, we hydrogen-terminated a sample containing shallow silicon vacancies in fabricated nanopillars and removed the termination selectively from two

pillars by laser illumination. We verify the disappearance and reappearance of the SiV^- emission by measuring spectra on nanopillars that were previously characterized under oxygen termination. We find no sign of the 740 nm SiV^- ZPL on the hydrogen-terminated pillars and a clear SiV^- ZPL signal on the laser-illuminated pillars. Compared to the oxygen termination, the signal measured on the laser-illuminated pillar was weaker, either because of an incomplete surface termination or possibly a different termination combining nitrogen and oxygen species.

After successful eliminating the SiV^- fluorescence at room temperature spectra of the H-terminated and laser-treated pillars were measured at cryogenic temperatures, and the resulting spectra were compared to the RT spectra. Interestingly, it was found that the hydrogen-termination appears to have a weaker effect on the charge state of color centers at low temperature, we suggest the freezing out of holes as a plausible explanation. To investigate this further, Hall effect conductivity measurements, as conducted in Ref. [108] could help to complete the picture and verify the suggested reduction in hole sheet density. Ideally, for such a test, both Hall effect conductivity and fluorescence spectroscopy measurements should be conducted on the same sample for a range of temperatures.

Next, we clarified the positioning of the SiV charge conversion levels relative to the positioning of the $NV^{-/0}$ charge conversion level, by implanting a nitrogen-enriched diamond sample with Si atoms. We found our results in good agreement with the calculation by Adam Gali et al. [89], placing the $SiV^{-/0}$ and $SiV^{2-/-}$ charge conversion levels below the $NV^{-/0}$ charge conversion level (c.f. Fig. 4.1).

To investigate the influence of water adsorbed on the H-terminated diamond surface on the band bending, we conducted a series of KPFM measurements under inert gas comparing the oxygen terminated diamond surface with the hydrogen-terminated surface in the presence and absence of the surface water layer. We found a reproducible shift in CPD between the surfaces with and without the water layer. The detected shift is consistent with previous reports on nanodiamonds and suggests a thinner water layer on the hydrogen-terminated diamond compared with the oxygen terminated diamond. So far, we could not detect an indication of the band bending being reversed by the annealing. We assume that higher temperatures are necessary to desorb not only the water layer but also the charged adsorbents stabilizing the 2D hole gas. The measurement on a hydrogen-terminated diamond surface without adsorbents could bring some interesting additional insights. The decreased efficiency of the band bending could open up an opportunity to study the NV^- under hydrogen termination. However, also the NV^0 is so far not well studied and could offer some insights relevant to the negatively charged NV when it comes to charge state dynamics.

For the neutral charge state of the SiV, an important next step is to verify the charge conversion from SiV^- to its neutral charge state by measuring the SiV^0 spectral signature directly. Open questions concerning the quantum efficiency of the SiV^0 in general and under these specific circumstances remain. If the quantum efficiency is further reduced due to interactions of the SiV^0 with the hydrogen-termination or the adsorbed water layer, direct observation of the fluorescence could prove difficult. The correlation of the Fermi level with the presence of an adsorbed water layer and the sample temperature could constitute another problem. One possible solution could be the capping of the diamond surface with an alumina

oxide layer. We performed some preliminary experiments on a diamond implanted with shallow NV centers. We find a strong fluorescence after the deposition of only 1 nm, but fluorescence could be bleached up to some extent by laser illumination. An essential next step is to analyze the fluorescence spectrum of aluminum oxide in the range relevant for the SiV^0 emission. Alumina has been shown to stabilize the surface conductivity of the diamond and protect the diamond surface for diamond electronic devices for temperature ranges from 10 K to 700 K.

The establishment of a hydrogen termination protocol opens up various possibilities for other termination protocols. Some examples of termination protocols using hydrogen termination as starting point are Nitrogen termination [87] or Fluorine termination [86]. Additional to these protocols, we suggest a possibly novel technique to terminate the diamond surface locally using laser illumination, with an unknown variety of different species. Patterning the diamond surface with different terminations could be interesting for various reasons and research fields. For color center-based research, it could present an ideal platform to study the influence of these terminations on the color center charge state and its optical and spin properties in a comparable and reproductive way. In biology, diamond films patterned with different hydrophilic areas are studied for guided cell attachment and growth [119]. For the field of diamond electronics, this technique could be used to pattern electric circuits. Depending on the needed resolution, the suggested method could be an easy and comparably cheap alternative to the normally used e-beam lithography combined with plasma-induced surface termination.

Summarizing, the hydrogen-terminated diamond surface is a unique system offering lots of different open phenomena to study and to use in prospective applications.

5. Single crystalline diamond pyramids and their potential for sensing applications

After discussing different surface termination protocols and their influence on shallow color centers, we present, in this chapter, a new approach avoiding the plasma-induced damage of our usual fabrication processes. In the first part, we introduce the fabrication of all diamond nanopyramids formed by the overgrowth of nanopillars. We describe the nanopillar fabrication, the overgrowth process, and the incorporation of color centers. In the second part, we present our findings studying the photonic properties of overgrown structures, using confocal microscopy and numerical simulations. We further discuss substrate quality, smoothness of the surface, and sharpness of the tip, of the overgrown structures.

5.1. Motivation

The advantages of diamond as host also come with some drawbacks, as discussed in Chap. 2. The hardness and chemical inertness of single crystalline diamond (SCD) require harsh plasma etching procedures in the nanofabrication process, which leaves the SCD surface damaged and results in non-ideal coherence properties of the sensing spins [19]. Besides the optimization possibilities of the diamond surface, also the geometry of single color center SCD scanning probes have potential for optimization. The scanning probes usually assume the approximate shape of a truncated cone, with a relatively blunt, circular end-facet of $\sim 200\,\mathrm{nm}$ diameter. While this shape has proven beneficial for the tip's photonic properties [50], it is far from ideal for AFM performance for two reasons: First, the bluntness of these tips prevents high-resolution AFM imaging during single spin magnetometry, which is relevant when imaging samples with non-planar geometries. Second, pillars with circular end-facets require excellent angular alignment to be in full contact with the sample, which typically results in increased spin-to-sample distances leading to a loss in spatial resolution and sensitivity per source strength [8].

In this chapter, we present a new approach to realizing all-diamond tips for scanning-probe, nanoscale quantum sensing, which has the potential to address both issues of the truncated cone-shaped scanning probes highlighted above. These experiments have been conducted in collaboration with our colleagues at the Frauenhofer Institut für angewandte Festkörperphysik IAF in Freiburg and is published in Ref.[120]. For this, we combine aspects of "top-down" (etching) and "bottom-up" (overgrowth) fabrication to yield nanometre-sharp, pyramidal diamond tips, as illustrated in Fig 5.1(a). Specifically, we overgrow SCD nanopillars, fabricated via

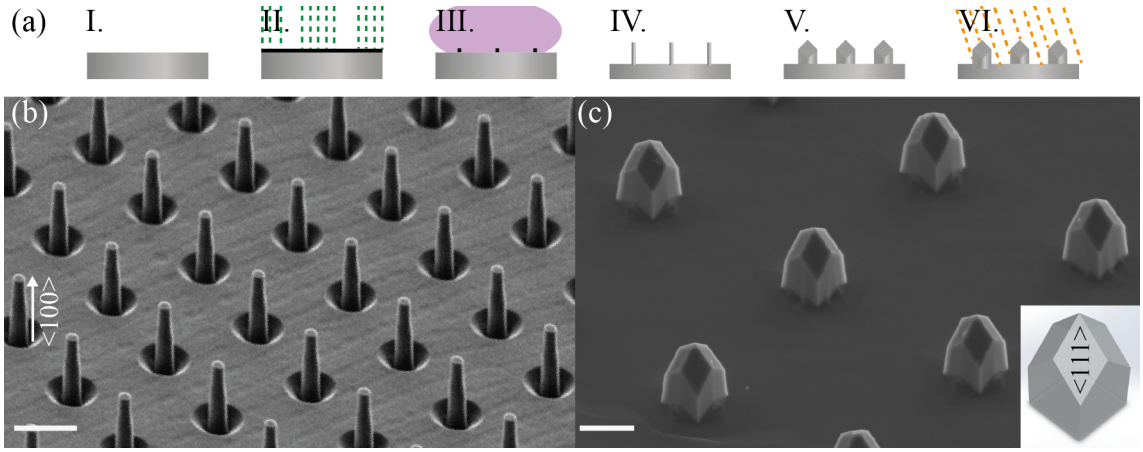

Figure 5.1.: (a) Schematic of the nanofabrication and overgrowth process pursued in this work. Base material, as well as grown pyramids, are single crystal diamond (SCD) I: Cleaning and surface preparation; II: Definition of etch-masks by e-beam lithography; III: Etching of diamond nanopillars using oxygen plasma; IV: Removal of etch residues and HSQ mask; V: Overgrowth of diamond material to form pyramids; VI: Color center incorporation by ^{14}N-ion implantation and subsequent annealing. (b) Scanning electron microscopy (SEM) image of representative diamond nanopillars after nanofabrication (step II) and (b) after diamond overgrowth (step III). The scale bar $\widehat{=}$ 1 μm in both cases. Both SEM images were recorded at a 45° tilt angle from the sample normal. Inset: Schematic of the resulting pyramids with a $\langle 111 \rangle$ crystal facet indicated.

reactive ion etching, with high purity SCD by chemical vapor deposition (CVD). The highly anisotropic growth of SCD transforms these pillars into single-crystalline diamond pyramids [121, 122]. The pyramids show high collection efficiencies for color center photoluminescence, which, together with their sharp apex radius of curvature of $\lesssim$ 20 nm, makes them perfectly amenable for future applications as scanning probes.

5.2. Fabrication of single-crystalline diamond pyramids

The fabrication of diamond pyramids can be divided into three main phases: The fabrication of the nanopillar template, the template overgrowth, and the incorporation of color centers into the diamond pyramids. A schematic of the process can be found in Fig. 5.1(a).

5.2.1. Pillar template fabrication

Fabrication processes evolve as knowledge grows and needs change. We choose to report the most recent protocol for diamond nanopillar fabrication, as we expect it to be most valuable to the reader. A detailed description of the former process used to fabricate the actual pillar template can be found in [18] and [123].

Plasma	ICP Power (W)	RF power/bias (W/V)	Flux (sccm)	Pressure (Pa)	Etch rate (nm/min)
$ArCl_2$	400	100/-220	Ar 25 Cl_2 40	1	60
O_2	700	50/-110	60	1.3	100

Table 5.1.: Table with plasma parameter used for nanofabrication of diamond pillar.

The base material used in our process was commercially available, ⟨100⟩-oriented electronic grade single crystalline diamond (SCD) (Element6, Electronic grade $[N]^S < 5$ ppb, [B]<1 ppb)[124]. First, the SCD substrate was boiled in a $1:1:1$ mixture of nitric, sulfuric, and perchloric acids previously referred to as "tri-acid clean" (Sect. 3.2.1). To remove possible acid residues, we performed a "solvent clean" (the sample was rinsed with DI water, acetone, IPA, and blow-dried with nitrogen gas) after the tri-acid clean. This first step aimed to create a reproducible starting point with a clean surface and well-defined surface chemistry. To get rid of a possible water layer or solvent residues, we prebaked the sample on a hotplate at a temperature of 120 °C for 2 minutes. Then the sample was spin-coated with FOX-16, an HSQ based negative e-beam resist distributed by Dow Corning. The spin-coating was followed by another baking (90 °C for 2 minutes) and another spin-coating step with Electra 92 (bought from AllRESIST), a conductive coating used to mitigate charging effects during e-beam lithography. To finish the resist preparation, we baked the sample one last time at a temperature 90 °C for 2 minutes. The expected FOX film thickness was 600 nm. Electron beam lithography with an electron energy of 30 keV, and a dose of 1500-2000 μ As / cm^2 was used to write a pattern of 200 nm diameter circles. After exposure, the sample was developed in 25 wt.% TMAH for 25 s. A Sentech SI 500 ICP-RIE apparatus was used to transfer the mask into the diamond by plasma etching. A one minute Argon-Chlorine ($ArCl_2$) plasma (see Tab. 5.1) ensured a clean surface. Subsequently, a longer oxygen plasma step (see Tab. 5.1) was used, to etch $\sim 2\,\mu$m long pillars. In the next step, the HSQ mask was removed by a buffered oxide etch (10:10:1 deionized water, ammonium fluoride, 40% HF), and the sample was cleaned in a final acid clean followed by a solvent clean.

5.2.2. Pillar overgrowth

The nanopillars (Fig. 5.1(b)) were then overgrown at Frauenhofer Institut für angewandte Festkörperphysik IAF in Freiburg. A total of $\sim$ 1 μm of SCD ([N]<2 ppb [125]) was grown on top of the patterned substrate by microwave plasma-assisted chemical vapor deposition. For more details on the crystal quality, we refer to Ref. [125]. Key growth parametersa substrate temperature of 750° C, microwave power of 2.1 kW, a chamber pressure of 200 mbar and a gas mixture of $3:1$ [CH4]:[O2] with a methane concentration of 3 % in the process gas. The flow rates for H_2 and methane were 291 sccm and 9 sccm respectively. The resulting diamond growth velocity along 100 was determined to be $V_{\{100\}} \sim 0.4\,\mu$/h at which the diamond was overgrown for 75 minutes. As evidenced by the representative scanning electron microscopy (SEM) image shown in Fig. 5.1(c), the pillar overgrowth led

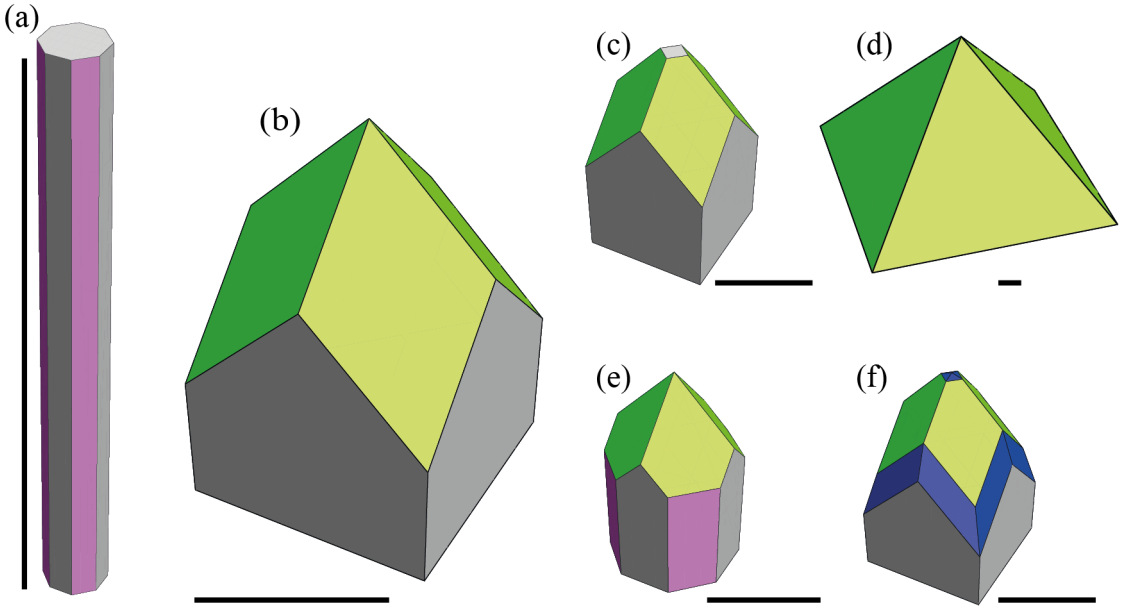

Figure 5.2.: (a) starting geometry used to simulate the final pyramidal geometry obtained using the parameter (b) $\alpha = 3.5$, $\beta = 0.1$ and $\gamma = 0.1$ (c) $\alpha = 2.9$, $\beta = 0.1$ and $\gamma = 0.1$ (d) $\alpha = 3.5$, $\beta = 0.1$ and $\gamma = 0.1$ (e) $\alpha = 3.5$, $\beta = 1.3$ and $\gamma = 0.1$ (f) $\alpha = 3.5$, $\beta = 0.1$ and $\gamma = 4.2$. (b,c,e and f) were overgrown with a total amount of $1\,\mu$m grown material (in (100) direction) and (d) with $15\,\mu$m. For all illustrations: The facets color of indicates its crystallographic direction: grey (100), green (111), blue (113) and pink (110) and the scale bar=$2\,\mu$m.

to the formation of pyramids with well-defined geometry and excellent uniformity across the sample. Based on the fourfold symmetry, the orientation of the pyramids with respect to the ⟨100⟩-oriented diamond surface, and the angle between the top facets, we identify these facets as {111}-planes of the diamond crystal. These observations are consistent with previous reports on diamond nanopillar overgrowth [122].

Due to the recently established formalism and the software by Bogatskiy et al. [126], we were able to understand the final pyramidal geometry. Diamond growth can be conveniently characterized in terms of the parameter α, β and γ [127, 128]. They are based on the inverse displacement speed V_{111}, V_{110}, and V_{113} of the (111), (110), and (113) faces during growth, normalized to the inverse displacement speed V_{100} of the (100) face. The different displacement speeds depend on the growth parameter chosen [125]. An example is the reported correlation between V_{113} and the deposition temperature [129]. The shape of the crystal is determined by kinetics; the slower the displacement speed of a crystalline plane, the larger the corresponding surface on the steady-state shape.

$$\alpha = \sqrt{3}\frac{V_{100}}{V_{111}}, \beta = \sqrt{2}\frac{V_{100}}{V_{110}}, \gamma = \sqrt{11}\frac{V_{100}}{V_{113}} \tag{5.1}$$

Utilizing the script published by Bogatskiy et al. [126], we identified conditions reproducing the experimentally observed pyramidal shape and studied the influence of different initial geometries. The cylindrical form of a nanopillar was approxi-

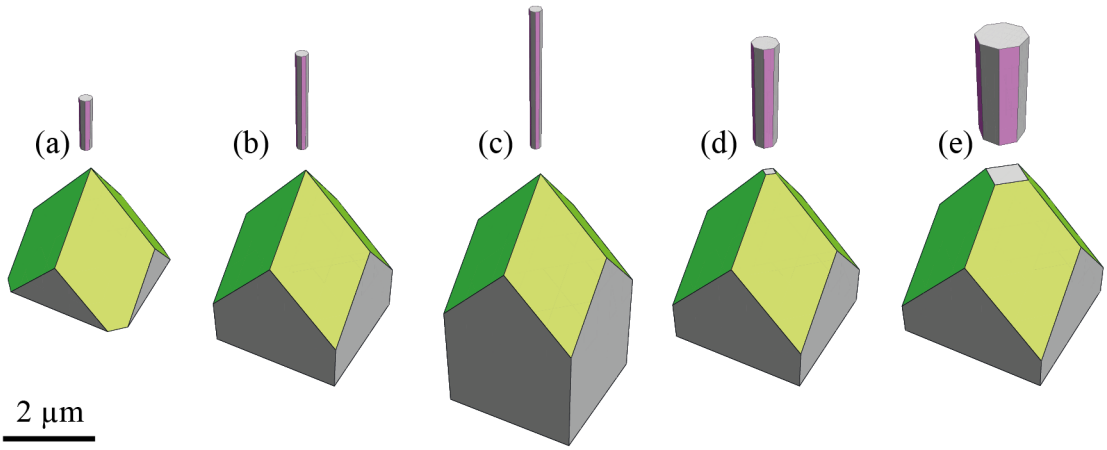

Figure 5.3.: For all the cases the overgrown structure was simulated for a total amount of 1 μm grown material (in (100) direction) assuming the growth parameter $\alpha = 3.5$, $\beta = 0.1$ and $\gamma = 0.1$ and varying the stating geometries (a) pillar hight h=1 μm, pillar diameter d=200 nm (b) h=2 μm, d=200 nm (c) h=3 μm, d=200 nm (d) h=2 μm, d=400 nm and (e) h=2 μm, d=800 nm .For all illustrations: The facets color of indicates its crystallographic direction: grey (100), green (111), blue (113) and pink (110).

mated with a 2 μm long pillar with an 200 nm diameter octagon base see Fig. 5.2(a). We found the most important parameter for the pyramid growth to be the α parameter characterizing V_{111}. For $\alpha \approx 3$ or higher, we found geometries similar to our pyramids (Fig. 5.2(b)). Smaller α parameters lead to a characteristic truncation (Fig. 5.2(c)) with a remaining {100}-facet on top of the pyramid, as found in previous reports [122]. If the sample is overgrown longer, it will eventually form a full pyramid (Fig. 5.2(d)). Next we studied the influence of the parameters β and γ and found that they need to satisfy the following conditions $\beta < 1$ or $\gamma < 4$ else the corresponding facets would show up on the overgrown structure. The result of $\beta \geq 1$ or $\gamma \geq 4$ can be found in Fig. 5.2(e) and (f).

Next, we studied the influence of different starting geometries on the pyramidal shape. We varied the length and width of the initial geometry and kept the overgrowth parameters constant for all simulations (see Fig. 5.3). We find that the variation of the pillar length results in different pyramid heights but has no influence on the geometry of the top facets (Fig. 5.3(a-c)). An increase in pillar diameter resulted in truncated pyramids with a remaining {100}-facet on top of the pyramid (Fig. 5.3(d) and (e)). When the amount of deposited material was increased, the simulated geometry featured a sharp pyramid tip again. We found a linear dependence between increased pillar diameter and material needed to preserve the tip shape.

For our application, we mostly care about a sharp tip. Under this assumption, critical parameters are α and the initial pillar diameter. The variation of the pillar length might be interesting for future geometry optimizations.

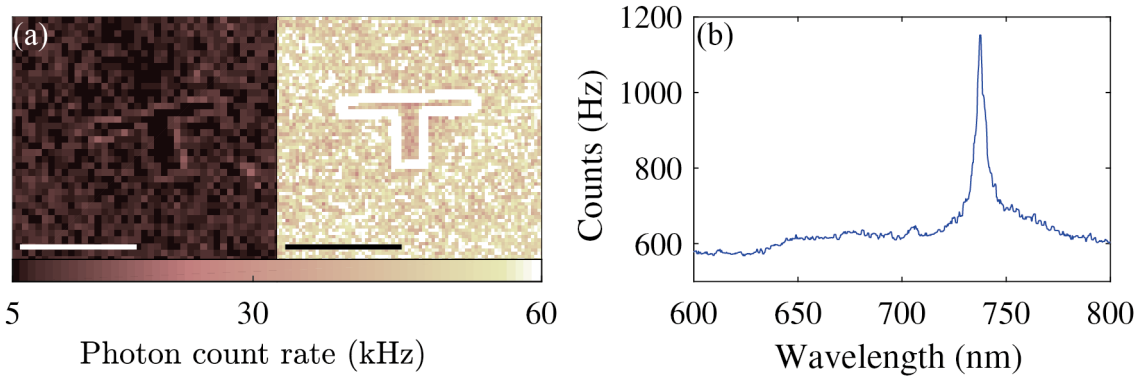

Figure 5.4.: (a) Confocal fluorescence map of the same part of an overgrown diamond substrate without pyramids before (left) and after (right) N implantation (excitation power: 150 μW). The visible "T-shaped" structure is an alignment marker. The scale bars in both images are 10 μm.(b) Fluorescence spectrum of a nanopyramid after implantation (excitation power: 20 μW).

5.2.3. Color center incorporation

To verify the initial absence of color centers, we acid cleaned the overgrown sample and then examined it in a home-built confocal microscope [18] with numerical aperture NA 0.8 and using continuous laser excitation at 532 nm. The acid clean prior to the examination is necessary, as diamond samples after overgrowth are typically by Hydrogen terminated (s. f. Chap.4). The inspection of as-grown samples showed no significant fluorescence, indicating the high purity of the overgrown and substrate materials (Fig 5.4(a) left panel).

After the sample was implanted with Nitrogen (Innovion; fluence: ^{14}N 3e11 ions/cm^2, energy: 12 keV, sample tilt: 7°), annealed (4 h at 400° C, 10 h at 800° C and 4 h at 1200° C) and acid cleaned, we observed significant increase in fluorescence from the diamond surface (Fig. 5.4(a))). A spectrum was taken on a diamond pyramid contained SiV$^-$ and NV$^-$ characteristics (Fig. 5.4(b))). More details to SiV and NV spectra can be found in Fig. 4.9. The appearance of stray SiV fluorescence in the implanted sample suggests that Si atoms were incorporated into the diamond during overgrowth. Implantation of nitrogen then provided the necessary vacancies for SiV creation during annealing.

Based on numerical modeling of the implantation process (SRIM software package) run with lattice binding energy 1.5 eV, surface binding energy 4.5 eV and displacement energy 45 eV [130–132], we expect the observed color centers to be located within $\sim$ 15 nm from the diamond surface (c. f. Fig. 5.5(a) NV:17±6 nm, SiV:12±6 nm) [56, 133], for the unstructured area. The mean of the simulated ion distribution defines the depth, and the square root of the variance the straggling. The estimations of the SiV depth are based on the assumption that SiV centers are predominantly created in regions where the implantation created vacancies. For the pyramids, it is more difficult to predict a distribution as it is unclear how the surface topography influences the implantation. If we assume an implantation in an angeled surface similar to the unstructured area, the expectation value for the color center depth would change to NV:12±5 nm, SiV:9±5 nm for the 47° and NV:9±5 nm, SiV:6±4 nm for the 61° angle (Fig. 5.5(b) and (c)). The chosen angles are the ex-

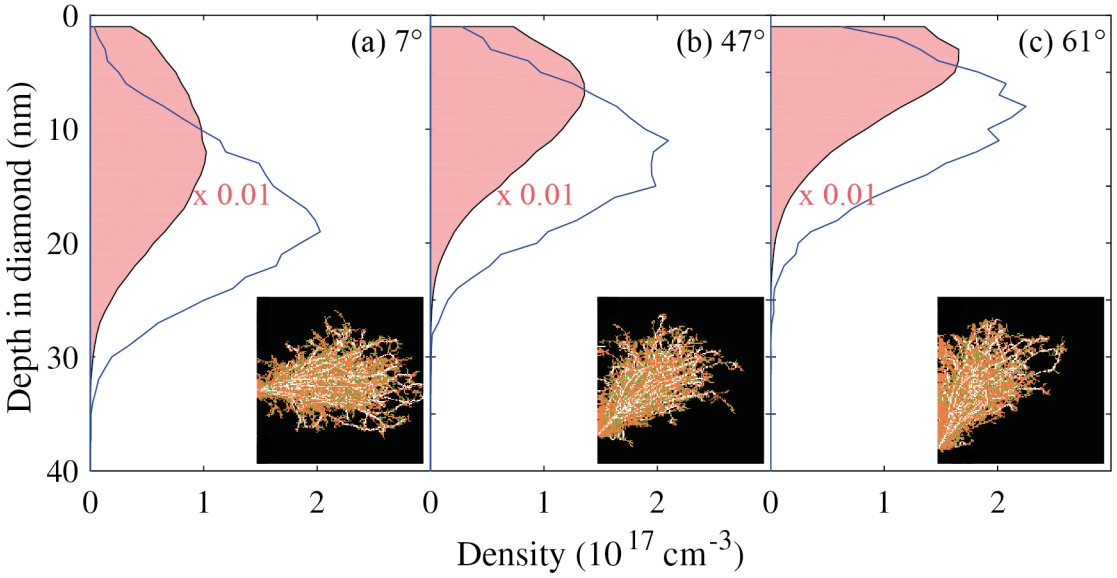

Figure 5.5.: Vacancy (light red surface scaled by 0.1) and nitrogen (blue line) densities as a function of depth from the diamond surface simulated with SRIM. Average over 10000 ions with the implantation parameter of 1e11 cm^{-2} ^{14}N 12 keV and an incidence angle (a) 7°, (b) 47° and (c)61°. For all panels the inset illustrates the trace of 100 simulated ions implanted at the respective angle.

treme cases where the incoming beam is either tilted (7°) towards or away from the ⟨111⟩-plane, approximating the angle between the ⟨111⟩ and the ⟨100⟩ plane with 54°. Another possible scenario is a more perpendicular implantation caused by a deformation of the field lines due to the sharp tip, similar to reports using diamond pyramids as emitter tips [121]. In this case, we would expect a vacancy and nitrogen distribution closer to Fig. 5.5(a), and possibly an increased concentration of implanted Nitrogen around the pyramid apex. To summarize, every implanted nitrogen ions creates about 60 vacancies on its way through the diamond until it settles into the crystal lattice, and we expect the color center to be located within the first 20 nm from the diamond surface. Further, we expect the SiV centers to be created more shallow than the NV centers.

5.3. Pyramid characterization

After the fabrication of SCD nanopyramids, we characterized the photonic properties and the final geometry of the pyramid apex and pyramid surface to assess the potential of SCD nanopyramids for application as sensor tips for nanoscale magnetometry.

5.3.1. Photonic properties

For a detailed characterization of the diamond pyramids' photonic properties, we focused on NV^- emission and suppressed unwanted signals from SiV^- emission by an appropriate short pass filter (Thorlabs FES0700, Cut-Off wavelength: 700 nm). A

resulting confocal map recorded through the pyramid-base (the fluorescence collection direction relevant for the scanning probe application we target in the future) is shown in Fig. 5.6(a). NV^- emission from the pyramids is significantly brighter than NV^- fluorescence from the nearby unstructured diamond, which already indicates efficient waveguiding and enhanced collection efficiencies from these structures [134]. The increased fluorescence collected from the pyramids could also be explained by preferential incorporation of Nitrogen into diamond material growing along the $\langle 111 \rangle$ direction [135]. We exclude this possibility because of the low N-density (less than 0.2 ppb) reported for a sample gown under the same conditions [125].

NV^- fluorescence from both the unstructured surface and from the pyramids exhibit clear signatures of optically detected electron spin resonance (ODMR) [136]. Figure 5.6(a) shows two representative ODMR traces, one from a pyramid and one from the surrounding unstructured surface. Both ODMR traces were measured with the same bias magnetic field applied in a direction not aligned with any of the diamond sample's symmetry axes to distinguish different NV families. Each NV family has a corresponding pair of ODMR lines. Interestingly, the majority of pyramids investigated show a single pair of ODMR lines, whereas the NV^- ensemble observed on the unstructured part of the diamond (Fig. 5.6(b)) shows four such pairs, as expected.

A statistical analysis of the number of ODMR lines observed in the pyramids allows for an estimation of the NV density in these structures. Out of a total of seven investigated pyramids, three showed a single pair of well-resolved ODMR lines, while the remaining pyramids had either two such pairs or unclear ODMR traces. Assuming a Poissonian distribution of the number of NV's per pyramid, the measured probability of 3/7 of observing a single ODMR line yields an expectation value of ~ 2.6 NVs per pillar. This estimation deviates by more than a factor of ten from our expected NV density. Using either our implantation parameters and the known $N \rightarrow NV^-$ conversion efficiency [137] or, alternatively and consistently, the brightness of NV^- fluorescence from the unstructured surface, compared to a well-known reference sample, we estimate an NV^- density of $\sim 30\ \mu m^{-2}$ in the sample under investigation. For the given pyramid footprint, this would result in an average number of 45 NV^- centers per pyramid, in stark contrast to our above estimation. As we will show in the following, this discrepancy results from the nanophotonic properties of the pyramids: Optical waveguiding is most efficient for NV centers in the vicinity of the pyramid apex, and as a result, our experiment most efficiently detects NV fluorescence from this subset of NVs only.

No ODMR signal could be detected when the pyramids were measured though the pyramid apex ("top-collection"). Measuring saturation curves Fig. 5.6(c), through top-collection and thought the pyramid base and diamond substrate (further referred to as "bottom-collection") we find a strong directionality. Fitting the signal with the following equation, we can isolate the NV fluorescence the background signal [138].

$$I(P) = \frac{I_{\mathrm{sat}}}{1 + \frac{P_{\mathrm{sat}}}{P}} + bP \tag{5.2}$$

Where I(P) is the measured intensity as a function of the applied laser power P, P_{sat} is the saturation power, I_∞ the saturation counts and bP accounts for the background. The data collected through top-collection appear linear, indicating a

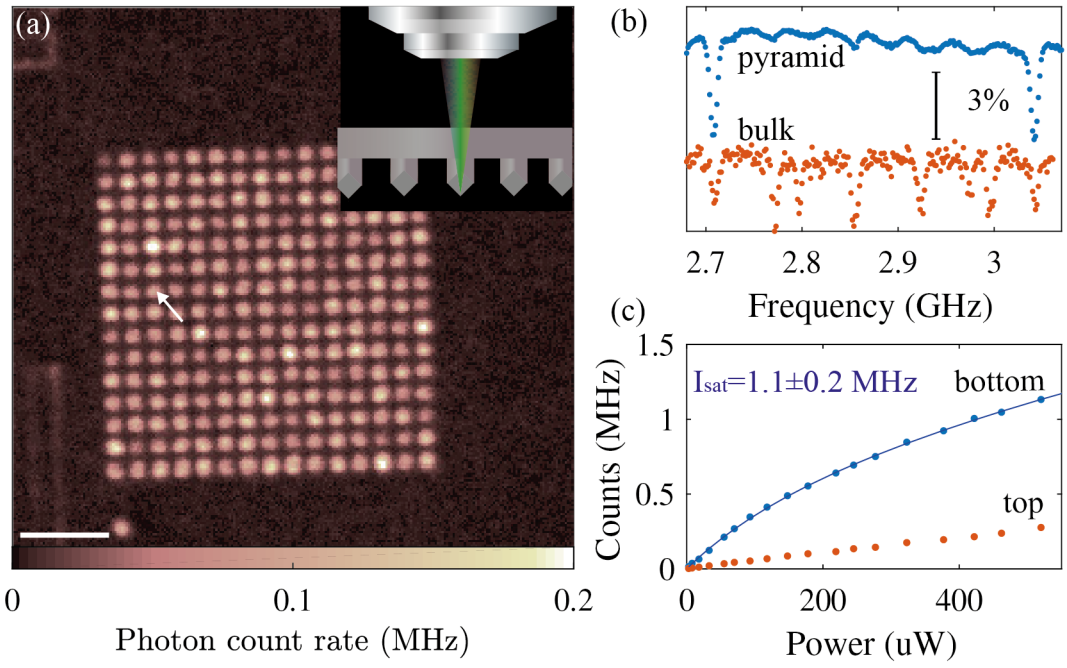

Figure 5.6.: (a)Confocal image of an array of overgrown pyramids with fluorescence collected using a short pass filter at 700 nm. The pyramid used for the measurements in (b) and (c) is indicated with an arrow. Inset: schematic of the sample orientation during measurement. The scale bar equals 10 μm. (b) Optically detected electron spin resonance from the diamond nanopyramid indicated in (a) and from surrounding bulk. The single pair of ODMR lines observed in many pyramids indicates a fluorescence signal originating from only a few NVs. (c)Fluorescence saturation curves collected from the top (red) and bottom (blue) side of the same diamond pyramid. The curve collected through bottom-collection is fitted with Eq. (5.2).

very low NV fluorescence contribution compared to the background signal. This result is consistent with the lack of measurable ODMR signal. In comparison, the fluorescence collected through bottom-collection has significant NV content. Fitting the fluorescence saturation curve with Eq. (5.2) gives saturation counts of 1.1 MHz, nearly twice as much as measured in the same setup with solid immersion lenses on single NVs [139]. For single NV emission, this would be amongst the highest saturation count-rates reported. However, due to the high background, it was not possible to confirm the NV number with correlation measurements.

In order to experimentally assess the photonic properties of the nanopyramids, we measured the angular emission patterns from the embedded NV^- centers by back focal plane (BFP) imaging. In this imagining technique, all the light emitted from the sample plane in the same direction is focused on one point in the back focal plane. Hence, a BFP image contains information about the angular distribution of the light emitted from the sample plane. A description of the technique can be found in Ref. [140].

Fig. 5.7(a) top and bottom show, respectively, the resulting BFP emission patterns for NV^- collection through the pyramid apex and through the pyramid base and substrate. In these subfigures and the following, white circles indicate collection

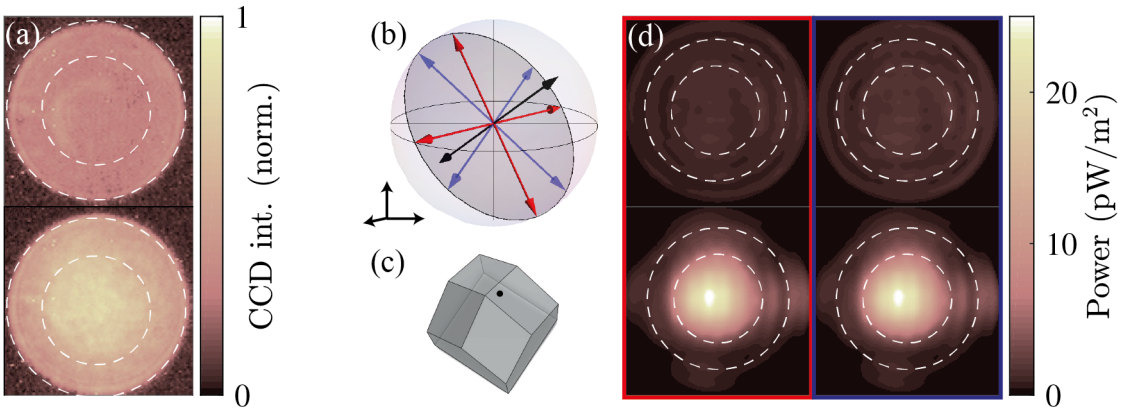

Figure 5.7.: (a) Experimentally measured back focal plane images of emission from a representative pyramid, for top and bottom collection (top and bottom row, respectively) (b) Coordinate system with a unit sphere at the origin. One NV direction is drawn as a black arrow with a gray area marking the plane perpendicular to the NV direction. Illustration of the dipoles (red and blue set of arrows) used to simulate the NV emission. (c) Position of the NV used for the simulation. (d) Simulation of far-field power distribution patterns collected from the pyramid top and bottom (top and bottom row, respectively). Left and right panels are simulations of the same NV assuming different dipole sets, the red dipoles in (b) were used in the simulations shown in the left and blue for the simulation shown in the right panel. The white circles in all panels indicate the NA 0.8 and 0.5.

NA's of 0.5 and 0.8 (the NA of our collection optics). While top-collection shows diffuse emission into the whole collection NA, bottom-collection shows a BFP emission pattern that is more centered on the optical axis and shows emission predominantly within a collection NA of ~ 0.5.

NV^- emission from the nanopyramids shows significant directionality: Approximately five times more fluorescence light is emitted to the bottom compared to the top side, as evidenced by both the signal integrated over the BFP images and the fluorescence saturation curves collected from the top and bottom sides for the same pyramid (Fig. 5.6(c)). This observed directionality of color center emission from nanopyramids is in qualitative agreement with previous reports [134, 141].

For a better understanding of the observed BFP emission patterns, we performed numerical simulations using the finite-difference time-domain (FDTD) module of the commercially available software Lumerical. We replicate the ideal pyramidal geometry with a nanometer sharp tip, placed individual optical dipoles emulating NV^- emission onto selected locations on one of the top facets of the pyramid and at a depth of 20 nm below the diamond surface and calculated the far-field emission patterns corresponding to our top- and bottom-collection BFPs (Fig. 5.7(d), top and bottom row, respectively). The NV emission is typically approximated with one or two dipoles lying in the plane perpendicular to the NV axis. For our simulation, we randomly assigned one of the four possible NV directions and used the dipole orientations (relative to the NV) indicated by red arrows in Fig. 5.7(b). To exclude interference effects between these dipoles, they are simulated separately, and the resulting far fields are added incoherently, averaging over the spectral range collected

in our measurement (650 nm-700 nm). To test our approach, we repeat the simulations for one NV position and orientation (Fig. 5.7(c)) with a different set of dipoles, indicated by blue arrows in Fig. 5.7(b). The resulting far-field emission patterns can be seen in Fig. 5.7(d). The resulting pattern is indistinguishable, which supports the validity of our method.

The simulations qualitatively reproduce our experimental BFP images and show a clear tendency of waveguiding of NV^- emission towards the pyramid bottom. We attribute small differences to a difference in position on the pyramid surface and additional NVs contributing to a background. To quantify the directionality we consider the commonly used collection factor [74]

$$\xi = \frac{\Gamma_{\mathrm{NA}}}{\Gamma_{\mathrm{hom}}}, \tag{5.3}$$

where Γ_{hom} is the radiative emitter decay rate in a homogeneous medium and Γ_{NA} is the rate of far field photons emitted into the collection NA (here with NA=0.8). Additional to that we introduce ξ_{rad} to account for the difference in lifetime due to the change of dipole environment. The decrease in effective refractive index leads to a reduction of the radiative density of states resulting in an increase in radiative lifetime [142].

$$\xi_{\mathrm{rad}} = \frac{\Gamma_{\mathrm{NA}}}{\Gamma_{\mathrm{rad}}}, \tag{5.4}$$

where Γ_{rad} is the radiative emitter decay rate in the actual dipole position. The waveguiding properties of our pyramids can best be understood considering ξ_{rad}, because it is normalized to the photons that have been emitted. However, as we have to consider not only the waveguiding properties but also the impact of the dipole environment ξ is the important value for the comparability of our pyramids with other photonic structures.

In Fig. 5.8, the collection factors ξ (panels (a,c)) and ξ_{rad} (panels (b,d)) are shown as a function of the NV position on the pyramid. The simulation was performed for a selection of 110 randomly placed NVs with random assigned NV direction. NVs with same distance from the apex but different ξ^{bottom} correspond to different azimuthal positions of the NVs (see inset to Fig. 5.8) and/or different dipole orientations assigned to the same NV position. In addition to the bottom-collection (c) and (d) also the top-collection is represented. The average top and bottom-side collection factor, we find ξ^{bottom}= 0.14 and ξ^{top}=0.045. Their ratio $\xi^{\mathrm{bottom}}/\xi^{\mathrm{top}} = 3.48$ is in close agreement with our experimental finding of $\xi^{\mathrm{bottom}}/\xi^{\mathrm{top}} \sim 3.0$ and previous reports on similar structures [122, 134]. If only the NVs close to the tip (r < 50 nm) are considered, the bottom collection factor found is even slightly higher ξ^{bottom}= 0.15 than otherwise.

Our simulations also shed light on our observed discrepancy between the NV^- density estimated from the optical (ODMR) signal from the pyramids as compared to the estimated NV^- density based on implantation parameters (Fig. 5.6(b)). Specifically, we find that ξ^{bottom} is strongly depending on the lateral NV^- location within the pyramid surface (Fig. 5.8(c)). NVs closer to the pyramid apex experience a stronger waveguiding effect, with ξ^{bottom} peaking at $\xi^{\mathrm{bottom}}_{\mathrm{max}} \sim 0.5$ for r $\sim$ 150 nm. For NVs closer to the apex ξ^{bottom} drops again. This drop can be explained by a combination of two effects. First a decrease in the total rate of radiated photons

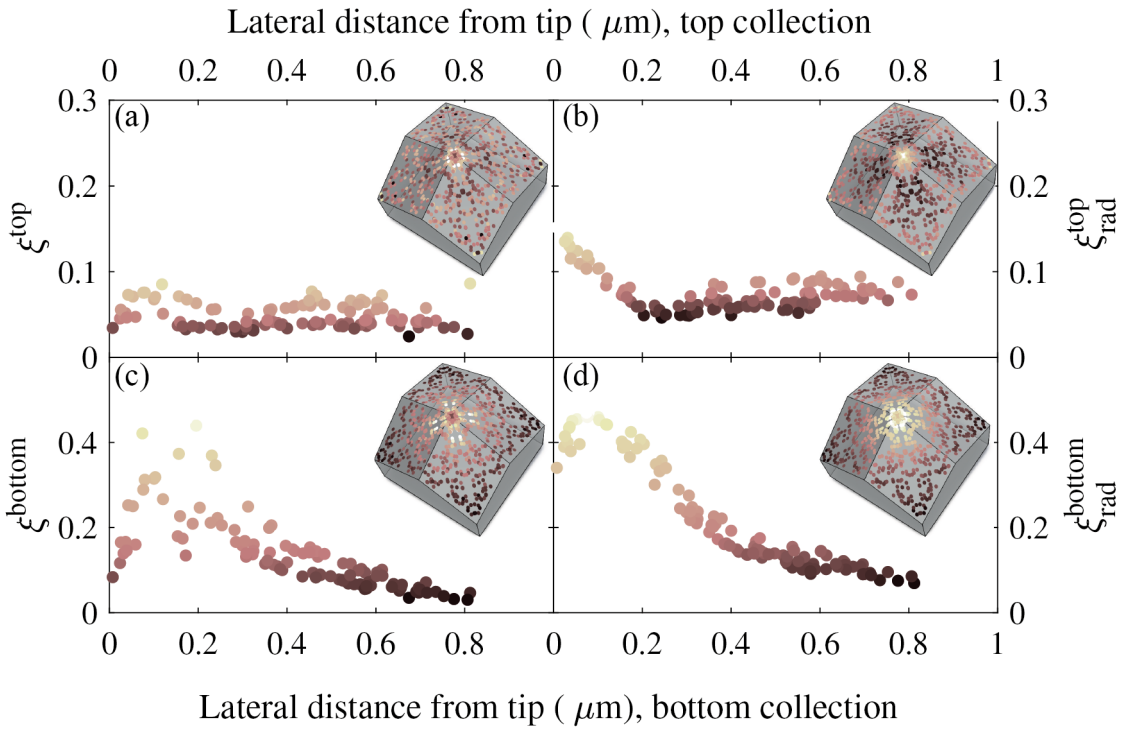

Figure 5.8.: Collection efficiency ξ(left panels) or ξ_{rad} (right panels) for NA = 0.8 through the pyramid (a,c) bottom or (b,d) top, as a function of radial distance between NVs and the pyramid apex. The inset shows the NV locations considered, where the color of the points encodes the value of ξ (respectively (ξ_{rad}).

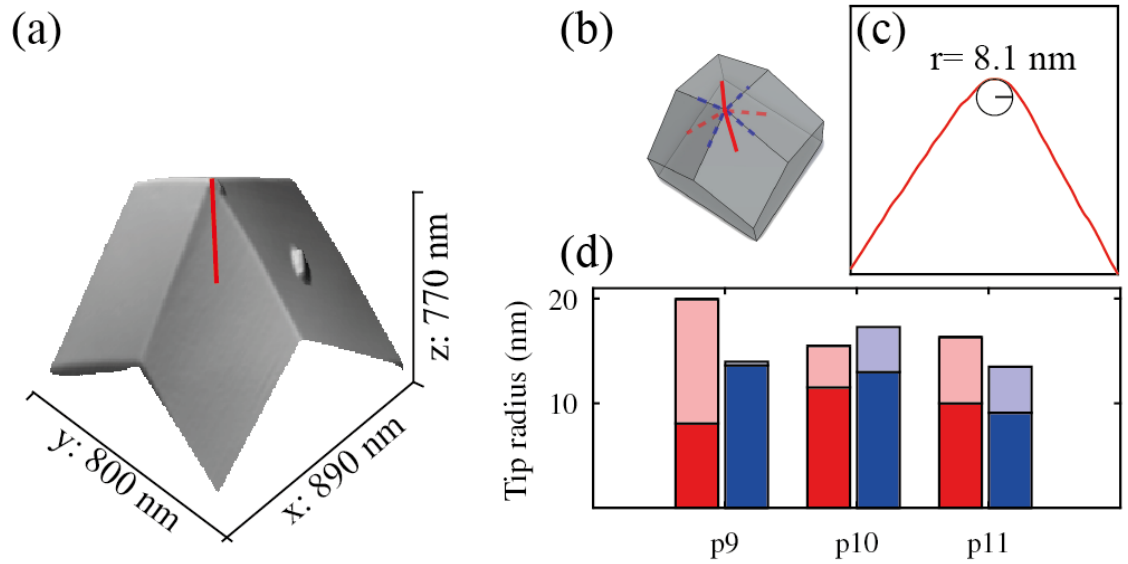

Figure 5.9.: (a) AFM image of pyramid top facets. (b) Schematic sketch of a pyramid with colored lines indicating the positioning of the line cuts (blue: along the edge or red: across the facet) used to fit the tip radii in (d). (c) Line-cut through the AFM structure highlighted in (a), with osculating circle fitted to the tip (black) (d) Histogram of tip radii for three different pyramids. The darker (light) bar indicates the minimal (maximal) radii measured on each pyramid, whereas colors symbolize the direction of the line cut.

due to an increase in radiation lifetime. This can be understood comparing the collection efficiency normalized to the emission of a dipole in a homogeneous substrate (Fig. 5.8(c)) with the collection efficiency normalized to the photons emitted by a dipole in the actual sample geometry (Fig. 5.8(d)). Authors of [143] found the smallest elementary volume influencing the effective refractive index to be a sphere with radius on the order of $\lambda/4$. Assuming λ=700 nm this is in good agreement with the observed decrease for NVs positioned at a distance of less than $\sim$ 150 nm. The second effect is an increase in waveguiding towards the top for NVs located closer to the pyramid tip visible in ξ^{top} (Fig. 5.8(a)) and $\xi^{\mathrm{top}}_{\mathrm{rad}}$ (Fig. 5.8(b)).

For a qualitative estimate of the NV number contributing to the collected fluorescence signal we assume the NV signal collected though bottom collection to be dominated by the NVs with $\xi^{\mathrm{bottom}} > \xi^{\mathrm{bottom}}_{\mathrm{max}}/2$. From our previous NV density estimate of ($\sim 30\mu m^{-2}$), we then expect the majority of the emission to come from approximately three NVs. This estimation is in good agreement with our estimate based on the ODMR measurements. We stress that further factors might add to this qualitative argument to explain the lower NV density we observe in the nanopyramids compared to their surroundings. These include potential distortions of electric field lines by the nanopyramids during the ^{14}N implantation process, which could lead to non-uniform implantation profiles.

5.3.2. Tip and surface characterization

One of the key benefits of working with bottom-up fabricated structures is the increased surface quality of CVD grown diamond compared to diamond etched in a plasma. To characterize and quantify the surface quality and sharpness of our diamond pyramid tips, we performed detailed AFM imaging on representative pyramids from our sample (Fig. 5.9(a)). The AFM image reflects the pyramidal shape of the tips already seen in our SEM investigation (Fig. 5.1) and shows flat crystal facets without visible dislocations or crystal terraces. The surface roughness with root-mean-square amplitude < 1 nm of the top facets of the pyramids is consistent with surface roughness reported for diamond grown under similar conditions [144]. More importantly, our AFM image confirms the sharpness of the pyramid tips already visible in Fig. 5.9. To quantify the tip sharpness, we extracted line cuts across pyramid facets and edges as illustrated in Fig. 5.9 (b) and fitted osculating circles to these line profiles (Fig. 5.9(c)). Fig. 5.9(d) summarizes our findings and shows the minimal and maximal radii found in each direction for a selection of three pyramids. Importantly, all tip radii found were in the range 8 nm to 20 nm, which on the one hand demonstrates the remarkable sharpness of theses tips and on the other hand suggests that the values determined here are not masked by the radius of the AFM tip employed for imaging.

5.4. Summary and Outlook

With our work, we have shown the potential of diamond pyramids created by CVD overgrowth of diamond nanopillars as an attractive avenue for future all-diamond scanning probe quantum sensors. We demonstrated a scalable process that yields sharp diamond pyramids forming highly attractive, robust tips for high-resolution AFM in general and nanoscale quantum sensing in particular. In the latter case, the sharpness of the tip would ensure close proximity of a color-center quantum sensor placed at the apex of the pyramid to a sample of interest. An improvement over existing approaches [17], which could promote spatial resolution in such imaging to the sub-10 nm range. Furthermore, we demonstrated that the pyramids are effective photonic nanostructures, which yield high-efficiency fluorescence collection, on par with currently available nanoscale quantum sensing technologies [17, 145]. The high collection efficiency, combined with the possibility to tailor the overgrown diamond material to the needs of the application, make this approach an attractive and versatile method. Such enhancement overgrowth includes native diamond surfaces with isotropically purified SCD, supporting long spin coherence times for near-surface color center spins [146], or phosphor doped SCD for a higher NV^- yield obtained by specific Fermi level engineering to stabilize charge states not naturally occurring in diamond [48].

Our hopes of increased coherence times of NV spins in overgrown diamond could not be proven due to the high background fluorescence obstructing the necessary measurements. Along these lines the purity of the overgrown diamond is a point that should to be optimized together with two key steps that still need to be addressed in order to employ such diamond pyramids for scanning probe quantum sensing experiments: The overgrowth method demonstrated here has to be combined with

scanning probe fabrication, and individual color centers need to be controllably created at the pyramid apex. The first requirement can easily be met since scanning probe fabrication procedures are readily applicable to the diamond pyramids realized here. Color-center creation at the pyramid apex appears more challenging but could be achieved by ion implantation with nanoscale resolution, either by nano-implantation through AFM tips [147] or through focused-ion beam implantation of color centers [148].

6. Summary and outlook

Color center-based sensing is a field with a bright future in fundamental research and commercial applications. The fabricated structures in the semiconductor industry become smaller, more fragile, and the resulting devices less power consuming. These developments open up the need for highly sensitive, non-intrusive methods for quality control and process optimization. For such tasks and when it comes to developing new devices based on novel scientific concepts, the NV is a handy measurement tool. All these applications profit from optimizing the diamond surface, as this directly translates into an increase in sensitivity and spatial resolution. Spatial resolution benefits because the ideal surface stabilizes the charge state, relevant for sensing even if the color center is incorporated only 1-2 nm below the diamond surface to reduce the sensor-to-sample distance. The resulting increase in sensitivity would be twofold first due to the smaller sensor-to-sample distance and second due to an increase in coherence time.

6.1. Summary

We start this thesis by drawing the bigger picture and giving an idea of the endless potential of color centers for future applications in the different fields of quantum technologies. Next, we introduce the approach of color center-based sensing in combination with atomic force microscopy.

We give the reader an introduction to the material properties of diamond and introduce the two most promising color centers for quantum sensing - the SiV and NV center. Then we give an impression, how color center-based measurements are implemented and show a state of the art quantum sensor based on the NV center.

In the next chapter, we focus on the state of the art, the oxygen terminated diamond with shallow implanted NV centers. We give an overview of the theoretical and experimental work done by other groups and discuss different treatment protocols for oxygen surface termination and removal of damaged diamond layers. We introduce two methods, namely XPS and NV-based sensing protocols, to evaluate different surface terminations and discuss their advantages and limitations conducting a series of measurements on plasma-treated diamond surfaces. We find a probable source of decoherence, suggest further experiments to confirm our notion, and identify the most promising protocols to reduce the plasma introduced spin noise.

The following chapter discusses the hydrogen surface termination of diamond and different charge states of the SiV and NV centers. We first introduce the concepts of energy bands, band bending, and Fermi level for the intrinsic and nitrogen-doped diamond and then discuss the impact on color centers present in the diamond lattice. We successfully established a hydrogen termination protocol and confirmed its performance and reversibility by XPS and NV fluorescence measurements. We propose hydrogen termination as a potential new approach to stabilize shallow neutral

SiV centers and conduct the first series of tests at room and cryogenic temperatures. Further, we discuss the potential of hydrogen termination as the starting point of other chemical functionalizations and present a new idea combining thermal surface treatments with laser writing. Finally, we conduct KPFM measurements on hydrogen and oxygen terminated diamond with and without water present to investigate the diamond surface further.

After discussing different possibilities to modify the diamond surface, we concentrate, in the fifth chapter, on the optimization of the scanning probe geometry. We present a new technique based on the bottom-up overgrowth of a top-down fabricated template. We characterize the resulting geometry by AFM and SEM and find a pyramidal structure with smooth facets and a sharp tip with a radius on the order of 10 nm. We study the photonic properties of the structures by measuring the emission profile of incorporated color centers and conducting a series of numerical simulations. We find excellent collection efficiencies from the color centers situated close to the pyramid apex.

6.2. Outlook

In our work, we presented several different ways to overcome material limitations to quantum sensing imposed by the diamond surface. To conclude, we will present suggestions concerning the next steps for the surface and sensor geometry optimization for NV-based sensing and propose possible future experiments for the neutral SiV center.

In order to be able to present new and better surface terminations to stabilize near-surface NV centers, we first need to implement the best-known termination, as reference for different terminations. From our literature research and personal experience, we consider the annealing in dry oxygen atmosphere followed by a clean with piranha the best currently investigated termination. In parallel, we suggest investigating the reduction of oxygen terminated diamond by borane as it has been reported to perform very well for nanodiamonds [83]. An alternative approach to the borane reduction could be the annealing in water vapor, which has been reported to result in a -OH termination as well [149].

In parallel to the surface optimization, we want to continue the integration of the diamond nano pyramids into our standard sample fabrication routine. Cantilevers with such tips would yield higher topographical resolutions, better control over sensor-to-sample distance, and less sensibility to small tilts during the sample mounting. The controlled implantation into the pyramid apex needs to be implemented. Further, the diamond overgrowth parameters need to be adjusted to reduce Si atoms incorporation during overgrowth in order to be able to study the coherence properties of the NV centers in overgrown diamond. A reduced background signal would allow confirming the expected enhanced performance of shallow NV centers implanted into native diamond compared to shallow NV centers in diamond nanostructures fabricated using plasma-based etch protocols.

For the neutral SiV, the next important step is to verify its existence by measuring its spectral signature. If the current experiments do not prove fruitful, more shallow centers could be a possibility to increase the band bending effect and favor the

neutral charge state even more. Also, a study of the negative charged NV could lead to further insights concerning possible line shifts the neutral SiV could experience. We believe the understanding of the behavior of the charge state at low temperature to be a key to the next phase of color center-based sensing.

The ideal ultimate structure for nanoscale quantum sensing with single NV centers might consist of a combination of pyramid-shaped tips with optimized surface termination to stabilize shallow NV center spins. This thesis has laid the groundwork for these developments, which may lead to further performance enhancements of this promising new nanoscale imaging and sensing technology.

A. Appendix

A.1. Hydrogen termination protocol

Detailed instructions to conduct the hydrogen-termination of diamond samples utilizing a quartz tube furnace. This description is intended to serve as a guide for future group members.

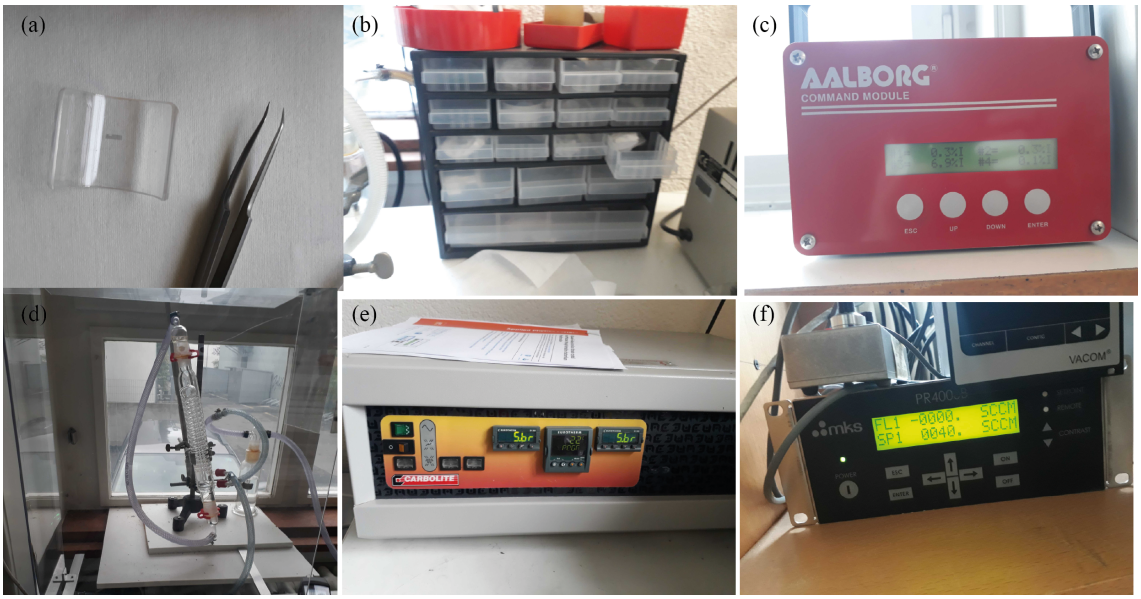

Figure A.1.: (a) sample on glass carrier (b) storage place of glass carrier (c) Argon mass flow control (d) water trap (e) control unit of the oven; green button to turn oven on; orange to turn on heating (f) mass flow control for the hydrogen gas

1. prepare the sample by acid cleaning it and removing it from the silicon substrate
2. reserve oven on the whiteboard (on the wall to the left of the oven)
3. put on gloves
4. change to the glass tube specifically reserved for diamond H-termination (if not in the oven, it should be in the rack below the table). This is the tube which has holes in the heat shields and no metal cuff
5. connect the tube to the gas line and the water trap
6. open the tube, put the sample on glass carrier, insert the carrier into the tube and push it to the middle of the glass tube using a bent wire, insert heat shield and close tube

7. flush the tube for 10 min with Argon:
   a) open Argon bottle
   b) open the valve between the gas bottle and the mass flow control and the valve on the gas tube to the oven .
   c) open the Argon mass flow control (channel 3 → press next → press open)
8. while Argon flushing
   a) for safety reasons open window (small window in the corner to the top right of the gas bottles) and turn off the air conditioning (red knob on the wall to the right of the gas bottles)
   b) check the connections to the hydrogen generator and make sure nothing has changed, and no valve is open
   c) turn generator on (switch on the backside and start button on the front). If there is an error message, do not worry, it happens frequently. Just restart (repress button on the front), if the error remains, refill water (user manual). If the error is still not gone contact Daniel Sacker
   d) turn oven on and control the temperature set (lower number on display), if the temperature is not set to 750° C use up and down arrows to set the temperature
9. press open on the generator to start hydrogen flow
10. open valve before and after hydrogen mass flow control
11. set mass flow control to 40 sccm, and press ok. If gas is flowing, a small blue lamp will blink at the side of the mass flow control unit.
12. stop Argon flow and start oven (flip orange switch)
13. it takes approximately 30 minutes until the oven reaches temperature
14. when the oven is on temperature, make sure that the water trap still bubbles (indicating an overpressure inside the tube) if that is not the case immediately add some Argon flow, and make sure the hydrogen generator runs properly
15. anneal sample for 6 hours
16. to cool down, start the Argon again and stop the oven
17. at a temperature of 600° C open the lid of the oven, be careful not to burn yourself
18. at a temperature of 200° C stop hydrogen flow (close both valves, stop the gas flow and press close on the generator)
19. turn off Argon and take the sample out when the temperature is below 100° C. (open the tube and fish the carrier out using a bent wire)
20. turn off hydrogen generator, close the window and turn the air conditioning back on

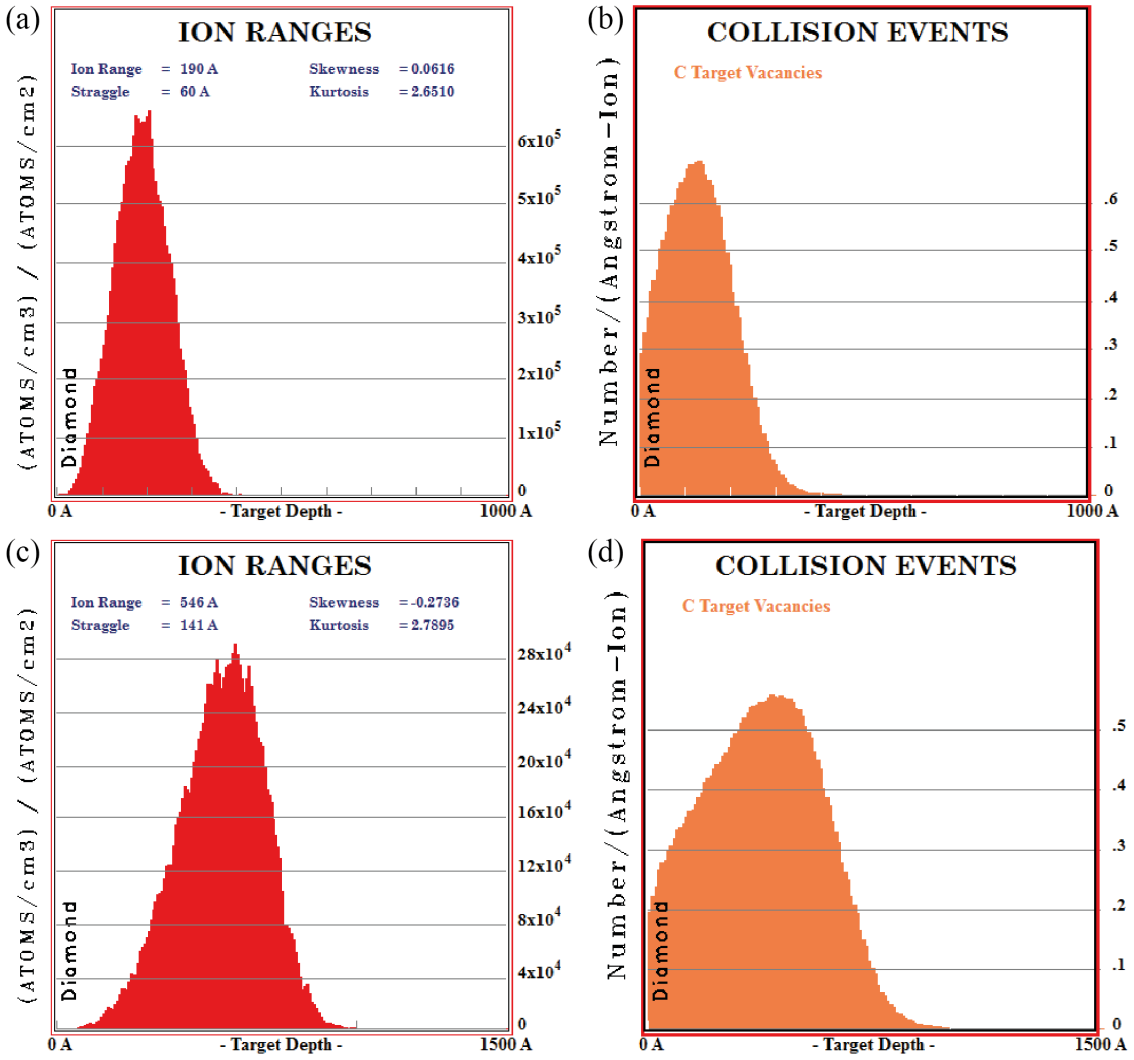

Figure A.2.: Output of SRIM calculations for the implantation parameter (a, b) Si ions, 25 keV, 7° and (c, d) Si ions, 80 keV, 7°. A total of 10000 ions were simulated for both parameter sets.

A.2. SRIM

Srim simulations are typically used to estimate the implantation depth [150]. Here two different sets of Si ion implantation parameters are simulated. The left panels (Fig. A.2(a and (c)) show the expected ion distribution and the left (Fig. A.2(b) and (d)) panels the created vacancies. The following parameters were used to model the diamond substrate: lattice binding energy 1.5 eV, surface binding energy 4.5 eV and displacement energy 45 eV [130–132]. The extracted ion ranges are 19±6 nm for the 25 keV and 55±14 nm for the 80 keV implantation.

B. Bibliography

[1] Gordon E. Moore, *Cramming more components onto integrated circuits*, Electronics **38** (1965).

[2] Stacy Smith, https://newsroom.intel.com/editorials/moores-law-setting-the-record-straight/.

[3] V. Baltz, A. Manchon, M. Tsoi, T. Moriyama, T. Ono, and Y. Tserkovnyak, *Antiferromagnetic spintronics*, Reviews of Modern Physics **90** (2018).

[4] A. V. Zasedatelev, A. V. Baranikov, D. Urbonas, F. Scafirimuto, U. Scherf, T. Stferle, R. F. Mahrt, and P. G. Lagoudakis, *A room-temperature organic polariton transistor*, Nature Photonics **13**, 378 (2019).

[5] A. Joesaar, S. Yang, B. Bgels, A. van der Linden, P. Pieters, B. V. V. S. P. Kumar, N. Dalchau, A. Phillips, S. Mann, and T. F. A. de Greef, *DNA-based communication in populations of synthetic protocells*, Nature Nanotechnology **14**, 369 (2019).

[6] I. Aharonovich, S. Castelletto, D. A. Simpson, C.-H. Su, A. D. Greentree, and S. Prawer, *Diamond-based single-photon emitters*, Reports on Progress in Physics **74**, 076501 (2011).

[7] S. Wehner, D. Elkouss, and R. Hanson, *Quantum internet: A vision for the road ahead*, Science **362**, eaam9288 (2018).

[8] L. Rondin, J.-P. Tetienne, T. Hingant, J.-F. Roch, P. Maletinsky, and V. Jacques, *Magnetometry with nitrogen-vacancy defects in diamond*, Rep. Prog. Phys. **77**, 56503 (2014).

[9] C. Degen, F. Reinhard, and P. Cappellaro, *Quantum sensing*, Reviews of Modern Physics **89**, 035002 (2017).

[10] L. Thiel, D. Rohner, M. Ganzhorn, P. Appel, E. Neu, B. Mller, R. Kleiner, D. Koelle, and P. Maletinsky, *Quantitative nanoscale vortex imaging using a cryogenic quantum magnetometer*, Nature Nanotechnology **11**, 677 (2016).

[11] J.-P. Tetienne, T. Hingant, J.-V. Kim, L. H. Diez, J.-P. Adam, K. Garcia, J.-F. Roch, S. Rohart, A. Thiaville, D. Ravelosona, and V. Jacques, *Nanoscale imaging and control of domain-wall hopping with a nitrogen-vacancy center microscope*, Science **344**, 1366 (2014).

[12] L. Thiel, Z. Wang, M. A. Tschudin, D. Rohner, I. Gutirrez-Lezama, N. Ubrig, M. Gibertini, E. Giannini, A. F. Morpurgo, and P. Maletinsky, *Probing magnetism in 2D materials at the nanoscale with single-spin microscopy*, Science **364**, 973 (2019).

[13] C. Du, T. Van der Sar, T. X. Zhou, P. Upadhyaya, F. Casola, H. Zhang, M. C. Onbasli, C. A. Ross, R. L. Walsworth, Y. Tserkovnyak, and A. Yacoby, *Control and Local Measurement of the Spin Chemical Potential in a Magnetic Insulator*, Science **357**, 195 (2017).

[14] B. M. Chernobrod and G. P. Berman, *Spin microscope based on optically detected magnetic resonance*, Journal of Applied Physics **97**, 014903 (2005).

[15] G. Balasubramanian, I. Y. Chan, R. Kolesov, M. Al-Hmoud, J. Tisler, C. Shin, C. Kim, A. Wojcik, P. R. Hemmer, A. Krueger, T. Hanke, A. Leitenstorfer, R. Bratschitsch, F. Jelezko, and J. Wrachtrup, *Nanoscale imaging magnetometry with diamond spins under ambient conditions*, Nature **455**, 648 (2008).

[16] S. Kuhn, C. Hettich, C. Schmitt, J. Poizat, and V. Sandoghdar, *Diamond colour centres as a nanoscopic light source for scanning near-field optical microscopy*, J. Microsc. **202**, 2 (2001).

[17] P. Maletinsky, S. Hong, M. S. Grinolds, B. Hausmann, M. D. Lukin, R. L. Walsworth, M. Loncar, and A. Yacoby, *A robust scanning diamond sensor for nanoscale imaging with single nitrogen-vacancy centres*, Nature Nanotechnology **7**, 320 (2012).

[18] P. Appel, E. Neu, M. Ganzhorn, A. Barfuss, M. Batzer, M. Gratz, A. Tschpe, and P. Maletinsky, *Fabrication of all diamond scanning probes for nanoscale magnetometry*, Review of Scientific Instruments **87**, 063703 (2016).

[19] B. Myers, A. Das, M. Dartiailh, K. Ohno, D. Awschalom, and A. Bleszynski Jayich, *Probing Surface Noise with Depth-Calibrated Spins in Diamond*, Physical Review Letters **113**, 027602 (2014).

[20] A. Zaitsev, *Optical Properties of Diamond A Data Handbook*, (Springer Berlin Heidelberg, Berlin, Heidelberg) (2001).

[21] Friedrich Mohs, *Grundriss der mineralogie.*, Zweite Theil. Physiographie. (in der Arnoldischen Buchhandlung, Dresden) (1824).

[22] Q. Wei and J. Narayan, *Superhard diamondlike carbon: preparation, theory, and properties*, International Materials Reviews **45**, 133 (2000).

[23] J. E. Field (editor), *The Properties of natural and synthetic diamond* (Academic Press, London ; San Diego) (1992).

[24] R. Kalish, *Diamond as a unique high-tech electronic material: difficulties and prospects*, Journal of Physics D: Applied Physics **40**, 6467 (2007).

[25] C. J. Wort and R. S. Balmer, *Diamond as an electronic material*, Materials Today **11**, 22 (2008).

[26] K. M. Itoh and H. Watanabe, *Isotope engineering of silicon and diamond for quantum computing and sensing applications*, MRS Communications **4**, 143 (2014).

[27] G. Balasubramanian, P. Neumann, D. Twitchen, M. Markham, R. Kolesov, N. Mizuochi, J. Isoya, J. Achard, J. Beck, J. Tissler, V. Jacques, P. R. Hemmer, F. Jelezko, and J. Wrachtrup, *Ultralong spin coherence time in isotopically engineered diamond*, Nature Materials **8**, 383 (2009).

[28] B. Jamtveit and P. Meakin, *Growth, Dissolution and Pattern Formation in Geosystems.*, (Springer Netherlands, Dordrecht) (2010).

[29] M. W. Doherty, N. B. Manson, P. Delaney, F. Jelezko, J. Wrachtrup, and L. C. L. Hollenberg, *The nitrogen-vacancy colour centre in diamond*, Physics Reports **528**, 1 (2013).

[30] J. R. Maze, A. Gali, E. Togan, Y. Chu, A. Trifonov, E. Kaxiras, and M. D. Lukin, *Properties of nitrogen-vacancy centers in diamond: the group theoretic approach*, New J. Phys. **13**, 025025 (2011).

[31] C. Schreyvogel, V. Polyakov, R. Wunderlich, J. Meijer, and C. E. Nebel, *Active charge state control of single NV centres in diamond by in-plane Al-Schottky junctions*, Scientific Reports **5**, 12160 (2015).

[32] Arne Barfuss, *Hybrid spin-nanomechanics with single spins in diamond mechanical oscillators*, Ph.D. thesis, Basel (2017).

[33] A. Faraon, P. E. Barclay, C. Santori, K.-M. C. Fu, and R. G. Beausoleil, *Resonant enhancement of the zero-phonon emission from a colour centre in a diamond cavity*, Nature Photonics **5**, 301 (2011).

[34] Lucas Thiel, *Nanoscale magnetometry with a single spin in diamond at cryogenic temperatures*, Ph.D. thesis, Basel (2019).

[35] A. Drau, M. Lesik, L. Rondin, P. Spinicelli, O. Arcizet, J.-F. Roch, and V. Jacques, *Avoiding power broadening in optically detected magnetic resonance of single NV defects for enhanced dc magnetic field sensitivity*, Physical Review B **84** (2011).

[36] J. M. Taylor, P. Cappellaro, L. Childress, L. Jiang, D. Budker, P. R. Hemmer, A. Yacoby, R. Walsworth, and M. D. Lukin, *High-sensitivity diamond magnetometer with nanoscale resolution*, Nature Physics **4**, 810 (2008).

[37] I. I. Rabi, *Space Quantization in a Gyrating Magnetic Field*, Physical Review **51**, 652 (1937).

[38] M. A. Nielsen and I. L. Chuang, *Quantum computation and quantum information* (Cambridge University Press, Cambridge ; New York) (2000).

[39] E. L. Hahn, *Free nuclear induction*, Physics Today **6**, 4 (1953).

[40] B. K. Ofori-Okai, S. Pezzagna, K. Chang, M. Loretz, R. Schirhagl, Y. Tao, B. A. Moores, K. Groot-Berning, J. Meijer, and C. L. Degen, *Spin properties of very shallow nitrogen vacancy defects in diamond*, Phys. Rev. B **86**, 081406 (2012).

[41] T. Müller, C. Hepp, B. Pingault, E. Neu, S. Gsell, M. Schreck, H. Sternschulte, D. Steinmller-Nethl, C. Becher, and M. Atatre, *Optical signatures of silicon-vacancy spins in diamond*, Nature Communications **5**, 1 (2014).

[42] J. P. Goss, R. Jones, S. J. Breuer, P. R. Briddon, and S. berg, *The Twelve-Line 1.682 eV Luminescence Center in Diamond and the Vacancy-Silicon Complex*, Physical Review Letters **77**, 3041 (1996).

[43] L. J. Rogers, K. D. Jahnke, M. W. Doherty, A. Dietrich, L. P. McGuinness, C. Mller, T. Teraji, H. Sumiya, J. Isoya, N. B. Manson, and F. Jelezko, *Electronic structure of the negatively charged silicon-vacancy center in diamond*, Physical Review B **89**, 235101 (2014).

[44] K. D. Jahnke, A. Sipahigil, J. M. Binder, M. W. Doherty, M. Metsch, L. J. Rogers, N. B. Manson, M. D. Lukin, and F. Jelezko, *Electronphonon processes of the silicon-vacancy centre in diamond*, New J. Phys. **17**, 043011 (2015).

[45] D. Sukachev, A. Sipahigil, C. Nguyen, M. Bhaskar, R. Evans, F. Jelezko, and M. Lukin, *Silicon-Vacancy Spin Qubit in Diamond: A Quantum Memory Exceeding 10 ms with Single-Shot State Readout*, Physical Review Letters **119**, 223602 (2017).

[46] M. H. Metsch, K. Senkalla, B. Tratzmiller, J. Scheuer, M. Kern, J. Achard, A. Tallaire, M. B. Plenio, P. Siyushev, and F. Jelezko, *Initialization and Readout of Nuclear Spins via a Negatively Charged Silicon-Vacancy Center in Diamond*, Phys. Rev. Lett. **122**, 190503 (2019).

[47] U. Jantzen, A. B. Kurz, D. S. Rudnicki, C. Schfermeier, K. D. Jahnke, U. L. Andersen, V. A. Davydov, V. N. Agafonov, A. Kubanek, L. J. Rogers, and F. Jelezko, *Nanodiamonds carrying silicon-vacancy quantum emitters with almost lifetime-limited linewidths*, New Journal of Physics **18**, 073036 (2016).

[48] B. C. Rose, D. Huang, Z.-H. Zhang, P. Stevenson, A. M. Tyryshkin, S. Sangtawesin, S. Srinivasan, L. Loudin, M. L. Markham, A. M. Edmonds, D. J. Twitchen, S. A. Lyon, and N. P. d. Leon, *Observation of an environmentally insensitive solid-state spin defect in diamond*, Science **361**, 60 (2018).

[49] C. Galland, Y. Ghosh, A. Steinbrck, J. A. Hollingsworth, H. Htoon, and V. I. Klimov, *Lifetime blinking in nonblinking nanocrystal quantum dots*, Nature Communications **3**, 908 EP (2012).

[50] S. A. Momenzadeh, R. J. Sthr, F. F. de Oliveira, A. Brunner, A. Denisenko, S. Yang, F. Reinhard, and J. Wrachtrup, *Nanoengineered Diamond Waveguide as a Robust Bright Platform for Nanomagnetometry Using Shallow Nitrogen Vacancy Centers*, Nano Letters **15**, 165 (2015).

[51] M. Kaviani, P. Dek, B. Aradi, T. Frauenheim, J.-P. Chou, and A. Gali, *Proper Surface Termination for Luminescent Near-Surface NV Centers in Diamond*, Nano Letters **14**, 4772 (2014).

[52] G. Braunbeck, S. Mandal, M. Touge, O. Williams, and F. Reinhard, *Effect of ultraprecision polishing techniques on coherence times of shallow nitrogen-vacancy centers in diamond*, Diamond and Related Materials **85**, 18 (2018).

[53] I. Lovchinsky, A. O. Sushkov, E. Urbach, N. P. de Leon, S. Choi, K. De Greve, R. Evans, R. Gertner, E. Bersin, C. Muller, L. McGuinness, F. Jelezko, R. L. Walsworth, H. Park, and M. D. Lukin, *Nuclear magnetic resonance detection and spectroscopy of single proteins using quantum logic*, Science **351**, 836 (2016).

[54] M. Kim, H. J. Mamin, M. H. Sherwood, C. T. Rettner, J. Frommer, and D. Rugar, *Effect of oxygen plasma and thermal oxidation on shallow nitrogen-vacancy centers in diamond*, Applied Physics Letters **105**, 042406 (2014).

[55] S. B. van Dam, M. Walsh, M. J. Degen, E. Bersin, S. L. Mouradian, A. Galiullin, M. Ruf, M. IJspeert, T. H. Taminiau, R. Hanson, and D. R. Englund, *Optical coherence of diamond nitrogen-vacancy centers formed by ion implantation and annealing*, Physical Review B **99**, 161203 (2019).

[56] F. Favaro de Oliveira, D. Antonov, Y. Wang, P. Neumann, S. A. Momenzadeh, T. Huermann, A. Pasquarelli, A. Denisenko, and J. Wrachtrup, *Tailoring spin defects in diamond by lattice charging*, Nature Communications **8**, 15409 (2017).

[57] K. J. Brown, E. Chartier, E. M. Sweet, D. A. Hopper, and L. C. Bassett, *Cleaning diamond surfaces using boiling acid treatment in a standard laboratory chemical hood*, Journal of Chemical Health and Safety **26**, 40 (2019).

[58] V. Petrkov, A. Taylor, I. Kratochvlov, F. Fendrych, J. Vack, J. Kuka, J. tursa, P. Cgler, M. Ledvina, A. Fierov, P. Kneppo, and M. Nesldek, *Luminescence of Nanodiamond Driven by Atomic Functionalization: Towards Novel Detection Principles*, Advanced Functional Materials **22**, 812 (2012).

[59] P. E. Pehrsson and T. W. Mercer, *Oxidation of the hydrogenated diamond (100) surface*, Surface Science **460**, 49 (2000).

[60] F. Maier, J. Ristein, and L. Ley, *Electron affinity of plasma-hydrogenated and chemically oxidized diamond (100) surfaces*, Physical Review B **64**, 165411 (2001).

[61] M. V. Hauf, B. Grotz, B. Naydenov, M. Dankerl, S. Pezzagna, J. Meijer, F. Jelezko, J. Wrachtrup, M. Stutzmann, F. Reinhard, and J. A. Garrido, *Chemical control of the charge state of nitrogen-vacancy centers in diamond*, Physical Review B **83**, 081304 (2011).

[62] H. Yamano, S. Kawai, K. Kato, T. Kageura, M. Inaba, T. Okada, I. Higashimata, M. Haruyama, T. Tanii, K. Yamada, S. Onoda, W. Kada, O. Hanaizumi, T. Teraji, J. Isoya, and H. Kawarada, *Charge state stabilization of shallow nitrogen vacancy centers in diamond by oxygen surface modification*, Japanese Journal of Applied Physics **56**, 04CK08 (2017).

[63] Y. Romach, C. Mller, T. Unden, L. Rogers, T. Isoda, K. Itoh, M. Markham, A. Stacey, J. Meijer, S. Pezzagna, B. Naydenov, L. McGuinness, N. Bar-Gill, and F. Jelezko, *Spectroscopy of Surface-Induced Noise Using Shallow Spins in Diamond*, Physical Review Letters **114**, 017601 (2015).

[64] T. Rosskopf, A. Dussaux, K. Ohashi, M. Loretz, R. Schirhagl, H. Watanabe, S. Shikata, K. Itoh, and C. Degen, *Investigation of Surface Magnetic Noise by Shallow Spins in Diamond*, Physical Review Letters **112**, 147602 (2014).

[65] H. Bluhm, J. A. Bert, N. C. Koshnick, M. E. Huber, and K. A. Moler, *Spin-like Susceptibility of Metallic and Insulating Thin Films at Low Temperature*, Physical Review Letters **103**, 026805 (2009).

[66] F. Favaro de Oliveira, S. A. Momenzadeh, Y. Wang, M. Konuma, M. Markham, A. M. Edmonds, A. Denisenko, and J. Wrachtrup, *Effect of low-damage inductively coupled plasma on shallow nitrogen-vacancy centers in diamond*, Applied Physics Letters **107**, 073107 (2015).

[67] S. Sangtawesin, B. L. Dwyer, S. Srinivasan, J. J. Allred, L. V. Rodgers, K. De Greve, A. Stacey, N. Dontschuk, K. M. ODonnell, D. Hu, D. A. Evans, C. Jaye, D. A. Fischer, M. L. Markham, D. J. Twitchen, H. Park, M. D. Lukin, and N. P. de Leon, *Origins of Diamond Surface Noise Probed by Correlating Single-Spin Measurements with Surface Spectroscopy*, Physical Review X **9**, 031052 (2019).

[68] S. Stehlik, M. Varga, M. Ledinsky, V. Jirasek, A. Artemenko, H. Kozak, L. Ondic, V. Skakalova, G. Argentero, T. Pennycook, J. C. Meyer, A. Fejfar, A. Kromka, and B. Rezek, *Size and Purity Control of HPHT Nanodiamonds down to 1 nm*, The Journal of Physical Chemistry C **119**, 27708 (2015).

[69] I. Friel, S. Clewes, H. Dhillon, N. Perkins, D. Twitchen, and G. Scarsbrook, *Control of surface and bulk crystalline quality in single crystal diamond grown by chemical vapour deposition*, Diamond and Related Materials **18**, 808 (2009).

[70] M. Kim, H. J. Mamin, M. H. Sherwood, C. T. Rettner, J. Frommer, and D. Rugar, *Effect of oxygen plasma and thermal oxidation on shallow nitrogen-vacancy centers in diamond*, Applied Physics Letters **105**, 042406 (2014).

[71] S. Cui, A. S. Greenspon, K. Ohno, B. A. Myers, A. C. B. Jayich, D. D. Awschalom, and E. L. Hu, *Reduced Plasma-Induced Damage to Near-Surface Nitrogen-Vacancy Centers in Diamond*, Nano Letters **15**, 2887 (2015).

[72] A. Stacey, K. M. O'Donnell, J.-P. Chou, A. Schenk, A. Tadich, N. Dontschuk, J. Cervenka, C. Pakes, A. Gali, A. Hoffman, and S. Prawer, *Nitrogen Terminated Diamond*, Advanced Materials Interfaces **2**, 1500079 (2015).

[73] S. Cui and E. L. Hu, *Increased negatively charged nitrogen-vacancy centers in fluorinated diamond*, Applied Physics Letters **103**, 051603 (2013).

[74] P. Fuchs, M. Challier, and E. Neu, *Optimized Single-Crystal Diamond Scanning Probes for High Sensitivity Magnetometry*, New J. Phys. **20**, 125001 (2018).

[75] F. Favaro de Oliveira, S. A. Momenzadeh, Y. Wang, M. Konuma, M. Markham, A. M. Edmonds, A. Denisenko, and J. Wrachtrup, *Effect of low-damage inductively coupled plasma on shallow nitrogen-vacancy centers in diamond*, Applied Physics Letters **107**, 073107 (2015).

[76] P. Van der Heide, *X-ray photoelectron spectroscopy: an introduction to principles and practices*, (Wiley, Hoboken, N.J.) (2012).

[77] F. Klauser, S. Ghodbane, R. Boukherroub, S. Szunerits, D. Steinmller-Nethl, E. Bertel, and N. Memmel, *Comparison of different oxidation techniques on single-crystal and nanocrystalline diamond surfaces*, Diamond and Related Materials **19**, 474 (2010).

[78] www.casaxps.com, *Peak fitting in XPS*.

[79] R. Graupner, F. Maier, J. Ristein, L. Ley, and C. Jung, *High-resolution surface-sensitive C1s core-level spectra of clean and hydrogen-terminated diamond (100) and (111) surfaces*, Physical Review B **57**, 12397 (1998).

[80] S. Kono, T. Kageura, Y. Hayashi, S.-G. Ri, T. Teraji, D. Takeuchi, M. Ogura, H. Kodama, A. Sawabe, M. Inaba, A. Hiraiwa, and H. Kawarada, *Carbon 1s X-ray photoelectron spectra of realistic samples of hydrogen-terminated and oxygen-terminated CVD diamond (111) and (001)*, Diamond and Related Materials **93**, 105 (2019).

[81] Y. Xie and P. M. A. Sherwood, *X-ray photoelectron-spectroscopic studies of carbon fiber surfaces. 11. Differences in the surface chemistry and bulk structure of different carbon fibers based on poly(acrylonitrile) and pitch and comparison with various graphite samples*, Chemistry of Materials **2**, 293 (1990).

[82] M. Radtke, R. Nelz, A. Slablab, and E. Neu, *Reliable Nanofabrication of Single-Crystal Diamond Photonic Nanostructures for Nanoscale Sensing*, Micromachines **10**, 718 (2019).

[83] R. G. Ryan, A. Stacey, K. M. ODonnell, T. Ohshima, B. C. Johnson, L. C. L. Hollenberg, P. Mulvaney, and D. A. Simpson, *Impact of Surface Functionalization on the Quantum Coherence of Nitrogen-Vacancy Centers in Nanodiamonds*, ACS Applied Materials & Interfaces **10**, 13143 (2018).

[84] M. Inaba, H. Kawarada, and Y. Ohno, *Electrical property measurement of two-dimensional hole-gas layer on hydrogen-terminated diamond surface in vacuum-gap-gate structure*, Appl. Phys. Lett. **114**, 253504 (2019).

[85] C. E. Nebel, B. Rezek, and A. Zrenner, *2d-hole accumulation layer in hydrogen terminated diamond*, physica status solidi (a) **201**, 2432 (2004).

[86] K. J. Rietwyk, S. L. Wong, L. Cao, K. M. O'Donnell, L. Ley, A. T. S. Wee, and C. I. Pakes, *Work function and electron affinity of the fluorine-terminated (100) diamond surface*, Applied Physics Letters **102**, 091604 (2013).

[87] S. Kawai, H. Yamano, T. Sonoda, K. Kato, J. J. Buendia, T. Kageura, R. Fukuda, T. Okada, T. Tanii, T. Higuchi, M. Haruyama, K. Yamada, S. Onoda, T. Ohshima, W. Kada, O. Hanaizumi, A. Stacey, T. Teraji, S. Kono, J. Isoya, and H. Kawarada, *Nitrogen-Terminated Diamond Surface for Nanoscale NMR by Shallow Nitrogen-Vacancy Centers*, The Journal of Physical Chemistry C **123**, 3594 (2019).

[88] C. Schreyvogel, V. Polyakov, R. Wunderlich, J. Meijer, and C. E. Nebel, *Active charge state control of single NV centres in diamond by in-plane Al-Schottky junctions*, Scientific Reports **5**, 12160 (2015).

[89] A. Gali and J. R. Maze, *Ab initio study of the split silicon-vacancy defect in diamond: Electronic structure and related properties*, Phys. Rev. B **88**, 235205 (2013).

[90] P. Deak, B. Aradi, M. Kaviani, T. Frauenheim, and A. Gali, *Formation of NV centers in diamond: A theoretical study based on calculated transitions and migration of nitrogen and vacancy related defects*, Physical Review B **89**, 075203 (2014).

[91] U. F. S. D'Haenens-Johansson, A. M. Edmonds, B. L. Green, M. E. Newton, G. Davies, P. M. Martineau, R. U. A. Khan, and D. J. Twitchen, *Optical properties of the neutral silicon split-vacancy center in diamond*, Physical Review B **84**, 245208 (2011).

[92] A. T. Collins, *The Fermi level in diamond*, Journal of Physics: Condensed Matter **14**, 3743 (2002).

[93] C. E. Nebel, B. Rezek, D. Shin, and H. Watanabe, *Surface electronic properties of H-terminated diamond in contact with adsorbates and electrolytes*, physica status solidi (a) **203**, 3273 (2006).

[94] J. Ristein, M. Riedel, and L. Ley, *Electrochemical Surface Transfer Doping*, Journal of The Electrochemical Society **151**, E315 (2004).

[95] A. N. Newell, D. A. Dowdell, and D. H. Santamore, *Surface effects on nitrogen vacancy centers neutralization in diamond*, Journal of Applied Physics **120**, 185104 (2016).

[96] V. Seshan, D. Ullien, A. Castellanos-Gomez, S. Sachdeva, D. H. K. Murthy, T. J. Savenije, H. A. Ahmad, T. S. Nunney, S. D. Janssens, K. Haenen, M. Nesldek, H. S. J. van der Zant, E. J. R. Sudhlter, and L. C. P. M. de Smet, *Hydrogen termination of CVD diamond films by high-temperature annealing at atmospheric pressure*, The Journal of Chemical Physics **138**, 234707 (2013).

[97] I. Langmuir, *The dissociation of hydrogen into atoms.* , Journal of the American Chemical Society **34**, 860 (1912).

[98] A. C. Ferrari and J. Robertson, *Resonant Raman spectroscopy of disordered, amorphous, and diamondlike carbon*, Physical Review B **64**, 075414 (2001).

[99] C. Manfredotti, P. Bonino, M. De La Pierre, E. Vittone, and C. Manfredotti, *About orientation dependence of physico-chemical properties of HPHT diamond surfaces thermally treated in H2 and D2 environments*, Diamond and Related Materials **19**, 279 (2010).

[100] N. Stojilovic, *Why Cant We See Hydrogen in X-ray Photoelectron Spectroscopy?*, Journal of Chemical Education **89**, 1331 (2012).

[101] P. Appel, *Scanning nanomagnetometry, probing magnetism with single spins in diamond*, Ph.D. thesis (2017).

[102] G. Braunbeck, S. Mandal, M. Touge, O. Williams, and F. Reinhard, *Effect of ultraprecision polishing techniques on coherence times of shallow nitrogen-vacancy centers in diamond*, Diamond and Related Materials **85**, 18 (2018).

[103] B. Shields, Q. Unterreithmeier, N. de Leon, H. Park, and M. Lukin, *Efficient Readout of a Single Spin State in Diamond via Spin-to-Charge Conversion*, Physical Review Letters **114**, 136402 (2015).

[104] M. Atatre, D. Englund, N. Vamivakas, S.-Y. Lee, and J. Wrachtrup, *Material platforms for spin-based photonic quantum technologies*, Nature Reviews Materials **3**, 38 (2018).

[105] R. E. Evans, A. Sipahigil, D. D. Sukachev, A. S. Zibrov, and M. D. Lukin, *Narrow-Linewidth Homogeneous Optical Emitters in Diamond Nanostructures via Silicon Ion Implantation*, Physical Review Applied **5**, 044010 (2016).

[106] B. M. Nichols, J. E. Butler, J. N. Russell, and R. J. Hamers, *Photochemical Functionalization of Hydrogen-Terminated Diamond Surfaces: A Structural and Mechanistic Study*, The Journal of Physical Chemistry B **109**, 20938 (2005).

[107] D.-w. Zhang and Y.-x. Cui, *Surface chemical modification of CVD diamond films by laser irradiation*, International Journal of Refractory Metals and Hard Materials **81**, 36 (2019).

[108] C. E. Nebel, C. Sauerer, F. Ertl, M. Stutzmann, C. F. O. Graeff, P. Bergonzo, O. A. Williams, and R. Jackman, *Hydrogen-induced transport properties of holes in diamond surface layers*, Applied Physics Letters **79**, 4541 (2001).

[109] D. A. Broadway, N. Dontschuk, A. Tsai, S. E. Lillie, C. T.-K. Lew, J. C. McCallum, B. C. Johnson, M. W. Doherty, A. Stacey, L. C. L. Hollenberg, and J.-P. Tetienne, *Spatial mapping of band bending in semiconductor devices using in situ quantum sensors*, Nat Electron **1**, 502 (2018).

[110] A. Gali and J. R. Maze, *Ab initio study of the split silicon-vacancy defect in diamond: Electronic structure and related properties*, Physical Review B **88**, 235205 (2013).

[111] A. N. Newell, D. A. Dowdell, and D. H. Santamore, *Surface effects on nitrogen vacancy centers neutralization in diamond*, Journal of Applied Physics **120**, 185104 (2016).

[112] O. A. Williams and R. B. Jackman, *Surface conductivity on hydrogen terminated diamond*, Semiconductor Science and Technology **18**, S34 (2003).

[113] W. Melitz, J. Shen, A. C. Kummel, and S. Lee, *Kelvin probe force microscopy and its application*, Surface Science Reports **66**, 1 (2011).

[114] S. Sadewasser and T. Glatzel (editors), *Kelvin Probe Force Microscopy*, *Springer Series in Surface Sciences*, volume 48 (Springer Berlin Heidelberg, Berlin, Heidelberg) (2012).

[115] S. Stehlik, T. Glatzel, V. Pichot, R. Pawlak, E. Meyer, D. Spitzer, and B. Rezek, *Water interaction with hydrogenated and oxidized detonation nanodiamonds Microscopic and spectroscopic analyses*, Diamond and Related Materials **63**, 97 (2016).

[116] Y. Homma, S. Chiashi, T. Yamamoto, K. Kono, D. Matsumoto, J. Shitaba, and S. Sato, *Photoluminescence Measurements and Molecular Dynamics Simulations of Water Adsorption on the Hydrophobic Surface of a Carbon Nanotube in Water Vapor*, Physical Review Letters **110**, 157402 (2013).

[117] H. Kawarada, T. Yamada, D. Xu, H. Tsuboi, T. Saito, and A. Hiraiwa, *Wide temperature (10K700K) and high voltage (∼1000V) operation of C-H diamond MOSFETs for power electronics application*, in *2014 IEEE International Electron Devices Meeting* (IEEE, San Francisco, CA, USA) (2014).

[118] Y. Yang, F. A. Koeck, M. Dutta, X. Wang, S. Chowdhury, and R. J. Nemanich, *Al $_2$ O $_3$ dielectric layers on H-terminated diamond: Controlling surface conductivity*, Journal of Applied Physics **122**, 155304 (2017).

[119] A. Voss, S. R. Stateva, J. P. Reithmaier, M. D. Apostolova, and C. Popov, *Patterning of the surface termination of ultrananocrystalline diamond films for guided cell attachment and growth*, Surface and Coatings Technology **321**, 229 (2017).

[120] M. Batzer, B. Shields, E. Neu, C. Widmann, C. Giese, C. Nebel, and P. Maletinsky, *Single crystal diamond pyramids for applications in nanoscale quantum sensing*, arXiv:1910.10737 [cond-mat, physics:quant-ph] (2019).

[121] Y. Nishibayashi, H. Saito, T. Imai, and N. Fujimori, *Homoepitaxial growth on fine columns of single crystal diamond for a field emitter*, Diamond and Related Materials **9**, 290 (2000).

[122] T. Jaffe, N. Felgen, L. Gal, L. Kornblum, J. P. Reithmaier, C. Popov, and M. Orenstein, *Deterministic Arrays of Epitaxially Grown Diamond Nanopyramids with Embedded Silicon-Vacancy Centers*, Advanced Optical Materials **7**, 1800715 (2019).

[123] C. J. Widmann, C. Giese, M. Wolfer, D. Brink, N. Heidrich, and C. E. Nebel, *Fabrication and characterization of single crystalline diamond nanopillars with NV-centers*, Diamond and Related Materials **54**, 2 (2015).

[124] e6, See https://www.e6.com for more information.

[125] C. J. Widmann, *Characterization and optimization of nanoscale magnetometric diamond sensors*, PhD Thesis (2017).

[126] A. Bogatskiy and J. E. Butler, *A geometric model of growth for cubic crystals: Diamond*, Diamond and Related Materials **53**, 58 (2015).

[127] F. Silva, J. Achard, X. Bonnin, O. Brinza, A. Michau, A. Secroun, K. De Corte, S. Felton, M. Newton, and A. Gicquel, *Single crystal CVD diamond growth strategy by the use of a 3d geometrical model: Growth on (113) oriented substrates*, Diamond and Related Materials **17**, 1067 (2008).

[128] F. Silva, X. Bonnin, J. Achard, O. Brinza, A. Michau, and A. Gicquel, *Geometric modeling of homoepitaxial CVD diamond growth: I. The {100}{111}{110}{113} system*, Journal of Crystal Growth **310**, 187 (2008).

[129] G. Janssen, J. Schermer, W. van Enckevort, and L. Giling, *On the occurrence of {113}; facets on CVD-grown diamond*, Journal of Crystal Growth **125**, 42 (1992).

[130] C. UzanSaguy, C. Cytermann, R. Brener, V. Richter, M. Shaanan, and R. Kalish, *Damage threshold for ionbeam induced graphitization of diamond*, Applied Physics Letters **67**, 1194 (1995).

[131] Z. Ma, B. Liu, H. Naramoto, Y. Aoki, S. Yamamoto, H. Takeshita, and P. Goppelt-Langer, *Non-destructive characterization of ion-implanted diamond*, Vacuum **55**, 207 (1999).

[132] P. Reinke, G. Francz, P. Oelhafen, and J. Ullmann, *Structural changes in diamond and amorphous carbon induced by low-energy ion irradiation*, Physical Review B **54**, 7067 (1996).

[133] S. B. van Dam, M. Walsh, M. J. Degen, E. Bersin, S. L. Mouradian, A. Galiullin, M. Ruf, M. IJspeert, T. H. Taminiau, R. Hanson, and D. R. Englund, *Optical coherence of diamond nitrogen-vacancy centers formed by ion implantation and annealing*, Physical Review B **99**, 161203 (2019).

[134] R. Nelz, P. Fuchs, O. Opaluch, S. Sonusen, N. Savenko, V. Podgursky, and E. Neu, *Color center fluorescence and spin manipulation in single crystal, pyramidal diamond tips*, Applied Physics Letters **109**, 193105 (2016).

[135] R. Samlenski, C. Haug, R. Brenn, C. Wild, R. Locher, and P. Koidl, *Incorporation of nitrogen in chemical vapor deposition diamond*, Applied Physics Letters **67**, 2798 (1995).

[136] A. Gruber, A. Drabenstedt, C. Tietz, L. Fleury, J. Wrachtrup, and C. Borczyskowski, *Scanning Confocal Optical Microscopy and Magnetic Resonance on Single Defect Centers*, Science **276**, 2012 (1997).

[137] S. Pezzagna, B. Naydenov, F. Jelezko, J. Wrachtrup, and J. Meijer, *Creation efficiency of nitrogen-vacancy centres in diamond*, New Journal of Physics **12**, 065017 (2010).

[138] C. Kurtsiefer, S. Mayer, P. Zarda, and H. Weinfurter, *Stable Solid-State Source of Single Photons*, Physical Review Letters **85**, 4 (2000).

[139] D. Riedel, D. Rohner, M. Ganzhorn, T. Kaldewey, P. Appel, E. Neu, R. Warburton, and P. Maletinsky, *Low-Loss Broadband Antenna for Efficient Photon Collection from a Coherent Spin in Diamond*, Physical Review Applied **2**, 064011 (2014).

[140] A. B. Vasista, D. K. Sharma, and G. V. P. Kumar, *Fourier plane optical microscopy and spectroscopy*, arXiv:1806.08280 [cond-mat, physics:physics] (2019).

[141] S. Choi, V. Leong, G. Alagappan, and L. Krivitsky, *Enhancing Optical Readout from Diamond AFM Tips for Quantum Nanosensing* ACS Photonics **5**, 4244 (2018).

[142] C.-K. Duan and M. F. Reid, *Dependence of the spontaneous emission rates of emitters on the refractive index of the surrounding media*, Journal of Alloys and Compounds **418**, 213 (2006).

[143] V. LeBihan, A. Pillonnet, D. Amans, G. Ledoux, O. Marty, and C. Dujardin, *Critical dimension where the macroscopic definition of refractive index can be applied at a nanometric scale*, Physical Review B **78** (2008).

[144] C. J. Widmann, M. Hetzl, S. Drieschner, and C. E. Nebel, *Homoepitaxial growth of high quality (111)-oriented single crystalline diamond*, Diamond and Related Materials **72**, 41 (2017).

[145] T. X. Zhou, R. J. Sthr, and A. Yacoby, *Scanning diamond NV center probes compatible with conventional AFM technology*, Applied Physics Letters **111**, 163106 (2017).

[146] Y. Kato, H. Kawashima, T. Makino, M. Ogura, A. Traor, N. Ozawa, and S. Yamasaki, *Estimation of Inductively Coupled Plasma Etching Damage of Boron-Doped Diamond Using X-Ray Photoelectron Spectroscopy*, physica status solidi (a) **214**, 1700233 (2017).

[147] J. Riedrich-Mller, S. Pezzagna, J. Meijer, C. Pauly, F. Mcklich, M. Markham, A. M. Edmonds, and C. Becher, *Nanoimplantation and Purcell enhancement of single nitrogen-vacancy centers in photonic crystal cavities in diamond*, Applied Physics Letters **106**, 221103 (2015).

[148] T. Schrder, M. E. Trusheim, M. Walsh, L. Li, J. Zheng, M. Schukraft, A. Sipahigil, R. E. Evans, D. D. Sukachev, C. T. Nguyen, J. L. Pacheco, R. M. Camacho, E. S. Bielejec, M. D. Lukin, and D. Englund, *Scalable focused ion beam creation of nearly lifetime-limited single quantum emitters in diamond nanostructures*, Nature Communications **8**, 15376 (2017).

[149] R. Yoshida, D. Miyata, T. Makino, S. Yamasaki, T. Matsumoto, T. Inokuma, and N. Tokuda, *Formation of atomically flat hydroxyl-terminated diamond (111) surfaces via water vapor annealing*, Applied Surface Science **458**, 222 (2018).

[150] James Ziegler, See http://www.srim.org/ for more information.

Aknowledgement

First and foremost, I would like to thank Patrick Maletinsky and Uwe Piles. Without them, this thesis would not have been possible. Next, I would like to thank the SNI for funding this project and of course, the whole quantum sensing group as it is and as it was. But it does not end with the group; the entire department of physics in Basel is exceptional. Due to the interdisciplinary character of my project, I had the joy to work with several people outside the group. But I got also help outside the department without the input and help of Sina Saxer and the rest of the nanochemistry team I would have been completely lost at the beginning.

Scientific collaborations and input are essential, but during times when "Diamonds are a girl's best friend" (Marilin Monroe) is wishful thinking, emotional support is even more important. I want to thank my parents for all their advice and support. I did not always agree with them (and that's most certainly is a mutual feeling), but they supported me literally from day one on. I feel fortunate to have such an empathic and caring mom. Thank you for sharing your wisdom and for always being there for me. I also feel lucky with my dad. In many aspects, he is a role model for me, and I value his advice and our discussions.

I want to thank all the persons that read part of this thesis or helped me keeping my shit together during these last few months. The quantum sensing group was always a great workplace, but in the last years, it became more. I especially want to thank the D&D crew and the bouldering addicts. These and all the other, not work-related activities turned my PhD experience into something special.

Last but not least, I want to thank my whole office. I feel lucky to share my office with such considered people, and I enjoyed our discussions very much.

I want to thank the whole group for an amazing time. I found comradeship, friendship, and more. Thanks for making the last five years into a not always smooth, but fun ride.